

SOUND TRANSMISSION LOSS OF COMPOSITE SANDWICH PANELS

Except where reference is made to the work of others, the work described in this dissertation is my own or was done in collaboration with my advisory committee. This dissertation does not include proprietary or classified information.

Ran Zhou

Certificate of Approval:

George T. Flowers
Professor
Mechanical Engineering

Malcolm J. Crocker, Chair
Distinguished University Professor
Mechanical Engineering

Winfred A. Foster, Jr.
Professor
Aerospace Engineering

Subhash C. Sinha
Professor
Mechanical Engineering

George T. Flowers
Dean
Graduate School

SOUND TRANSMISSION LOSS OF COMPOSITE SANDWICH PANELS

Ran Zhou

A Dissertation

Submitted to

the Graduate Faculty of

Auburn University

in Partial Fulfillment of the

Requirements for the

Degree of

Doctor of Philosophy

Auburn, Alabama

May 9, 2009

SOUND TRANSMISSION LOSS OF COMPOSITE SANDWICH PANELS

Ran Zhou

Permission is granted to Auburn University to make copies of this dissertation at its discretion, upon the request of individuals or institutions and at their expense. The author reserves all publication rights.

Signature of Author

Date of Graduation

VITA

Ran Zhou, daughter of Kaiti Zhou and Jiena Shao, was born on October 26, 1977, in Taiyuan, Shanxi, China. She entered Nanjing University in September, 1995, and graduated with a GPA of 4.5 (out of 5) with a Bachelor of Science degree in Electronic Science and Engineering in June, 1999. Then she entered Graduate School, Nanjing University, in September, 1999, and graduated with a Master of Science degree in Electronic Science and Engineering in June, 2002. She entered Auburn University in August, 2002.

DISSERTATION ABSTRACT

SOUND TRANSMISSION LOSS OF COMPOSITE SANDWICH PANELS

Ran Zhou

Doctor of Philosophy, May 9, 2009
(M.S., Nanjing University, 2002)
(B.S., Nanjing University, 1999)

205 Typed Pages

Directed by Malcolm J. Crocker

Light composite sandwich panels are increasingly used in automobiles, ships and aircraft, because of the advantages they offer of high strength-to-weight ratios. However, the acoustical properties of these light and stiff structures can be less desirable than those of equivalent metal panels. These undesirable properties can lead to high interior noise levels. A number of researchers have studied the acoustical properties of honeycomb and foam sandwich panels. Not much work, however, has been carried out on foam-filled honeycomb sandwich panels.

In this dissertation, governing equations for the forced vibration of asymmetric sandwich panels are developed. An analytical expression for modal densities of symmetric sandwich panels is derived from a sixth-order governing equation. A boundary element analysis model for the sound transmission loss of symmetric sandwich panels is proposed. Measurements of the modal density, total loss factor, radiation loss factor, and sound transmission loss of foam-filled honeycomb sandwich panels with different configurations and thicknesses

are presented. Comparisons between the predicted sound transmission loss values obtained from wave impedance analysis, statistical energy analysis, boundary element analysis, and experimental values are presented.

The wave impedance analysis model provides accurate predictions of sound transmission loss for the thin foam-filled honeycomb sandwich panels at frequencies above their first resonance frequencies. The predictions from the statistical energy analysis model are in better agreement with the experimental transmission loss values of the sandwich panels when the measured radiation loss factor values near coincidence are used instead of the theoretical values for single-layer panels. The proposed boundary element analysis model provides more accurate predictions of sound transmission loss for the thick foam-filled honeycomb sandwich panels than either the wave impedance analysis model or the statistical energy analysis model.

ACKNOWLEDGMENTS

I would like to thank Dr. Malcolm J. Crocker for his guidance during this research. I am also thankful to Dr. George T. Flowers, Dr. Winfred A. Foster, Dr. Subhash C. Sinha, and Shannon Price for their help. Thanks are also due to my parents for their support and encouragement.

Style manual or journal used Journal of Approximation Theory (together with the style known as “aums”). Bibliography follows Journal of Sound and Vibration

Computer software used The document preparation package T_EX (specifically L^AT_EX) together with the departmental style-file aums.sty.

TABLE OF CONTENTS

LIST OF FIGURES	x
1 INTRODUCTION	1
1.1 Background	1
1.2 Approaches	1
1.3 Dissertation outline	3
2 LITERATURE REVIEW	6
2.1 Wave impedance analysis	6
2.2 Statistical energy analysis	10
2.3 Boundary element analysis	15
3 WAVE IMPEDANCE ANALYSIS	18
3.1 Introduction	18
3.2 Governing equations for forced vibration	19
3.3 Sound transmission loss	27
3.4 Symmetric sandwich panels	31
3.5 Numerical results	33
3.6 Other TL models for asymmetric sandwich panels	43
3.7 Other governing equations for anti-symmetric motion	48
3.8 Conclusions	52
4 STATISTICAL ENERGY ANALYSIS	54
4.1 Introduction	54
4.2 Assumptions and concepts	55
4.3 Transmission suite model	59
4.4 Modal densities	62
4.5 Internal loss factors	68
4.6 Coupling loss factors	69
4.7 Sound transmission loss	77
4.8 Numerical results	80
4.9 Conclusions	84
5 BOUNDARY ELEMENT ANALYSIS	86
5.1 Introduction	86
5.2 Finite element analysis models for sandwich structures	87
5.3 Basic concepts of boundary element analysis	91

5.4	Boundary element analysis model for fluid-structure-fluid systems	95
5.5	Boundary element analysis model for three-layer symmetric sandwich panels	108
5.6	Conclusions	110
6	MATERIALS AND MATERIAL PROPERTIES	112
6.1	Introduction	112
6.2	Materials	113
6.3	Measurement methods for materials	118
6.4	Experimental resonance frequencies of sandwich beams	121
6.5	Material properties of sandwich panels	128
6.6	Conclusions	134
7	DYNAMIC PROPERTIES OF COMPOSITE SANDWICH PANELS	135
7.1	Introduction	135
7.2	Experimental modal densities	136
7.3	Experimental total loss factors	144
7.4	Experimental radiation loss factors	149
7.5	Experimental internal loss factors	159
7.6	Conclusions	160
8	SOUND TRANSMISSION LOSS OF COMPOSITE SANDWICH PANELS	161
8.1	Introduction	161
8.2	Experimental sound transmission loss	162
8.3	Sound transmission loss from wave impedance analysis	164
8.4	Sound transmission loss from statistical energy analysis	172
8.5	Sound transmission loss from boundary element analysis	176
8.6	Conclusions	181
9	CONCLUSIONS	183
	BIBLIOGRAPHY	186
A	DERIVATION OF STIFFNESS CONSTANTS OF ROTATED-AXIS	191
B	PARTIAL DIFFERENTIAL OPERATORS	194

LIST OF FIGURES

3.1	The geometry and loads of a sandwich panel	19
3.2	Symmetric and anti-symmetric face sheet displacements	21
3.3	The rotated axis system of the orthotropic material	23
3.4	Components of pressure fields on a sandwich panel	27
3.5	Predicted wave numbers for anti-symmetric waves in panel <i>A</i>	35
3.6	Predicted wave speeds for anti-symmetric motion of panel <i>A</i>	37
3.7	Predicted wave speeds for symmetric motion of panel <i>A</i>	37
3.8	Wave impedances along two principal directions for panel <i>A</i>	39
3.9	Calculated sound transmission loss values of panel <i>A</i> without damping . . .	39
3.10	Predicted and measured sound transmission loss values of panel <i>A</i>	40
3.11	Wave impedances along two principal directions for panel <i>B</i>	42
3.12	Predicted and measured sound transmission loss values of panel <i>B</i>	42
3.13	Calculated wave impedances for symmetric panel <i>C</i>	46
3.14	Predicted sound transmission loss values of panel <i>C</i> from Dym and Lang's model	47
3.15	Predicted sound transmission loss values of panel <i>C</i> from the present analysis	47
3.16	Predicted sound transmission loss values of panel <i>A</i> made using governing equations	52
4.1	Block diagram for power flows between the structure and the reverberant field	57
4.2	Block diagram for power flows between the structure and two reverberation rooms	60

4.3	The transmission suite	61
4.4	Constant frequency loci for transverse wave numbers of a simply supported panel	63
4.5	Wave numbers for free transverse wave in x -axis of panel A	67
4.6	Modal densities of free transverse wave in x -axis of panel A	68
4.7	Effective radiation areas for edge and corner modes	73
4.8	Normalized radiation resistances of baffled simple supported aluminum panels	75
4.9	Sound transmission measurements from the two-room method	77
4.10	Estimated transmission loss values of panel D	81
4.11	Resonant and non-resonant modes on the sound transmission loss of panel D	82
4.12	Estimated sound transmission loss values of panel A	83
4.13	The effects of dimensions of panels and volumes of rooms on sound transmission loss	84
5.1	Finite element model for sandwich structures using MSC Nastran	88
5.2	A cantilever sandwich beam with viscoelastic core (beam G)	90
5.3	Half-space V limited by an infinite rigid plane S_H and boundary S	94
5.4	Sound fields Ω_1 and Ω_2 created by a baffled planar vibrating structure . . .	97
5.5	Calculated sound transmission loss values of the aluminum panel H for sound waves at normal incidence using the BEM computer program	103
5.6	Calculated sound transmission loss values of the aluminum panel H for sound waves at oblique incidence using the BEM computer program	105
5.7	Predicted sound transmission loss values of the aluminum panel H for sound waves at normal incidence	107
5.8	Predicted sound transmission loss values of the aluminum panel H for sound waves at oblique incidence	107

6.1	Commonly used cell configurations for honeycomb core materials (a) hexagonal (b) square (c) over expanded hexagonal (d) flex	115
6.2	Manufacture of honeycomb cores - corrugating (top) and expansion (bottom) processes	115
6.3	The face sheet (a) and core (b) materials of sandwich structures in this study	118
6.4	The frequency response function of the aluminum beam for the shaker set-up	120
6.5	The frequency response function of the aluminum beam for the impact set-up	120
6.6	The frequency response function of beam I_x	123
6.7	The frequency response function of beam I_y	123
6.8	The frequency response function of beam J_x	123
6.9	The frequency response function of beam J_y	124
6.10	The frequency response function of beam K_x	124
6.11	The frequency response function of beam K_y	124
6.12	The frequency response function of beam L_x	125
6.13	The frequency response function of beam L_y	125
6.14	Loss factors of beams I_x, I_y, J_x and J_y	126
6.15	Loss factors of beams K_x and K_y	127
6.16	The frequency response functions of the aluminum beam	127
6.17	Transverse displacement caused by (a) bending and (b) shear	129
7.1	Set-up for the modal density and loss factor experiments	139
7.2	The inertance of the added mass	140
7.3	The measured point mobility of panel J using the three-channel spectral analysis (a) real part (b) imaginary part	141
7.4	Modal density estimates for panel J without mass correction	141

7.5	Modal density estimates for panel J with mass correction	142
7.6	Modal density estimates for panel I with mass correction	143
7.7	Modal density estimates for panel K with mass correction	143
7.8	Modal density estimates for panel L with mass correction	144
7.9	Loss factor estimates for panel J	147
7.10	Loss factor estimates for panel I	147
7.11	Loss factor estimates for panel K	148
7.12	Loss factor estimates for panel L	148
7.13	Radiation resistance estimates for baffled clamped panel I	153
7.14	Radiation resistance estimates for baffled clamped panel J	153
7.15	Radiation resistance estimates for baffled clamped panel K	154
7.16	Radiation resistance estimates for baffled clamped panel L	154
7.17	Radiation loss factor estimates for clamped panels $I \sim L$	155
7.18	Radiation resistance estimates for unbaffled free-edge panel I	156
7.19	Radiation resistance estimates for unbaffled free-edge panel J	157
7.20	Radiation resistance estimates for unbaffled free-edge panel K	157
7.21	Radiation resistance estimates for unbaffled free-edge panel L	158
7.22	Radiation loss factor estimates for unbaffled free-edge panels $I \sim L$	158
7.23	Internal loss factor estimates for panels $I \sim L$	159
8.1	Experimental sound transmission loss values of panel I	164
8.2	Experimental sound transmission loss values of panel J	165
8.3	Experimental sound transmission loss values of panel K	165

8.4	Experimental sound transmission loss values of panel L	166
8.5	Predicted sound transmission loss values of panel I from the wave impedance analysis	167
8.6	Predicted sound transmission loss values of panel J from the wave impedance analysis	168
8.7	Predicted sound transmission loss values of panel K from the wave impedance analysis	168
8.8	Predicted sound transmission loss values of panel L from the wave impedance analysis	169
8.9	Predicted sound transmission loss values of panel I by using Eq. (??) . . .	170
8.10	Predicted sound transmission loss values of panel J by using Eq. (??) . . .	171
8.11	Predicted sound transmission loss values of panel K by using Eq. (??) . . .	171
8.12	Predicted sound transmission loss values of panel L by using Eq. (??) . . .	172
8.13	Transmission loss estimates for panel I from SEA	174
8.14	Transmission loss estimates for panel I using the measured values of η_{rad} .	174
8.15	Transmission loss estimates for panel J using the measured values of η_{rad} .	175
8.16	Transmission loss estimates for panel K using the measured values of η_{rad} .	175
8.17	Transmission loss estimates for panel L using the measured values of η_{rad} .	176
8.18	Predicted sound transmission loss values of panel K from the boundary element analysis, for sound waves at oblique incidences	178
8.19	Predictions of sound transmission loss for panel K made using the boundary element analysis model	179
8.20	The prediction of sound transmission loss for panel I made using the boundary element analysis model	180
8.21	The prediction of sound transmission loss for panel J made using the boundary element analysis model	180
8.22	The prediction of sound transmission loss for panel L made using the boundary element analysis model	181
A.1	The rotated-axis coordinate system of the orthotropic material	192

CHAPTER 1

INTRODUCTION

1.1 Background

Sound transmission loss is mostly determined by the mass, and the dynamic stiffness of structures. A high mass-to-stiffness ratio usually produces a high transmission loss. Because of the presence of the core, the dynamic stiffness of sandwich structures is strongly dependent on frequency and decreases with increasing frequency. Thus, the sound transmission loss of sandwich panels can be much different from that of single-layer panels. Three approaches have been used to investigate the sound transmission characteristics of single-layer panels.

1.2 Approaches

Wave impedance analysis is the most straightforward approach to calculate the sound transmission loss of panels. The wave impedance of a panel is derived from governing equations for the forced vibration of the panel. Since the acoustic particle velocity must match the transverse velocity of the panel at the fluid-structure interfaces, the pressures in the incident, reflected and radiated waves at the interface can be related to the wave impedance of the panel. Wave impedance analysis assumes that the panel is infinite, so that only the non-resonant forced motion is considered below the coincidence frequency.

Most previous work has used wave impedance analysis to predict the sound transmission loss of sandwich panels.

Statistical energy analysis (SEA) was developed in the early 1960's for estimating the response and radiation properties of structures excited by broadband noise. With broadband random noise excitation, the statistical properties such as mean square values and power densities can be used to provide a measure of vibration. SEA works best with reverberant fields of vibration, and has been used to predict the interaction between resonant structures and reverberant acoustic fields. SEA is very attractive for use in high frequency regions where modal densities are high and a deterministic analysis of all the resonant modes of the vibration of a structure is not practical.

The introduction of computers has permitted increasing use of numerical simulation analyses, including boundary element analysis and finite element analysis. The boundary element analysis produces more details of the vibro-acoustic interaction than the wave impedance analysis or the statistical energy analysis, especially at low frequencies, where the requirements of SEA may not be met. For finite and boundary element analyses, the mesh of the structure should provide with at least five finite element nodes per acoustic wavelength in the frequency range of interest. At high frequencies, a very refined discretization is required, which leads to a large algebraic system. Even with high speed computers, the computation time for a single frequency is considerable.

The manufacture of high modulus reinforced fabrics increases the application of composite sandwich panels. The relative difference between the stiffnesses of high modulus

reinforced face sheets and cores of the sandwich panels in this study is not the same as that of the traditional sandwich panels for normal constructions [1, 2, 3, 4, 5, 6, 7, 10]. A few experimental sound transmission loss data for sandwich panels with high modulus reinforced face sheets are available in the literature [8, 59, 60]. In Ref. [8] the sandwich panels were treated as single-layer panels with an equivalent dynamic bending stiffness in order to calculate the transmission loss of the sandwich panels. The other two references only presented comparisons of the experimental results with the mass law values [59, 60].

1.3 Dissertation outline

This dissertation is organized as follows.

Chapter 2 presents a review of previous work on the three analyses, wave impedance analysis, statistical energy analysis, and boundary element analysis. The section on wave impedance analysis includes derivations of governing equations for the forced vibration and the sound transmission loss of sandwich panels. The section on statistical energy analysis provides SEA applications for the prediction of noise and vibration associated with structures and acoustic volumes, together with work on the three main parameters, modal density, internal loss factor, and coupling loss factor. Chapter 2 closes with a brief review of boundary element analysis on the fluid-structure-fluid interaction.

Chapter 3 deals with wave impedance analysis. Governing equations for the forced vibration of asymmetric sandwich panels with orthotropic cores are developed, then these are followed by a sound transmission loss model which makes use of wave impedance analysis for

asymmetric sandwich panels. The sound transmission characteristics of two sandwich panels with honeycomb cores are discussed. Comparisons of the governing equations developed herein and other available governing equations for sandwich panels are provided.

Chapter 4 starts with an introduction of SEA, together with a sound transmission loss model using SEA. Then theoretical estimation methods for the three main parameters used in SEA, especially for composite sandwich panels, are discussed. In SEA, the response of structures is dependent on not only the dimensions of structures, but the dimensions of acoustic volumes as well. The effects of these dimensions on the predictions of sound transmission loss for panels are illustrated.

Chapter 5 first presents a comparison of different finite element models for sandwich structures. Then concepts of boundary element method in acoustics are introduced and the boundary element formulations for fluid-structure-fluid interaction are presented. Comparisons of predicted sound transmission loss values of an aluminum panel obtained from numerical analyses, a BEM computer program in MATLAB language and a transmission loss model in a commercial software, LMS SYSNOISE, are provided. Finally, a boundary element analysis model is proposed for three-layer symmetric sandwich panels.

Chapter 6 presents a comprehensive overview of available face sheet and core composite materials. The experimental methods used to obtain the material properties of the face sheets and core of sandwich structures are discussed. Then the estimated material properties of the sandwich panels tested in this study are presented.

Chapter 7 concentrates on dynamic properties of composite sandwich panels used in SEA. The experimental modal densities, radiation loss factors and internal loss factors of four sandwich panels are provided.

Chapter 8 presents experimental and predicted sound transmission loss values of four sandwich panels. Both face sheet and core losses are considered in the wave impedance analysis, and the internal loss factor of the whole structure is used in SEA and boundary element analysis. Conclusions are presented in Chapter 9.

CHAPTER 2

LITERATURE REVIEW

2.1 Wave impedance analysis

Kurtze and Watters [1], in their classic paper, assumed that the face sheets respond as elementary plates in bending, and the core acts as a spacer that has mass and only shear effects in the core are included. They developed the wave impedance of sandwich panels from an equivalent electrical circuit analog. Kurtze and Watters added periodic structures, rigid bridges, in the core to increase the sound insulation. They also illustrated that the loss tangent of the sandwich panel can be equal to that of the core in the mid-frequency region. In the analysis, they assumed that the core is soft but incompressible, and the double-wall resonance frequency is outside the frequency range of interest.

Ford and Walker [2] were the first to describe the effects of dilatational modes of sandwich panels on sound transmission loss. They introduced a dilatational term to describe the translational motion of the core. Then they developed governing equations for the free vibration of sandwich panels from energy relationships. Ford and Walker showed that the dilatational mode of vibration depends primarily on the core thickness and the face sheet masses, and identified the dips in the experimental transmission loss curves as the resonance frequencies for both flexural and dilatational modes.

Smolenski and Krokosky [3] corrected some errors in the work of Ford and Walker [2], and included volumetric and shear terms in the strain energy. They pointed out that in general flexural modes of vibration are insensitive to changes in the Poisson's ratio and thickness of the core, whereas dilatational modes of vibration respond dramatically to changes in these core properties.

The first effort at calculating the sound transmission loss of sandwich panels by using wave impedance analysis is attributed to Dym and Lang [4, 5]. They introduced a set of symmetric and anti-symmetric face sheet displacements as the dependent variables, and retained the dilatational term. Dym and Lang showed that, for identical face sheets, the symmetric and anti-symmetric energies are uncoupled naturally. They developed governing equations for the forced vibration of symmetric sandwich panels by applying Lagrange's principle. Then they derived an expression for the sound transmission coefficient in terms of the anti-symmetric and symmetric wave impedances [5]. They suggested that a high transmission loss can be achieved by choosing the panel properties in such a way so that the symmetric and anti-symmetric impedances have similar values.

Moore and Lyon [6] were the first to investigate symmetric sandwich panels with orthotropic cores. They used a set of symmetric and anti-symmetric displacements which are equivalent to those presented by Smolenski and Krokosky [3]. They showed that a high sound transmission loss can be achieved by using an orthotropic core with a low compressional stiffness and a high shear stiffness, which is quite opposite to the design approach suggested by Kurtze and Watters [1]. This moves the double-wall resonance frequency to a

low frequency, and shifts the coincidence associated with anti-symmetric motion to a high frequency, then the cancellation of the symmetric and anti-symmetric motions of the face sheets produces that the transmission loss results are greater than the mass law values in the mid-frequency region. In their analysis, there is an error in the expression for the stiffness in the rotated axis system for sandwich panels with orthotropic cores.

Narayanan and Shanbhag [61] derived the acceleration for the forced vibration of sandwich panels from the governing equation for sandwich panels presented by Mead and Markus [23] and applied a transmission loss model that is identical to the transmission loss model developed by Dym and Lang [5] to examine theoretically the effects of some core parameters on the sound transmission loss of sandwich panels.

Dym and Lang [7] extended their model for three-layer symmetric sandwich panels with isotropic cores to asymmetric sandwich panels with orthotropic cores. Based on the predictions, they found that when the mass is kept constant, panels with asymmetric configuration have a poorer acoustical performance than those panels with symmetric configuration. The dependence of stiffness on the angle of rotation of the orthotropic material was not considered in their model.

Nilsson [8] presented a free vibration dynamic analysis for sandwich panels with glass reinforced plastic face sheets. The calculation showed that the total loss factor of sandwich panels is primarily determined by the loss factors of the face sheets, at low- and high-frequencies. He treated the sandwich panels as single-layer panels with an equivalent

dynamic bending stiffness in order to calculate the sound transmission loss of the sandwich panels. He also applied an approximation approach derived from SEA to estimate the sound transmission loss of an asymmetric sandwich panel. Though Nilsson discussed the effects of fluid load on sandwich panels and gave an expression for the apparent mass of the water-loaded panel, he assumed that the effects of fluid load cancel out for symmetric sandwich panels.

Jones [10] evaluated various full-sized sandwich construction designs experimentally in a duplex living unit. He pointed out that the measured sound transmission loss values were higher than the mass law values at low frequencies, because of insufficiently diffuse sound fields in the rooms. He found that the sound transmission loss curves of the sandwich panels with paper honeycomb core have smaller coincidence dips, and those dips do not return as rapidly towards the mass law curve as do those of the panels with foam cores. The experimental results also showed that asymmetric sandwich constructions do improve sound insulation.

Huang and Ng [59] presented experimental sound transmission loss results for honeycomb sandwich panels with glass reinforced composite face sheets. They showed the effects of core thickness on sound transmission loss experimentally. They used an incorrect expression for the wave impedance of the sandwich panels to predict the sound transmission loss values. Rajaram *et al.* [60] conducted experimental studies of the sound transmission loss of honeycomb sandwich panels with carbon and glass fiber composite face sheets.

In the analyses of all the papers mentioned above the face sheets of sandwich panels are assumed to be isotropic that in general is not true for high modulus reinforced fiber materials. The orthotropic face sheets are considered in development of governing equations for the forced vibration of sandwich panels in this study.

2.2 Statistical energy analysis

Statistical energy analysis (SEA) is a modeling procedure which uses energy flow relationships for the theoretical estimation of the vibration response levels of and the noise radiation from structures in resonant motion.

Lyon and Maidanik [11] computed the power flow between two random excited, linear oscillators with small coupling between them. They showed that the power flow is proportional to the difference in average modal energies of the two oscillators. Then they extended the model to the coupling between two multimodal systems, and the interaction between a structure and a reverberant acoustic field. Lyon and Maidanik also gave a radiation resistance expression for the coupling of a single mode structure to a reverberant acoustic field.

Smith [12] calculated the response and sound radiation for one linear resonant mode of a structure excited by a pure tone. He extended the model to the case of a structure excited by broadband random noise. Then Smith found that when the modal vibrations are predominantly damped by sound radiation, the mean square velocity is inversely proportional to the modal stiffness.

Maidanik [13] extended the results presented in the two papers discussed above, from a single mode formalism to a multimode formalism using two main assumptions. The number of modes in a combined system is equal to the sum of the numbers of modes of the two systems; and the modal densities of a combined system also are equal to the sum of the modal densities of the two systems. Maidanik computed the radiation resistance of a finite baffled simply supported single-layer panel for individual modes. He also predicted the average modal radiation resistance of a baffled simply supported single-layer panel in a reverberant acoustic field and compared the predicted values with experimental results.

Eichler [15] presented a formulation of statistical energy analysis which includes the relations between the average energies in linear loosely and conservatively coupled systems in terms of modal densities, internal and coupling loss factors. He showed that the products of modal density and coupling loss factor are equal within each pair of subsystems. The noise reduction of a rectangular box was investigated in three frequency regions as presented by Lyon [14]. It was seen that the sound pressure in the box can exceed that in the incidence sound field in both theoretical and experimental cases. Eichler noticed that the predictions from the classical sound transmission predictions were closer to the measured values near the critical frequency, because the theory presented in their analysis only considered the resonant free vibration wave modes.

Crocker and Price [18] presented general power flow relationship equations for a room-panel-room transmission suite. The power flow between the two rooms was defined as the flow between at non-resonant modes, when there are no modes excited in the panel in the

frequency band under consideration. Both non-resonant and resonant vibration modes were taken into consideration. They also provided the experimental determination for the radiation resistance, the coupling factors, the panel response, and the sound transmission loss, derived using SEA. An aluminum panel was tested in a reverberation room and also clamped between two reverberation rooms. Comparisons between experimental and predicted sound transmission loss and radiation resistance values were provided.

Sewell [20] derived an expression for the forced vibration transmission coefficient of a baffled single-layer partition in a reverberant acoustic field using the classical method. The expression for the forced vibration transmission factor is generally valid when the surface mass density of the partition is more than 10 kg/m^2 .

Gomperts [58] provided an expression for the radiation efficiency of a baffled free-edge panel and Oppenheimer and Dubowsky [25] studied the radiation efficiency of an unbaffled simply supported panel. Both of these studies were based on the results developed by Maidanik [13].

The successful prediction of noise and vibration levels of coupled structural elements and acoustic fields using SEA depends to a large extent on an accurate estimate of three parameters, 1) the modal density of each subsystem, 2) the internal loss factor of each subsystem, and 3) the coupling loss factors between the subsystems. Some studies have been carried out in assessing the parameters experimentally.

Clarkson and Pope [21] employed the point mobility technique, developed by Cremer *et al.* [42], to estimate modal densities of flat plates and cylinders. They found that the real part of point mobilities of very lightly damped structures can be negative.

Brown [55] showed that modal density estimates can be improved by using a three-channel spectral analysis which minimizes the erroneous results generated by feedback noise caused by exciter-structure interaction. Brown and Norton [40] showed that the modal density measurement for cylindrical pipes can be further improved by using the three-channel spectral analysis with a mass correction applied to the point mobility measurement. Keswick and Norton [30] used two mass correction methods, the measured mass method and the spectral mass method, to obtain the experimental modal densities of a lightly damped clamped cylindrical pipe. The results showed that the spectral mass method is in better agreement with theory.

Clarkson and Ranky [22] derived an expression for the modal density of honeycomb sandwich panels from a reduced form of the governing equation for sandwich structures presented by Mead and Markus [23] and they evaluated the modal density of honeycomb plates by using a two-channel spectral analysis without mass correction.

Renji and Nair [26] developed an expression for the modal density of a symmetric sandwich panel from a fourth-order equation which was modified from the governing equation of motion for a symmetric laminate by including the shear flexibility of the core. In the work, they considered both real and imaginary parts of the point mobility in the measured mass correction.

The expressions for the modal density of honeycomb sandwich panels given by both Clarkson and Ranky [22] and Renji and Nair [26] were developed from fourth-order governing equations, while most governing equations for symmetric honeycomb sandwich panels are sixth-order [6, 7, 23, 37]. Ferguson and Clarkson [41] presented an expression for the modal density of honeycomb sandwich panels derived from the sixth-order equation presented by Mead and Markus [23]. The expression, however, is incorrect.

Clarkson and Pope [21] used a steady state power flow method to estimate the loss factors of flat plates and cylinders. Ranky and Clarkson [57] compared the power flow method with the enveloped decay method which had been used to obtain internal loss factors of structures. They found that there is no significant difference between the results from the two methods when the modes in the chosen band of frequency have similar modal loss factors. If this is not the case, the decay curve is not a straight line, then the power flow method provides the result required for SEA calculations.

Renji and Narayan [28] investigated loss factors of honeycomb sandwich panels. They corrected the effect of added mass on the driving force by using the measured mass correction method and assumed that the mass loading of the accelerometer, which was employed to measure the spatial velocity of the panel is negligible.

Lyon and Maidanik [11] described the experimental determination for the radiation loss factor of a structure in a reverberant field. Crocker and Price [18] presented the experimental determination for the radiation loss factor of a structure clamped between two reverberation

rooms. Very little published data exist on the radiation loss factors or radiation resistances of sandwich panels.

In this study, an expression for modal densities of sandwich panels is derived from a sixth-order governing equation. The experimental results of radiation loss factors for sandwich panels with different boundary conditions are presented.

2.3 Boundary element analysis

The predictions from SEA are more accurate where sufficient modes in the frequency band under consideration. It is impossible to obtain closed-form expressions for the radiation efficiency for structures with arbitrary boundary conditions. Hence, the details of each mode of finite structures should be considered in the response analysis in order to obtain better predictions at low frequencies. A lot of studies have been carried out in simulating fluid-structure interactions. Three-domain, fluid-structure-fluid systems have been modeled as coupled systems [32, 34] and uncoupled systems [33, 45, 35].

Mariem and Hamdi [32] presented a boundary finite element analysis to compute the sound transmission loss of a baffled panel. The elastic potential energy, the kinetic energy and the work were described in their approach by the displacement of the panel. The radiated sound pressure field was associated with the modified Green's function using the classical formula of Rayleigh. The total load on the panel was given by the pressure step across the panel. The sound radiation from a baffled clamped thin circular panel excited by a normal incident plane wave was computed. The numerical results showed that the radiated

energies can be greater than the incident energy near the first few resonance frequencies. Except near these frequencies, the numerical results agree well with the experimental values. However, there are some errors in the expression for the total load on the panel.

Roussos [45] developed an uncoupled analytical model for the sound transmission loss of a simply supported panel. A Green's function integral equation was used to link the plate vibrations to the transmitted far-field pressure field.

Barisciano [33] studied the sound transmission loss of honeycomb sandwich panels using boundary element and finite element models. The finite elements of honeycomb sandwich panels were constructed using Patran. The computed velocities of the panel excited by fluid forces were imported to a boundary element analysis software as the boundary conditions of the fluid domain. Barisciano treated the fluid-structure-fluid system as an uncoupled system and used an incorrect finite element model for the sandwich panels.

Filippi *et al.* [34] studied the response of a thin elastic rectangular baffled panel in a light fluid excited by an incidence acoustic field. The total load on the panel was assumed to be related to the pressure step across the panel. They only predicted the noise reduction (difference in sound pressure levels) across the panel.

Thamburaj and Sun [35] examined the effects of material and geometrical properties on the theoretical sound transmission loss of a sandwich beam. The governing equations for the sandwich beam were derived by applying Lagrange's principle. They assumed that the external load on the beams is due to the incident and reflected pressures only.

In this work, a boundary element analysis model for the sound transmission loss of three-layer symmetric sandwich panels is proposed. In the model, the fluid-structure-fluid system is treated as a coupled system and the sandwich panel is excited a random incidence field.

CHAPTER 3

WAVE IMPEDANCE ANALYSIS

3.1 Introduction

The wave impedance analysis is used to compute the sound transmission loss of infinite structures. The pressure loads on the structures are associated with the pressures in the incident, reflected, radiated waves at the fluid-structure-fluid interfaces. The pressures in the radiated and transmitted waves depend on the transverse motions of the structure. The transverse vibration of the structure is determined by the pressure loads on the structure, as shown in Fig. 3.1.

Dym and Lang [4, 5] presented a sound transmission loss analysis for symmetric sandwich panels with isotropic cores. They later extended their model to asymmetric sandwich panels with orthotropic cores [7]. They provided the governing differential equations for sandwich panels in matrix form. The dependence of stiffness on the angle of rotation of the orthotropic material was not considered in their model. Moore and Lyon [6] included the angle of rotation effects on stiffness of orthotropic material in their sound transmission loss analysis for symmetric sandwich panels with orthotropic cores. The governing equations for symmetric and anti-symmetric motions of symmetric sandwich panels were presented in matrix form, respectively.

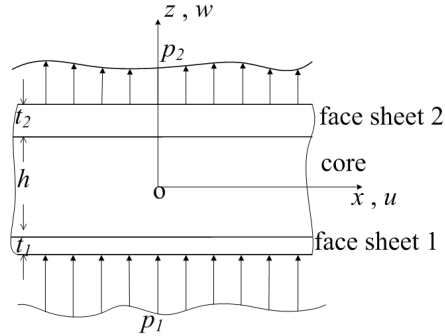


Figure 3.1: The geometry and loads of a sandwich panel

In this study, the governing equations for the forced vibration of symmetric sandwich panels with orthotropic cores developed by Moore and Lyon are extended to asymmetric sandwich panels with orthotropic face sheets and cores. The wave impedance analysis model for the sound transmission loss of asymmetric sandwich panels is provided. The effects of the wave number, wave speed and wave impedance on the prediction of sound transmission loss for sandwich panels are explained. This sound transmission loss analysis model is compared with the model given by Dym and Lang [7]. Then a sixth-order governing equation for anti-symmetric motion of symmetric sandwich panels is derived and compared with the sixth-order differential equations for sandwich panels presented by Mead and Markus [23] and Nilsson and Nilsson [37].

3.2 Governing equations for forced vibration

Both elasticity relationships and energy relationships can be employed to develop governing equations for three-layer sandwich structures. Since it is extremely difficult to obtain

analytical expressions from elasticity relationships, in this study energy relationships were chosen to derive governing equations for asymmetric sandwich panels. Elastic potential and kinetic energies are evaluated in terms of the displacements, and the virtual work done by the pressure loads on the face sheets is also derived in terms of the transverse displacements. Then Lagrange's equations are applied to obtain governing equations for the forced vibration of asymmetric sandwich panels.

The basic assumptions made with three-layer sandwich panels are as follows:

1. the face sheets both stretch and bend along the face sheet-core interface;
2. transverse shear and rotatory inertia effects are neglected in the face sheets;
3. the core is thick compared with the face sheet, and the transverse shear deformation is included;
4. a "dilatational term" is introduced to allow waves to propagate in-plane in the core.

The displacement functions are assumed as follows and are identical to those given by Smolenski and Krokosky [3],

$$u_2 = \left[(u_s + u_a) - \left(z - \frac{h}{2} \right) \frac{\partial w_2}{\partial x} \right] \cos(k_x x), \quad w_2 = (w_s + w_a) \sin(k_x x), \quad (3.1)$$

$$u_c = \left[\left(u_s + \frac{2z}{h} u_a \right) + \zeta \cos \left(\pi \frac{z}{h} \right) \right] \cos(k_x x), \quad w_c = \left(\frac{2z}{h} w_s + w_a \right) \sin(k_x x), \quad (3.2)$$

$$u_1 = \left[(u_s - u_a) - \left(z + \frac{h}{2} \right) \frac{\partial w_1}{\partial x} \right] \cos(k_x x), \quad w_1 = (w_a - w_s) \sin(k_x x), \quad (3.3)$$

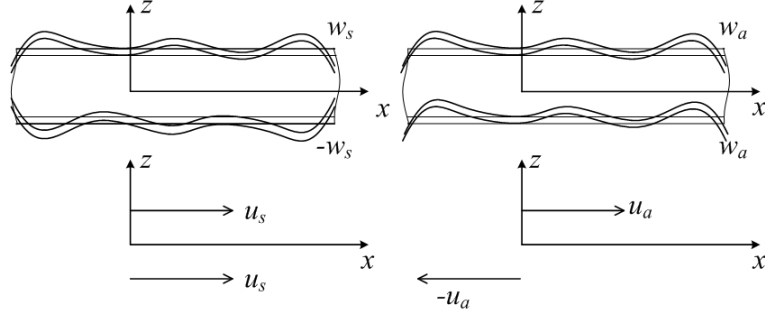


Figure 3.2: Symmetric and anti-symmetric face sheet displacements

where u_j and w_j are the in-plane and transverse displacements for the face sheet j , as shown in Fig. 3.1. u_c and w_c are the in-plane and transverse displacements for the core. The subscripts s and a denote the displacements caused by symmetric and anti-symmetric motions, respectively, as shown in Fig. 3.2. $\zeta \cos(\pi z/h)$ is the dilatational term and k_x is the wave number for the waves in the panel in the x -axis direction.

The transverse displacement functions are used to characterize the transverse deformation as either symmetric, with respect to the middle surface $z = 0$, or anti-symmetric, with respect to that surface $z = \pm(h/2)$. The in-plane displacements of the face sheets are obtained by making $z = \pm(h/2)$ in the core displacement, which gives the displacement at the interface between core and face sheets and adding a term caused by bending, which is zero at the interface between the core and face sheets.

The strains are obtained from the displacement functions in Eqs. (3.1) \sim (3.3):

$$\varepsilon_x = \frac{\partial u}{\partial x} \neq 0, \quad \text{for the face sheets;} \quad (3.4)$$

$$\varepsilon_x = \frac{\partial u}{\partial x} \neq 0, \varepsilon_z = \frac{\partial w}{\partial z} \neq 0, \gamma_{xz} = \frac{\partial w}{\partial x} + \frac{\partial u}{\partial z} \neq 0, \text{ for the core.} \quad (3.5)$$

If all three principal axes for the orthotropic material are aligned with the three axes of the coordinate system, then the elastic potential energy U can be written as follows with

$$\varepsilon_y = \gamma_{xy} = \gamma_{yz} = 0,$$

$$U = \frac{1}{2} \int \int [C_{11}\varepsilon_x^2 + 2C_{13}\varepsilon_x\varepsilon_z + 2C_{15}\varepsilon_x\gamma_{xz} + C_{33}\varepsilon_z^2 + 2C_{35}\varepsilon_z\gamma_{xz} + C_{55}\gamma_{xz}^2] dzdx, \quad (3.6)$$

where C_{ij} is the elastic stiffness constants of the orthotropic material.

Substitution of Eq. (3.4) into Eq. (3.6), yields the elastic potential energy U_j for the face sheets,

$$U_j = \frac{1}{2} \int \int \left[C_{11}^{tj} \left(\frac{\partial u_j}{\partial x} \right)^2 \right] dzdx, \quad j = 1, 2, \quad (3.7)$$

where C_{11}^{tj} is the elastic stiffness constants of the face sheet j .

Similarly, for the orthotropic core, the elastic potential energy U_c becomes,

$$U_c = \int \int \left[\frac{C_{11}}{2} \left(\frac{\partial u_c}{\partial x} \right)^2 + C_{13} \frac{\partial u_c}{\partial x} \frac{\partial w_c}{\partial z} + \frac{C_{33}}{2} \left(\frac{\partial w_c}{\partial z} \right)^2 + \frac{C_{55}}{2} \left(\frac{\partial u_c}{\partial z} + \frac{\partial w_c}{\partial x} \right)^2 \right] dzdx, \quad (3.8)$$

where C_{ij} is the elastic stiffness constants of the core.

If the three axes of the coordinate system are not completely aligned with the three principal axes of the orthotropic material, as shown in Fig. 3.3, the stiffness in the rotated

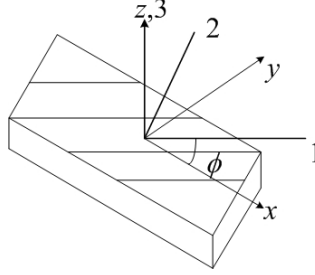


Figure 3.3: The rotated axis system of the orthotropic material

axis system becomes \overline{C}_{ij} instead of C_{ij} ,

$$\overline{C}_{11} = l^4 C_{11} + 2l^2 m^2 (C_{12} + 2C_{66}) + m^4 C_{22}, \quad (3.9)$$

$$\overline{C}_{13} = l^2 C_{13} + m^2 C_{23}, \quad (3.10)$$

$$\overline{C}_{15} = \overline{C}_{35} = 0, \quad (3.11)$$

$$\overline{C}_{33} = C_{33}, \quad (3.12)$$

$$\overline{C}_{55} = m^2 C_{44} + l^2 C_{55}, \quad (3.13)$$

where, ϕ denotes the angle of rotation, $l = \cos \phi$ and $m = \sin \phi$. The details of the derivation of the stiffnesses in the rotated-axis are given in Appendix A.

The kinetic energies are defined as follows, neglecting the rotational energies,

$$T = \frac{1}{2} \int \int \rho \omega^2 (u^2 + v^2 + w^2) dz dx. \quad (3.14)$$

The virtual work done by the pressure loads can be expressed as,

$$W = \int [p_1 w_1 - p_2 w_2] dx = \int [(p_1 - p_2)w_a - (p_1 + p_2)w_s] dx. \quad (3.15)$$

Lagrange's equations are used to obtain the governing equations,

$$\frac{d}{dt} \left(\frac{\partial T}{\partial \dot{q}_r} \right) - \frac{\partial T}{\partial q_r} + \frac{\partial U}{\partial q_r} = \frac{\partial W}{\partial q_r}, \quad (3.16)$$

where q_r is the generalized displacement which includes u_s , w_s , and ζ for the symmetric motion, and u_a , w_a , for the anti-symmetric motion.

The resultant matrix equations are,

$$\begin{bmatrix} D_{11} & D_{12} & D_{13} & D_{14} & D_{15} \\ D_{12} & D_{22} & D_{23} & D_{24} & D_{25} \\ D_{13} & D_{23} & D_{33} & 0 & 0 \\ D_{14} & D_{24} & 0 & D_{44} & D_{45} \\ D_{15} & D_{25} & 0 & D_{45} & D_{55} \end{bmatrix} \begin{Bmatrix} w_s \\ u_s \\ \zeta \\ w_a \\ u_a \end{Bmatrix} = \begin{Bmatrix} -(p_1 + p_2) \\ 0 \\ 0 \\ (p_1 - p_2) \\ 0 \end{Bmatrix}, \quad (3.17)$$

$$\text{with, } D_{11} = \begin{Bmatrix} (C_{11}^{t_1} t_1^3 + C_{11}^{t_2} t_2^3) k_x^4 / 3 + C_{55} h k_x^2 / 3 - (\rho_{sk}^{t_1} t_1^3 + \rho_{sk}^{t_2} t_2^3) \omega^2 k_x^2 / 3 \\ -(\rho_c h / 3) \omega^2 - (\rho_{sk}^{t_1} t_1 + \rho_{sk}^{t_2} t_2) \omega^2 + 4C_{33} / h \end{Bmatrix},$$

$$D_{12} = -(C_{11}^{t_1} t_1^2 + C_{11}^{t_2} t_2^2) k_x^3 / 2 - 2C_{13} k_x + (\rho_{sk}^{t_1} t_1^2 + \rho_{sk}^{t_2} t_2^2) \omega^2 k_x / 2,$$

$$D_{22} = (C_{11}^{t_1} t_1 + C_{11}^{t_2} t_2) k_x^2 + C_{11} h k_x^2 - (\rho_{sk}^{t_1} t_1 + \rho_{sk}^{t_2} t_2) \omega^2 - \rho_c h \omega^2,$$

$$\begin{aligned}
D_{13} &= -4C_{13}k_x/\pi - 4C_{55}k_x/\pi, \quad D_{23} = 2C_{11}hk_x^2/\pi - 2\rho_ch\omega^2/\pi, \\
D_{33} &= C_{11}hk_x^2/2 + \pi^2C_{55}/(2h) - \rho_ch\omega^2/2, \\
D_{14} &= (C_{11}^{t_1}t_1^3 - C_{11}^{t_2}t_2^3)k_x^4/3 - (\rho_{sk}^{t_1}t_1 - \rho_{sk}^{t_2}t_2)\omega^2 - (\rho_{sk}^{t_1}t_1^3 - \rho_{sk}^{t_2}t_2^3)\omega^2k_x^2/3, \\
D_{15} &= D_{24} = -(C_{11}^{t_1}t_1^2 - C_{11}^{t_2}t_2^2)k_x^3/2 + (\rho_{sk}^{t_1}t_1^2 - \rho_{sk}^{t_2}t_2^2)\omega^2k_x/2, \\
D_{25} &= (C_{11}^{t_1}t_1 - C_{11}^{t_2}t_2)k_x^2 - (\rho_{sk}^{t_1}t_1 - \rho_{sk}^{t_2}t_2)\omega^2, \\
D_{44} &= \left\{ \begin{array}{l} (C_{11}^{t_1}t_1^3 + C_{11}^{t_2}t_2^3)k_x^4/3 + C_{55}hk_x^2 - (\rho_{sk}^{t_1}t_1^3 + \rho_{sk}^{t_2}t_2^3)\omega^2k_x^2/3 \\ -\rho_ch\omega^2 - (\rho_{sk}^{t_1}t_1 + \rho_{sk}^{t_2}t_2)\omega^2 \end{array} \right\}, \\
D_{45} &= -(C_{11}^{t_1}t_1^2 + C_{11}^{t_2}t_2^2)k_x^3/2 + 2C_{55}k_x + (\rho_{sk}^{t_1}t_1^2 + \rho_{sk}^{t_2}t_2^2)\omega^2k_x/2, \\
D_{55} &= \left\{ \begin{array}{l} (C_{11}^{t_1}t_1 + C_{11}^{t_2}t_2)k_x^2 + C_{11}hk_x^2/3 + 4C_{55}/h \\ -(\rho_{sk}^{t_1}t_1 + \rho_{sk}^{t_2}t_2)\omega^2 - \rho_ch\omega^2/3 \end{array} \right\},
\end{aligned}$$

where $\rho_{sk}^{t_j}$, t_j denote the mass density and thickness of the face sheet j ; and ρ_c , h denote the mass density and thickness of the core.

The solutions for the transverse displacements can be written in terms of the sound pressure loads,

$$w_s = \frac{F_{11}}{|D|}[-(p_1 + p_2)] + \frac{F_{41}}{|D|}[(p_1 - p_2)], \quad (3.18)$$

$$w_a = \frac{F_{14}}{|D|}[-(p_1 + p_2)] + \frac{F_{44}}{|D|}[(p_1 - p_2)], \quad (3.19)$$

where $|D|$ is the determinant of the matrix \mathbf{D} , and F_{ij} and is the cofactor of element D_{ij} .

Since the matrix \mathbf{D} is a symmetric matrix, then the cofactors must satisfy $F_{ij} = F_{ji}$.

It is convenient to introduce the cofactor ratios,

$$s_1 = \frac{F_{41}}{F_{11}}, \quad s_4 = \frac{F_{14}}{F_{44}}. \quad (3.20)$$

After rearrangement, Eqs. (3.18) and (3.19) become,

$$z_s(i\omega w_s) = -(p_1 + p_2) + s_1(p_1 - p_2), \quad (3.21)$$

$$z_a(i\omega w_a) = -s_4(p_1 + p_2) + (p_1 - p_2), \quad (3.22)$$

where z_a, z_s are the impedances, $z_a = |D|/(i\omega F_{44})$, and $z_s = |D|/(i\omega F_{11})$.

Damping is incorporated by allowing the stiffness constants in the material to become complex,

$$C_{ij}^* = C_{ij}(1 + i\eta), \quad (3.23)$$

where η is the energy loss factor of the material.

For an isotropic material, a special case of an orthotropic material, the stiffness constants are described in terms of the Lamé constant λ and the shear modulus μ ,

$$C_{11} = C_{22} = C_{33} = \lambda + \mu, \quad C_{12} = C_{13} = C_{23} = \lambda, \quad C_{44} = C_{55} = C_{66} = \mu. \quad (3.24)$$

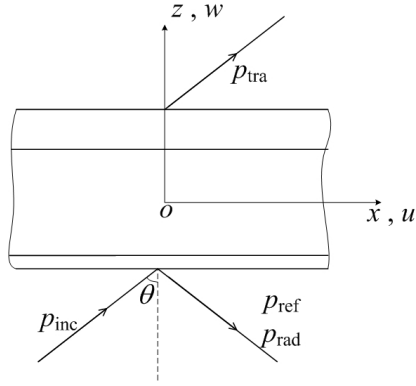


Figure 3.4: Components of pressure fields on a sandwich panel

3.3 Sound transmission loss

Consider a sandwich panel of infinite extent, separating two semi-infinite air spaces as shown in Fig. 3.4. All of the sound waves shown are assumed to be plane waves. Let a pressure wave be incident on the face sheet 1 at an angle θ .

The incident reflected, radiated, and transmitted sound pressures can be expressed as,

$$p_{\text{inc}}(x, z) = P_{\text{inc}} \exp[i(\omega t - kx \sin \theta - kz \cos \theta)], \text{ for } z < 0, \quad (3.25)$$

$$p_{\text{ref}}(x, z) = P_{\text{ref}} \exp[i(\omega t - kx \sin \theta + kz \cos \theta)], \text{ for } z < 0, \quad (3.26)$$

$$p_{\text{rad}}(x, z) = P_{\text{rad}} \exp[i(\omega t - kx \sin \theta + kz \cos \theta)], \text{ for } z < 0, \quad (3.27)$$

$$p_{\text{tra}}(x, z) = P_{\text{tra}} \exp[i(\omega t - kx \sin \theta - kz \cos \theta)], \text{ for } z > 0, \quad (3.28)$$

where P_{inc} , P_{ref} , P_{rad} and P_{tra} are the amplitudes of the incident, reflected, radiated, and transmitted sound pressures, respectively. k is the wave number of sound in air. The

pressure in the reflected wave is assumed to be equal in magnitude to the pressure in the incident wave.

As a result of the matching of the face sheet velocity and the acoustic field velocity at the interface, the radiated pressure can be determined from the acoustic momentum equation,

$$\left. \frac{\partial p_{\text{rad}}}{\partial z} \right|_{z=0} = -i\rho_{\text{air}}\omega\dot{w}_1, \quad (3.29)$$

where ρ_{air} is the mass density of air, and \dot{w}_1 is the transverse velocity of the face sheet 1.

Integrating Eq. (3.29) with respect to z , we have

$$p_{\text{rad}} = -\frac{z_{\text{air}}\dot{w}_1}{\cos\theta} \quad \text{with } z_{\text{air}} = \rho_{\text{air}}c_{\text{air}}, \quad (3.30)$$

where z_{air} is the acoustic impedance of air and c_{air} is the speed of sound in air.

Similarly, the transmitted pressure produced by the transverse motion of the face sheet 2 is,

$$p_{\text{tra}} = \frac{z_{\text{air}}\dot{w}_2}{\cos\theta}, \quad (3.31)$$

where \dot{w}_2 is the transverse velocity of the face sheet 2.

The pressure load on the face sheet 1 is,

$$p_1 = (p_{\text{inc}} + p_{\text{ref}} + p_{\text{rad}})|_{z=0}. \quad (3.32)$$

On the transmission side, the acoustic field pressure is simply the transmitted pressure.

The pressure load on the face sheet 2 is,

$$p_2 = p_{\text{tra}}|_{z=0}. \quad (3.33)$$

Substituting Eq. (3.30) into Eq. (3.32), and Eq. (3.31) into Eq. (3.33), yields the incident and transmitted pressures,

$$2p_{\text{inc}} = p_1 + \frac{z_{\text{air}}}{\cos \theta}(\dot{w}_a - \dot{w}_s), \quad (3.34)$$

$$p_{\text{tra}} = p_2 = \frac{z_{\text{air}}}{\cos \theta}(\dot{w}_a + \dot{w}_s). \quad (3.35)$$

Eliminating p_1 and p_2 from Eqs. (3.34) and (3.35), gives the equations of the transverse velocities in terms of the incident pressure,

$$\begin{bmatrix} z_s + 2z_{\text{air}}/\cos \theta & 2s_1 z_{\text{air}}/\cos \theta \\ 2s_4 z_{\text{air}}/\cos \theta & z_a + 2z_{\text{air}}/\cos \theta \end{bmatrix} \begin{Bmatrix} \dot{w}_s \\ \dot{w}_a \end{Bmatrix} = \begin{Bmatrix} 2p_{\text{inc}}(s_1 - 1) \\ 2p_{\text{inc}}(1 - s_4) \end{Bmatrix}. \quad (3.36)$$

The impedances and cofactor ratios are evaluated by replacing wave-number k_x by $k \sin \theta$ in Eq. (3.17).

The sound transmission coefficient can be evaluated in terms of the impedances and the cofactor ratios,

$$\tau(\theta, \phi) = \left| \frac{p_{\text{tra}}}{p_{\text{inc}}} \right|^2 = \left| \frac{(1 - s_4)z_s/(2z'_{\text{air}}) - (1 - s_1)z_a/(2z'_{\text{air}})}{\left[1 + z_s/(2z'_{\text{air}})\right] \left[1 + z_a/(2z'_{\text{air}})\right] - s_4s_1} \right|^2 \text{ with } z'_{\text{air}} = \frac{z_{\text{air}}}{\cos \theta}, \quad (3.37)$$

$$\tau(\theta, \phi) = \left| \frac{p_{\text{tra}}}{p_{\text{inc}}} \right|^2 = \left| \frac{z_s/(2z'_{\text{air}}) - z_a/(2z'_{\text{air}})}{\left[1 + z_s/(2z'_{\text{air}})\right] \left[1 + z_a/(2z'_{\text{air}})\right] - s_4s_1} \right|^2 \text{ for } s_4z_s = s_1z_a. \quad (3.38)$$

In practice, sound waves are usually incident upon a structure from many angles simultaneously. Therefore an idealized random incidence model is usually assumed, in which plane waves of equal amplitude are incident from all directions with equal probability and which have random phases. The random incidence transmission coefficient, $\bar{\tau}$, is obtained by averaging $\tau(\theta, \phi)$ over all angles of incidence and rotation as follows,

$$\bar{\tau} = \frac{\int_0^{2\pi} \int_0^{\theta_{\text{lim}}} \tau(\theta, \phi) \sin \theta \cos \theta \, d\theta d\phi}{\int_0^{2\pi} \int_0^{\theta_{\text{lim}}} \sin \theta \cos \theta \, d\theta d\phi}. \quad (3.39)$$

Based on field and laboratory measurements [38], the limiting angle θ_{lim} is usually assumed to be 78° .

For sandwich panels with isotropic face sheets and cores, the stiffness constants are independent of the angle of rotation. Then the random incidence transmission coefficient becomes,

$$\bar{\tau} = \frac{\int_0^{\theta_{\text{lim}}} \tau(\theta, \phi) \sin \theta \cos \theta \, d\theta}{\int_0^{\theta_{\text{lim}}} \sin \theta \cos \theta \, d\theta}. \quad (3.40)$$

Finally, the sound transmission loss is defined by

$$\text{TL} = 10 \log_{10} \left(\frac{1}{\bar{\tau}} \right) \text{ dB.} \quad (3.41)$$

3.4 Symmetric sandwich panels

For sandwich panels with identical face sheets, one has

$$C_{11}^{t_1} = C_{11}^{t_2} = C_t, \quad \rho_{sk}^{t_1} = \rho_{sk}^{t_2} = \rho_t, \quad t_1 = t_2 = t. \quad (3.42)$$

Then the symmetric and anti-symmetric motions are uncoupled naturally,

$$D_{14} = D_{15} = D_{24} = D_{25} = 0, \quad s_1 = s_4 = 0. \quad (3.43)$$

The governing matrix equations for symmetric and anti-symmetric motions can be written as follows.

$$[M_s] \begin{Bmatrix} w_s \\ u_s \\ \zeta \end{Bmatrix} = \begin{bmatrix} D_{11} & D_{12} & D_{13} \\ D_{12} & D_{22} & D_{23} \\ D_{13} & D_{23} & D_{33} \end{bmatrix} \begin{Bmatrix} w_s \\ u_s \\ \zeta \end{Bmatrix} = \begin{Bmatrix} -(p_1 + p_2) \\ 0 \\ 0 \end{Bmatrix}, \quad (3.44)$$

$$D_{11} = 2C_t t^3 k_x^4 / 3 + 4C_{33} / h + C_{55} h k_x^2 / 3 - 2m t^2 \omega^2 k_x^2 / 3 - \rho_c h \omega^2 / 3 - 2m \omega^2,$$

$$D_{12} = -C_t t^2 k_x^3 - 2C_{13} k_x + m t \omega^2 k_x, \quad D_{13} = -4C_{13} k_x / \pi - 4C_{55} k_x / \pi,$$

$$D_{22} = 2C_t t k_x^2 + C_{11} h k_x^2 - 2m\omega^2 - \rho_c h \omega^2, \quad D_{23} = 2C_{11} h k_x^2 / \pi - 2\rho_c h \omega^2 / \pi,$$

$$D_{33} = C_{11} h k_x^2 / 2 + \pi^2 C_{55} / 2h - \rho_c h \omega^2 / 2, \text{ and}$$

$$[M_a] \begin{Bmatrix} w_a \\ u_a \end{Bmatrix} = \begin{bmatrix} D_{44} & D_{45} \\ D_{45} & D_{55} \end{bmatrix} \begin{Bmatrix} w_a \\ u_a \end{Bmatrix} = \begin{Bmatrix} p_1 - p_2 \\ 0 \end{Bmatrix}, \quad (3.45)$$

$$D_{44} = 2C_t t^3 k_x^4 / 3 + C_{55} h k_x^2 - 2m t^2 \omega^2 k_x^2 / 3 - \rho_c h \omega^2 - 2m\omega^2,$$

$$D_{45} = 2C_{55} k_x - C_t t^2 k_x^3 + m t \omega^2 k_x,$$

$$D_{55} = 2C_t k_x^2 t + C_{11} h k_x^2 / 3 + 4C_{55} / h - 2(m + \rho_c h / 6) \omega^2,$$

where the surface mass density of a single face sheet is $m = \rho_t t$.

The symmetric and anti-symmetric wave impedances for transverse motion are,

$$z_s = \frac{-(p_1 + p_2)}{i\omega w_s} = \frac{|M_s|}{i\omega \begin{vmatrix} D_{22} & D_{23} \\ D_{23} & D_{33} \end{vmatrix}}, \quad (3.46)$$

$$z_a = \frac{(p_1 - p_2)}{i\omega w_a} = \frac{|M_a|}{i\omega D_{55}} = \frac{1}{i\omega} \left(D_{44} - \frac{D_{45}^2}{D_{55}} \right). \quad (3.47)$$

The contributions of anti-symmetric and symmetric motions to the sound transmission coefficients can be evaluated separately,

$$\tau_a(\theta, \phi) = \left| \frac{1}{1 + z_a / (2z'_{\text{air}})} \right|^2, \quad \tau_s(\theta, \phi) = \left| \frac{1}{1 + z_s / (2z'_{\text{air}})} \right|^2. \quad (3.48)$$

The sound transmission coefficient due to anti-symmetric and symmetric motions is,

$$\tau(\theta, \phi) = \left| \frac{1}{1 + z_s/(2z'_{\text{air}})} - \frac{1}{1 + z_a/(2z'_{\text{air}})} \right|^2. \quad (3.49)$$

If, under particular conditions, $z_s \gg z_a$, in the frequency range of interest, the sound transmission coefficient can be approximated by,

$$\tau(\theta, \phi) \approx \tau_a(\theta, \phi). \quad (3.50)$$

If the two wave impedances are nearly equal in sign and magnitude in certain frequency bands, high transmission loss values are expected in those bands.

The expressions for the governing equations, Eqs. (3.44) and (3.45), the sound transmission coefficient, Eq. (3.49) for symmetric sandwich panels are equivalent to those given by Moore and Lyon [6]. Their expression for the diffuse field transmission coefficient is equivalent to Eq. (3.39). However, they neglected the contribution of C_{66} on the rotated axis stiffness \overline{C}_{11} (see Eq. (3.9)).

3.5 Numerical results

The wave speed and wave impedance for panels provide a way to predict sound transmission characteristics of the panels. The wave speed in a panel is defined by the wave number in the panel and the circular frequency, $c = \omega/k_p$. In the absence of damping, zeros occur in the wave impedance, where the trace wave speed matches the wave speed for freely

propagating waves in the panel, $c_{\text{trace}} = c$. The trace wave speed is defined by the trace wave number in the panel and the circular frequency, and depends on the angle of incidence of the acoustic plane wave,

$$c_{\text{trace}} = \frac{c_0}{\sin \theta}, \quad k_{\text{trace}} = k \sin \theta, \quad c_{\text{trace}} = \frac{\omega}{k_{\text{trace}}}. \quad (3.51)$$

The trace wave speed is always greater than c_0 , the speed of sound in air. It is equal to c_0 at grazing incidence, $\theta = 90^\circ$, and becomes infinite at $\theta = 0^\circ$. Thus, coincidence may occur when the wave speed in the panel is greater than or equal to the speed of sound in air.

The calculated wave numbers for anti-symmetric waves in a symmetric sandwich panel with a honeycomb core are shown in Fig. 3.5. The wave numbers are evaluated from the zeros in the wave impedances assuming zero damping in both the face sheets and core. The face sheets of panel *A* were assumed to be isotropic and the honeycomb core was assumed to be orthotropic. The properties of panel *A* are given in Table 3.1. The wave numbers for the orthotropic core are dependent on the propagation direction of the incident acoustic wave relative to the principal axes in the honeycomb core. The four solid curves denote the wave numbers along the directions where the angles of rotation ϕ are equal to 0° , 30° , 60° and 90° , from top to bottom in the figure.

Two parallel dotted lines are indicated in Fig. 3.5. The lower dotted line corresponds to the wave number k_l for pure bending of the entire panel. The upper dotted line represents the wave number k_u for flexural waves propagating in a single face sheet loaded with half

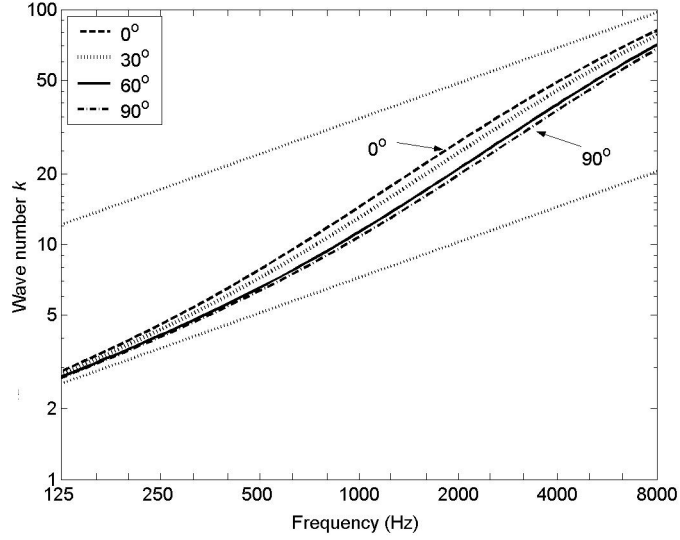


Figure 3.5: Predicted wave numbers for anti-symmetric waves in panel *A*

the mass of the core.

$$k_l = \left[\frac{(2\rho_t t + \rho_c h) \omega^2}{C_t (h^2 t/2 + h t^2 + 2t^3/3)} \right]^{1/4}, \quad k_u = \left[\frac{(\rho_t t + \rho_c h/2) \omega^2}{C_t t^3/12} \right]^{1/4}. \quad (3.52)$$

It is seen that the wave number of the first propagating mode for anti-symmetric motion of the panel asymptotically approaches the lower line for decreasing frequencies. In the high frequency region the upper line is the asymptote. The differences between the four solid curves become smaller when the curves approach either the lower or upper lines. Thus, the anti-symmetric motion of the panel is mainly determined by the pure bending stiffness of the entire panel in the low frequency region, and by the bending stiffness of one face sheet loaded with half the mass of the core in the high frequency region.

The wave numbers for symmetric waves in panel A along the four directions were also calculated. It was found that the wave numbers for symmetric waves are complex below 6000 Hz.

The predicted wave speeds for anti-symmetric and symmetric waves in panel A are shown in Figs. 3.6 and 3.7. The dotted horizontal lines indicate the speed of sound in air in both figures. It was found that anti-symmetric waves of panel A travel fastest along $\phi = 90^\circ$ and slowest along $\phi = 0^\circ$. The anti-symmetric wave speeds exceed the speed of sound in air near to 200 Hz.

No freely propagating symmetric waves in the four directions exist below 6000 Hz. The near vertical lines indicate the freely propagating symmetric waves in the panel, which travel at high speeds and which depend considerable on frequency. This behavior is similar to a double wall resonance.

$$f_w = \frac{1}{2\pi} \sqrt{\frac{C_{33}}{h(2\rho_t t + \rho_c h/3)}}. \quad (3.53)$$

For panel A , the double wall resonance frequency is about 5200 Hz. At double wall resonance, the face sheet motions are uniform, which corresponds to a trace wave number of zero and to an infinite wave speed. An incident wave at normal incidence excites symmetric panel motion at frequencies near the double wall resonance. The wave speeds for symmetric waves do not monotonically increase with increasing frequency as those for anti-symmetric

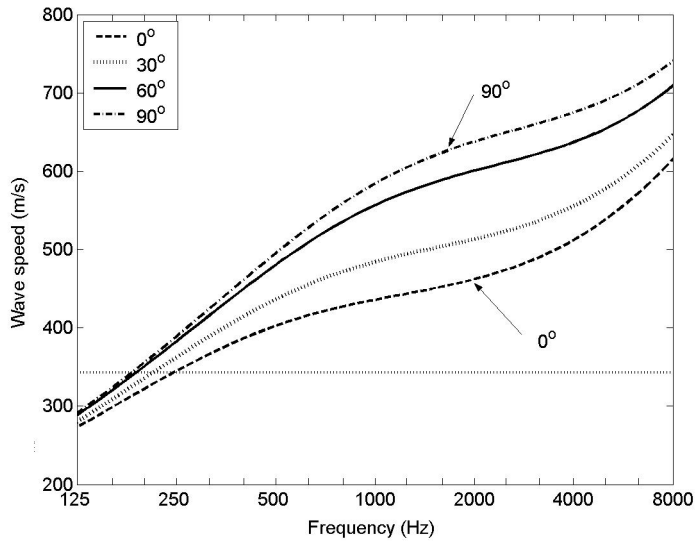


Figure 3.6: Predicted wave speeds for anti-symmetric motion of panel *A*

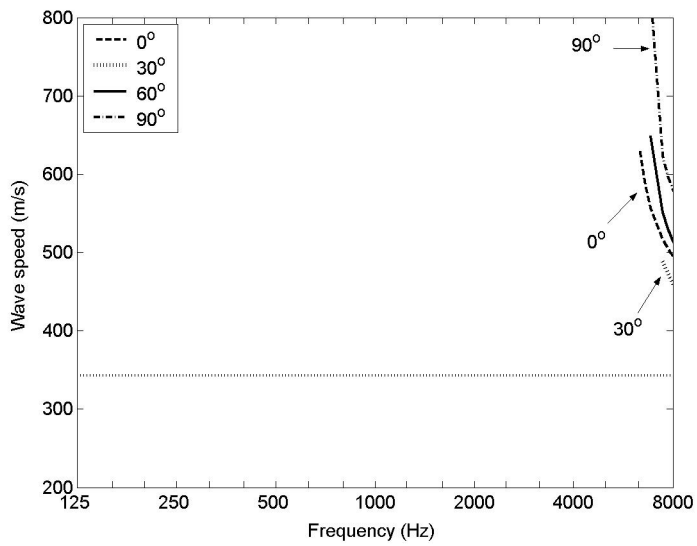


Figure 3.7: Predicted wave speeds for symmetric motion of panel *A*

waves do. The speeds of freely symmetric waves are greater than the speed of sound in air in the frequency range of interest.

In the absence of damping, the wave impedances are imaginary. The wave impedances were calculated for the two waves in $\phi = 0^\circ, 90^\circ$ directions at oblique incidence $\theta = 76.5^\circ$, as shown in Fig. 3.8. It is seen that anti-symmetric coincidences occur near to 250 Hz and no symmetric coincidence occurs in the frequency range of interest. The symmetric impedance is insensitive to the propagation direction in panel *A*. A dip in the symmetric wave impedance occurs near to 4000 Hz, below the double wall resonance frequency. The symmetric wave impedances are much higher than the anti-symmetric wave impedances below 2000 Hz for this oblique angle of incidence. The sound transmission loss values caused by anti-symmetric or symmetric wave motions are compared with the predictions of sound transmission loss generated by both motions for panel *A*, as shown in Fig. 3.9.

Since most measured sound transmission loss results for sandwich panels are presented in one-third octave bands, the predicted sound transmission loss values were frequency-averaged for comparison purpose. The transmission loss of panel *A* is dominated by the anti-symmetric motion in the frequency range of interest. The contribution of the symmetric motion is negligible up to 5000 Hz. The coincidence dip near to 250 Hz is associated with anti-symmetric motion of panel *A*, which is consistent with the wave speed curves. The sound transmission loss values of panel *A* were calculated and are compared with the measured transmission loss results given in Ref. [6], as shown in Fig. 3.10. The predictions were generated for two different values of energy loss factor of the core.

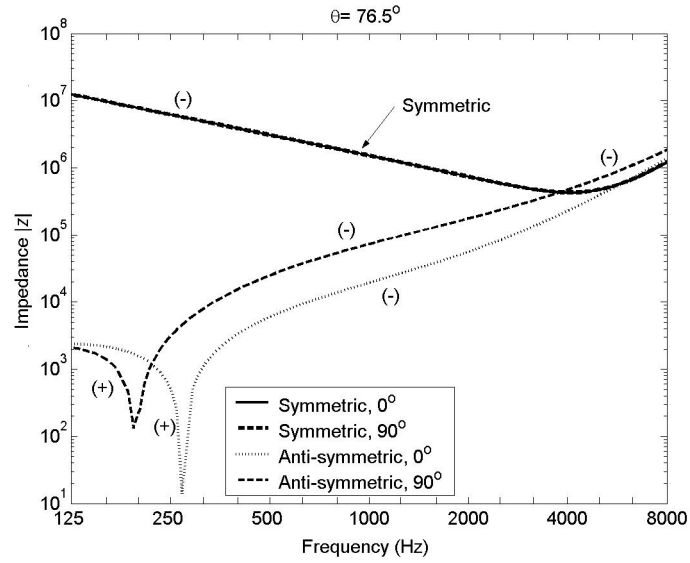


Figure 3.8: Wave impedances along two principal directions for panel A

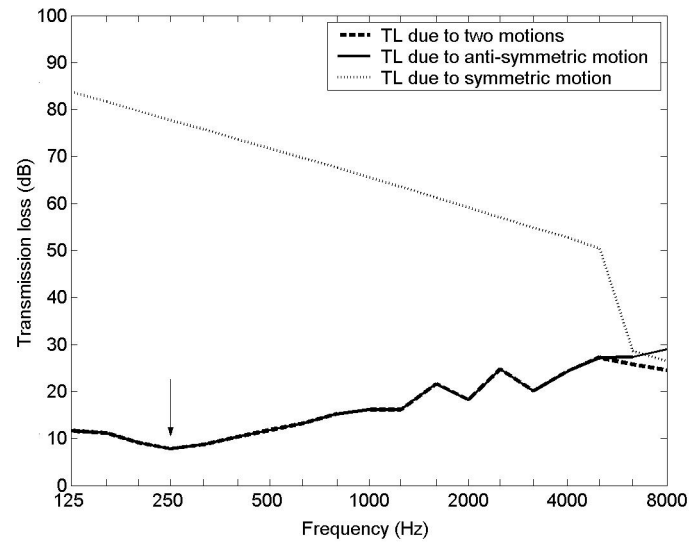


Figure 3.9: Calculated sound transmission loss values of panel A without damping

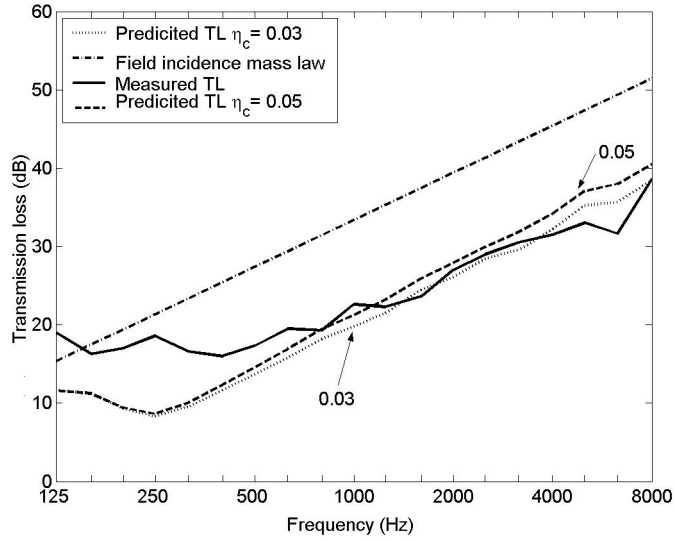


Figure 3.10: Predicted and measured sound transmission loss values of panel A

The effects of core damping are noticeable at frequencies above the onset of coincidence, where the core stiffnesses affect the sound transmission loss of the panel. The transmission loss curves do not return to the mass law curve at frequencies above coincidence, and are separated by more than 10 dB.

Theoretically, when the wave impedances for anti-symmetric and symmetric motions are equal in sign and magnitude, there is no transmitted sound pressure. So the transmission loss can exceed mass law values when the two wave impedances have similar values. This behavior has been demonstrated analytically and experimentally for a honeycomb sandwich panel in Ref. [6]. This acoustical behavior is a result of the cancellation of symmetric and anti-symmetric motions of the face sheets. The honeycomb core was uncommonly orientated so that the cells lay in the plane of the panel. The wave impedances of two motions along

Table 3.1: Properties of sandwich panels *A* and *B*

	Property	Panel <i>A</i>	Panel <i>B</i>
Face	Surface mass density m (kg/m ²)	4.17	5.7
Sheet	Stiffness C_{11}^t (GPa)	7.0	7.0
	Thickness t (mm)	6.35	9.53
Core	Density ρ_c (kg/m ³)	28	21
	Thickness h (mm)	76.2	84.1
	C_{11} (MPa)	4.0	0.4
	C_{22} (MPa)	4.0	95
	C_{33} (MPa)	370	0.4
	C_{44} (MPa)	50	7.6
	C_{55} (MPa)	23	0.17
	C_{66} (MPa)	0.2	4.2
	$C_{12} = C_{13} = C_{23}$ (MPa)	0.5	0.04
	Energy loss factor η_c	0.03, 0.05	0.03

$\phi = 0^\circ, 90^\circ$ at oblique incidence $\theta = 76.5^\circ$ for panel *B* are shown in Fig. 3.11. The first symmetric coincidence occurs near to 200 Hz, and the second symmetric coincidence and the first anti-symmetric coincidence are around 2000 Hz. It is seen that, in the frequency region $f > 400\text{Hz}$, the wave impedances are nearly equal in sign and magnitude. Thus high transmission loss values are expected above 400 Hz.

Sound transmission loss values of panel *B* were calculated and are compared with the measured results given in Ref. [6], as shown in Fig. 3.12. The predictions were generated for three different values of energy loss factor of the core. It is seen that damping does not have a noticeable effect on the sound transmission loss of panel *B* in the region $200\text{ Hz} < f < 2000\text{ Hz}$, between two symmetric coincidences.

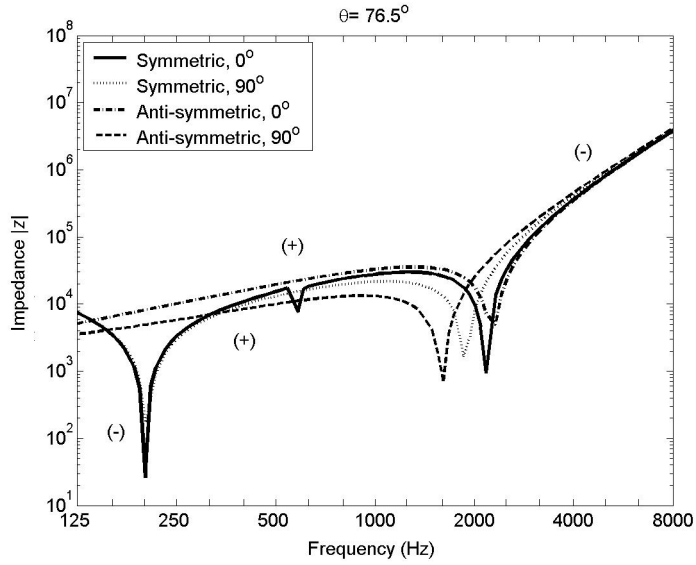


Figure 3.11: Wave impedances along two principal directions for panel *B*

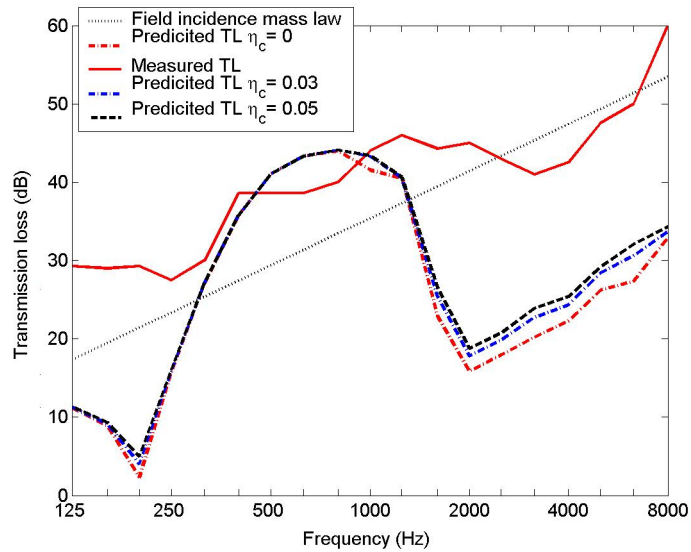


Figure 3.12: Predicted and measured sound transmission loss values of panel *B*

3.6 Other TL models for asymmetric sandwich panels

Dym and Lang [7] have presented a sound transmission loss analysis for asymmetric sandwich panels with orthotropic cores. In their model, the displacement functions of the face sheets and the core are written as,

$$u_2 = \left(\bar{u} - \frac{h}{2} \frac{\partial \bar{w}}{\partial x} \right) + \left(\tilde{u} - \frac{h}{2} \frac{\partial \tilde{w}}{\partial x} \right) - \left(z - \frac{h}{2} \right) \frac{\partial w_2}{\partial x}, w_2 = \tilde{w} + \bar{w}; \quad (3.54)$$

$$u_c = \left(\bar{u} - \frac{h}{2} \frac{\partial \bar{w}}{\partial x} \right) + \frac{2z}{h} \left(\tilde{u} - \frac{h}{2} \frac{\partial \tilde{w}}{\partial x} \right) + g \cos \left(\frac{\pi z}{h} \right), w_c = \frac{2z}{h} \bar{w} + \tilde{w}; \quad (3.55)$$

$$u_1 = \left(\bar{u} - \frac{h}{2} \frac{\partial \bar{w}}{\partial x} \right) - \left(\tilde{u} - \frac{h}{2} \frac{\partial \tilde{w}}{\partial x} \right) - \left(z + \frac{h}{2} \right) \frac{\partial w_1}{\partial x}, w_1 = \tilde{w} - \bar{w}; \quad (3.56)$$

where \bar{w} , \bar{u} and g are for the symmetric motion, and \tilde{u} , \tilde{w} are for the anti-symmetric motion, respectively. They assumed that all displacements are in phase,

$$\bar{u}, \bar{w}, g, \tilde{u}, \tilde{w} \sim \exp[i(\omega t - kx \sin \theta)], \quad (3.57)$$

while the transverse displacements and the in-plane displacements are assumed to be out of phase in other works [2, 3, 6].

It is noted that the displacement functions assumed in section 3.2 are equal to those in Eqs. (3.54) ~ (3.56), if

$$u_s = \bar{u} - \frac{h}{2} \frac{\partial \bar{w}}{\partial x}, g = \zeta, w_s = \bar{w}, \text{ and } u_a = \tilde{u} - \frac{h}{2} \frac{\partial \tilde{w}}{\partial x}, w_a = \tilde{w}. \quad (3.58)$$

Dym and Lang applied equations the same to Eqs. (3.7), (3.8), (3.14) and (3.15) to evaluate the elastic potentials, the kinetic energies of the sandwich panel, and the potential for surface pressures, respectively. But they introduced a shear correction factor κ in the transverse shear strain of the core, γ_{xz} . Applying Hamilton's principle, they derived the governing differential equations for the forced motion,

$$\begin{bmatrix} B_{11} & B_{12} & B_{13} & B_{14} & B_{15} \\ B_{12} & B_{22} & B_{23} & B_{24} & B_{25} \\ B_{13} & B_{23} & B_{33} & 0 & 0 \\ B_{14} & B_{24} & 0 & B_{44} & B_{45} \\ B_{15} & B_{25} & 0 & B_{45} & B_{55} \end{bmatrix} \begin{Bmatrix} \bar{w} \\ \bar{u} \\ g \\ \tilde{w} \\ \tilde{u} \end{Bmatrix} = \begin{Bmatrix} -(p_1 + p_2) \\ 0 \\ 0 \\ (p_1 - p_2) \\ 0 \end{Bmatrix}. \quad (3.59)$$

The elements of the matrix \mathbf{B} are given in Appendix B.

Since the in-plane displacement functions in their model are not the same as those used in our model, Eq. (3.1), and the factor κ is in the elastic potential of the core, the matrix \mathbf{B} is not equivalent to the matrix \mathbf{D} in Eq. (3.17). Thus the wave impedances computed from this model are not the same as those from our model.

Dym and Lang developed the sound transmission coefficient of asymmetric sandwich panels using the same approach described in Sec. 3.3. However, they neglected the dependence of the stiffness of orthotropic materials on the angle of rotation ϕ between the axes of the coordinate system and the principal axes of the orthotropic materials. Then they

Table 3.2: Properties of sandwich panel C

	Property	Panel C
	Density $\rho_1 = \rho_2$ (kg/m ³)	985.0
Face	Young's modulus $E_1 = E_2$ (GPa)	4.71
Sheet	Thickness $t_1 = t_2$ (mm)	3.68
	Poisson's ration $\nu_1 = \nu_2$	0.3
	Loss factor $\eta_1 = \eta_2$	0.01
	Density ρ_c (kg/m ³)	30
	Thickness h (mm)	50.7
Core	Lame constant λ (MPa)	21.57
	Shear modulus μ (MPa)	2.14
	Energy loss factor η_c	0.03

did not consider the dependence of the angle of rotation in the random incidence transmission coefficient calculation. The random incidence transmission coefficient $\bar{\tau}$ is defined Eq. (3.40), so it is only valid for sandwich panels with isotropic materials.

No experimental data for sandwich panels with asymmetric configurations are available in the literature. Dym and Lang [7] have studied the effects of the face sheet thicknesses of panel C . The properties of panel C are given in Table 3.2.

The predicted wave impedances for two wave motions at oblique incidence $\theta = 76.5^\circ$ from the present model and Dym and Lang's model are shown in Fig. 3.13. The predictions are almost the same except near coincidence. The symmetric coincidence of panel C is near to 1600 Hz, while the anti-symmetric coincidence is above 8000 Hz for this oblique incidence. It was found that in the frequency range $6300 \text{ Hz} > f > 3150 \text{ Hz}$, the two wave impedances are nearly equal in sign and magnitude, at this oblique coincidence. Thus high transmission loss values are expected in this region for panel C .

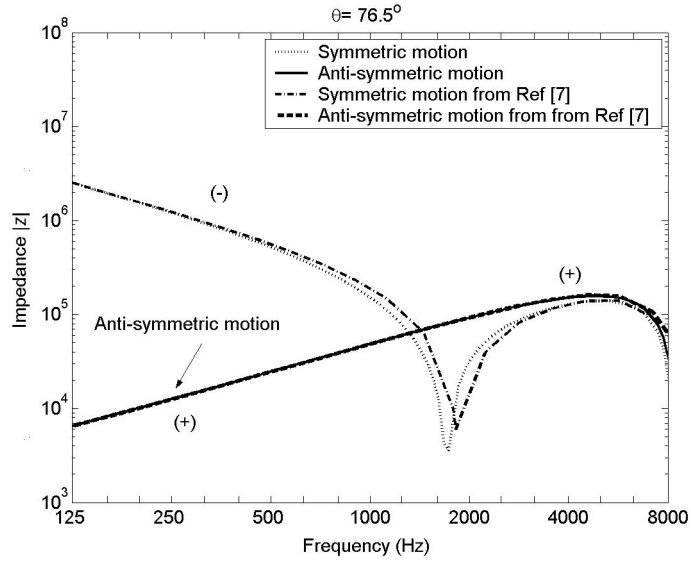


Figure 3.13: Calculated wave impedances for symmetric panel C

The transmission loss values of panel C with asymmetric configurations were calculated and are shown in Figs. 3.14 and 3.15. To avoid the effects introduced by adding mass, the sum of the face sheet thicknesses, $t_1 + t_2$, was fixed, and the ratio of the face sheet thicknesses t_1/t_2 was varied for panel C . Since the face sheets and core of panel C were assumed to be isotropic, the discrepancy between the two models is caused by the differences in the displacement functions and the elastic potential of the core. The two models produce similar transmission loss values. At low frequencies, below where symmetric coincidence occurs for the panels the predicted sound transmission loss results follow the field incidence mass law transmission loss curve.

The predicted sound transmission loss values exceed mass law values in some regions, especially for the symmetric configuration, $t_1 = t_2$. This behavior is the result of the

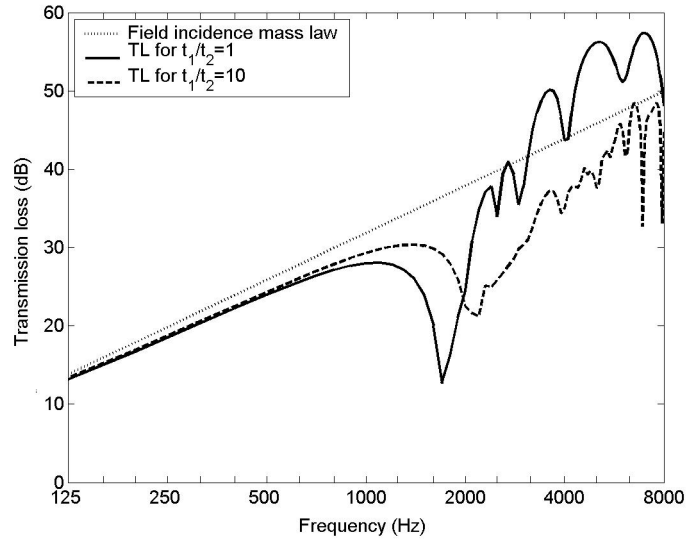


Figure 3.14: Predicted sound transmission loss values of panel *C* from Dym and Lang's model

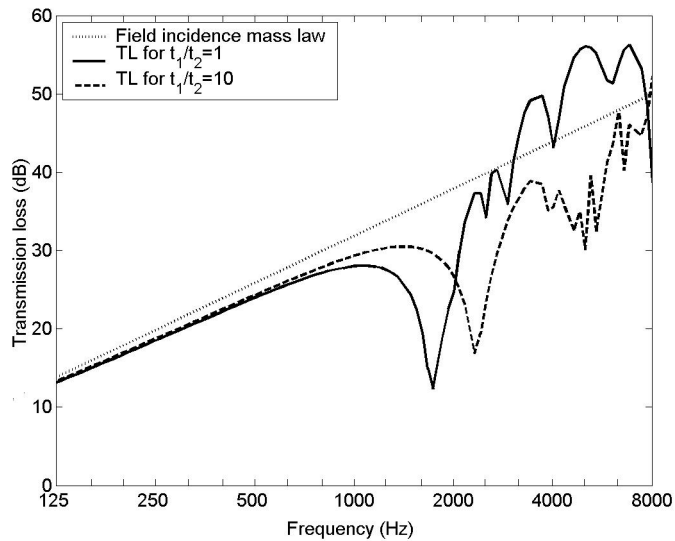


Figure 3.15: Predicted sound transmission loss values of panel *C* from the present analysis

cancellation of the symmetric and anti-symmetric motions of the face sheets. The symmetric configuration enhances the cancellation. Asymmetric configurations of the sandwich panel, $t_1 \neq t_2$, exhibit some improvement in sound isolation near coincidence.

3.7 Other governing equations for anti-symmetric motion

When the transverse vibration is dominated by anti-symmetric transverse vibration, the governing equation for transverse vibration of symmetric sandwich panels becomes,

$$q = \left[\begin{array}{c} 2C_t t^3 k_x^4 / 3 + C_{55} h k_x^2 - 2m t^2 \omega^2 k_x^2 / 3 - \mu \omega^2 \\ - \frac{(2C_{55} k_x - C_t k_x^3 t^2 + m \omega^2 k_x t)^2}{2C_t t k_x^2 + C_{11} h k_x^2 / 3 + 4C_{55} / h - 2(m + \rho_c h / 6) \omega^2} \end{array} \right] w, \quad (3.60)$$

where the pressure step across the panel is, $q = p_1 - p_2$, and the surface mass density is $\mu = \rho_c h + 2m$.

The governing equation can be written in the alternative form,

$$\left[A k_x^6 + B k_x^4 + C k_x^2 + D \right] w = \left[\left(1 + \frac{C_{11} h}{6 C_t t} \right) k_x^2 + \frac{2 C_{55}}{h C_t t} - \frac{1}{C_t t} \left(m + \frac{\rho_c h}{6} \right) \omega^2 \right] q, \quad (3.61)$$

$$\begin{aligned} \text{where, } A &= \frac{C_t t^3}{6} \left(1 + \frac{2 C_{11} h}{3 C_t t} \right), \quad D = \frac{\omega^2}{2 C_t t} \mu \left[\omega^2 \left(2m + \frac{\rho_c h}{3} \right) - \frac{4 C_{55}}{h} \right], \\ B &= C_{55} \left[\frac{(t+h)^2}{h} + \frac{t^2}{3h} + \frac{C_{11} h^2}{6 C_t t} \right] - \omega^2 \left[\frac{t^2}{3} \left(m + \frac{\rho_c h}{3} \right) - \frac{m t h C_{11}}{9 C_t} \right], \\ C &= \omega^2 \left\{ \frac{m t^2 \omega^2}{6 t C_t} \left[\frac{2 \rho_c h}{3} + m \right] - \left(1 + \frac{h C_{11}}{6 t C_t} \right) \mu - \frac{C_{55}}{t C_t} \left[\frac{\rho_c h^2}{6} + m \left(\frac{(t+h)^2}{h} + \frac{2 t^2}{3 h} \right) \right] \right\}. \end{aligned}$$

When the stiffnesses of the face sheets are much greater than the stiffnesses of the core, and high order ω^2 terms are negligible, the governing equation becomes,

$$\left[Ak_x^6 + Bk_x^4 + Ck_x^2 + D \right] w = \left[k_x^2 + \frac{2C_{55}}{hC_{tt}} \right] q, \quad (3.62)$$

$$\text{where, } A = \frac{C_{tt}t^3}{6}, B = C_{55} \left[\frac{(t+h)^2}{h} + \frac{t^2}{3h} \right], C = \omega^2 \{-\mu\}, D = \frac{\omega^2}{2C_{tt}} \mu \left(-\frac{4C_{55}}{h} \right).$$

Mead and Markus [23] presented an equation of motion in terms of the transverse displacement for a three-layer damped sandwich beam with a viscoelastic core. In their analysis, rotatory inertia was ignored and elasticity relationships were applied to derive the sixth-order differential equation:

$$\frac{\partial^6 w}{\partial x^6} - g(1+Y) \frac{\partial^4 w}{\partial x^4} + \frac{\mu}{D_t} \left(\frac{\partial^4 w}{\partial x^2 \partial t^2} - g \frac{\partial^2 w}{\partial t^2} \right) = \frac{1}{D_t} \left(\frac{\partial^2 q}{\partial x^2} - gq \right), \quad (3.63)$$

where q is the total load, D_t is the bending rigidity of a single face sheet, g is the shear parameter, Y is the geometric parameter and μ is the surface mass density of the panel.

For symmetric sandwich panels, the parameters can be evaluated as,

$$D_t = \frac{E_t t^3}{6(1-\nu_t^2)}, g = \frac{2C_{55}}{ht} \frac{1-\nu_t^2}{E_t}, Y = (h+t)^2 \frac{E_t t}{2(1-\nu_t^2)D_t}, \mu = \rho_c h + 2m. \quad (3.64)$$

The governing Eq. (3.63) can be written as follows,

$$\left[A'k_x^6 + B'k_x^4 + C'k_x^2 + D' \right] w = \left[k_x^2 + \frac{2C_{55}}{ht} \frac{1 - \nu_t^2}{E_t} \right] q, \quad (3.65)$$

$$\text{where, } A' = \frac{E_t t^3}{6(1 - \nu_t^2)}, \quad B' = \frac{C_{55} t^2}{3h} + \frac{C_{55}(t+h)^2}{h}, \quad C' = -\mu\omega^2, \quad D' = -\frac{2C_{55}\mu\omega^2(1 - \nu_t^2)}{C_t t h}.$$

The equation above is identical to Eq. (3.62), which is an approximate expression for Eq. (3.61) under certain conditions.

The impedance is given by,

$$z = \frac{q}{i\omega w} = \frac{1}{i\omega} \left\{ -\mu\omega^2 + \frac{D_t[k^6 + g(1+Y)k^4]}{k^2 + g} \right\}. \quad (3.66)$$

Nilsson and Nilsson [37] have presented an equation of motion for a three-layer symmetric sandwich beam. In their analysis, rotatory inertia effects were considered and energy relationships were applied to derive the sixth-order differential equation.

$$\begin{aligned} -2D_2 \frac{\partial^6 w}{\partial x^6} + \frac{2D_2}{D_1} I_\rho \frac{\partial^6 w}{\partial x^4 \partial t^2} - \left(\mu + \frac{2D_2}{D_1} \mu + \frac{I_\rho G_e h}{D_1} \right) \frac{\partial^4 w}{\partial x^2 \partial t^2} + G_e h \left(\frac{\partial^4 w}{\partial x^4} + \frac{\mu}{D_1} \frac{\partial^2 w}{\partial t^2} \right) \\ + \frac{I_\rho}{D_1} \mu \frac{\partial^4 w}{\partial t^4} = - \left(1 + \frac{2D_2}{D_1} \right) \frac{\partial^2 q}{\partial x^2} + \frac{G_e h}{D_1} q + \frac{I_\rho}{D_1} \frac{\partial^2 q}{\partial t^2}, \end{aligned} \quad (3.67)$$

where D_1 is the bending rigidity of the entire beam, D_2 is the bending rigidity of a single face sheet, I_ρ is the mass moment of inertia, G_e is the equivalent shear stiffness, and μ is

the surface mass density of the beam.

$$D_1 = \frac{E_1 h^3}{12(1-\nu_c^2)} + \frac{E_1^t}{(1-\nu_t^2)} \left(\frac{h^2 t}{2} + ht^2 + \frac{2t^3}{3} \right), \quad D_2 = \frac{E_1^t t^3}{12(1-\nu_t^2)},$$

$$I_\rho = \frac{\rho_c h^3}{12} + \rho_t \left(\frac{h^2 t}{2} + ht^2 + \frac{2t^3}{3} \right), \quad G_e = \frac{C_{55}(t+h)^2}{h^2}, \quad \mu = \rho_c h + 2m.$$

The governing equation (3.67) can be written as ,

$$\left[2D_2 k^6 + \left(G_e h - \frac{2D_2}{D_1} I_\rho \omega^2 \right) k^4 - \left(\mu + \frac{2D_2}{D_1} \mu + \frac{I_\rho G_e h}{D_1} \right) k^2 \omega^2 - \left(G_e h - I_\rho \omega^2 \right) \frac{\mu \omega^2}{D_1} \right] w$$

$$= \left[\frac{G_e h}{D_1} + \left(1 + \frac{2D_2}{D_1} \right) k^2 - \frac{I_\rho}{D_1} \omega^2 \right] q. \quad (3.68)$$

The impedance is,

$$z = \frac{q}{i\omega w} = \frac{1}{i\omega} \left\{ -\mu \omega^2 + \frac{2D_2 k^6 + \left(G_e h - \frac{2D_2}{D_1} I_\rho \omega^2 \right) k^4 - \frac{I_\rho G_e h}{D_1} k^2 \omega^2}{\frac{G_e h}{D_1} + \left(1 + \frac{2D_2}{D_1} \right) k^2 - \frac{I_\rho}{D_1} \omega^2} \right\}. \quad (3.69)$$

The sound transmission coefficient can be evaluated by Eq. (3.48). The predicted sound transmission loss values of panel *A* obtained by using the wave impedances computed from the three governing equations are compared with the measured results, as shown in Fig. 3.16. The energy loss factor in the core was assumed to be 0.03 for all three cases. The three governing equations generate similar transmission loss predictions for panel *A* in the region between 250 Hz and 4000 Hz, where the anti-symmetric transverse displacement is dominant.

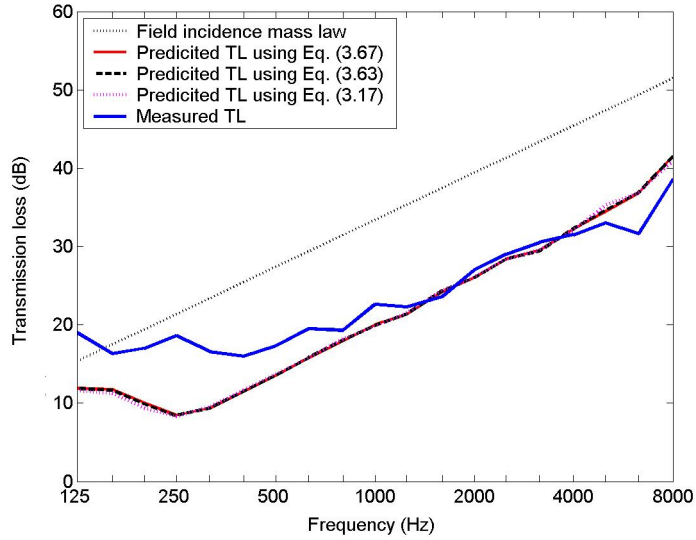


Figure 3.16: Predicted sound transmission loss values of panel *A* made using governing equations

3.8 Conclusions

The wave impedance analysis provides the sound transmission loss of infinite sandwich panels. If damping is included in the theoretical calculations, the effect is noticeable above coincidence, where the stiffnesses of the face sheets and core affect the sound transmission loss of the panels. For sandwich panels with stiff cores, typical honeycomb cores, anti-symmetric coincidence occurs at low frequencies, and symmetric coincidence is at high frequencies. Thus, in the frequency range of interest, the anti-symmetric wave motion is dominant. The sound transmission loss caused by anti-symmetric wave motion provides an accurate approximation of the sound transmission loss produced by anti-symmetric and symmetric motions. For sandwich panels with soft cores, the sound transmission loss values

can exceed the mass law values because of the cancellation of symmetric and anti-symmetric motions of the face sheets. This acoustical behavior occurs in the frequency region between symmetric and anti-symmetric coincidence. Asymmetric configurations lessen the cancellation of symmetric and anti-symmetric motions of the face sheets, and produce some improvement in sound isolation near coincidence.

CHAPTER 4

STATISTICAL ENERGY ANALYSIS

4.1 Introduction

The modal vibration of a finite panel consists of standing waves. Each standing wave can be considered to be composed of two wave types: forced traveling waves set up by external loads and free (reflected) waves that are generated by secondary and necessary to satisfy at the boundaries. There is little hope to obtain a detailed classical solution for a finite panel because of the existence of many modes of vibration. For panels excited by broadband noise, the detailed response characteristics may be neglected and statistical properties such as mean square values and power spectra can be used to provide an approximate measure of vibration.

Statistical energy analysis (SEA) was developed from studies of the power flow of two randomly excited linearly coupled oscillators in the 1960's. It was found that for conservative coupling the power flow is proportional to the average modal energy difference between two oscillators. A thermal argument concludes that the products of modal density and coupling loss factor are equal in the two coupled oscillators [11]. The modal averaged radiation resistance of a baffled simply supported single-layer panel excited by a reverberant field was derived by Maidanik [13]. Later this analysis was extended from systems consisting of two subsystems to multiple subsystems [39]. Crocker and Price [18] presented a three-subsystem

SEA model to estimate the sound transmission loss of a single-layer panel with both resonant and non-resonant modes under consideration. Price and Crocker [19] presented a five-subsystem SEA model to estimate sound transmission through a double wall.

In this chapter, the assumptions and concepts of SEA are briefly reviewed. A three-subsystem SEA model for a transmission suite is introduced. An analytical expression for modal densities of sandwich panels is derived from a sixth-order governing equation. The expression is compared with other analytical expressions for modal densities of sandwich panels [22, 41]. The sound transmission loss of the structure between two reverberation rooms is developed. Then the sound transmission loss estimates for a single-layer panel and a honeycomb sandwich panel are compared with those experimental values given in Refs. [6, 18]. The effects of test area of the panels and volume of the rooms' acoustic spaces on sound transmission loss are also studied.

4.2 Assumptions and concepts

The fundamental assumptions made in SEA are:

1. the couplings between the different subsystems are small, linear and conservative;
2. the power flows are between the subsystems having resonance frequencies in the band of interest;
3. the subsystems are excited by broadband random excitation;
4. the total motion is regarded as a sum of independent motions in individual modes;

5. equipartition of energy exists between all modes at resonance within a given frequency band in a given subsystem.

An individual oscillator driven in steady state conditions at a single frequency has potential and kinetic energy stored within it. The power dissipated via the damping is related to the energy stored in the oscillator.

$$\Pi_{\text{diss}} = c_v \dot{x}^2 = 2\zeta\omega_n m \dot{x}^2 = 2\zeta\omega_n E = \omega_n \eta E, \quad (4.1)$$

where c_v is the viscous damping coefficient, ζ is the damping ratio, ω_n is the radian natural frequency, m is the oscillator mass, E is the stored energy, and η is the energy loss factor.

The power dissipation concepts for a single oscillator can be extended to a collection of oscillators in a specified frequency band,

$$\Pi_{\text{diss}} = \omega \eta E, \quad (4.2)$$

where ω is the geometric mean center frequency of the band, and η is the mean energy loss factor of all the modes in the band.

SEA is closely related to room acoustics and thermodynamics. It is assumed that energy flows from oscillators of higher energy to those of lower energy. It was shown that the power flow is proportional to the average modal energy difference of two loosely coupled

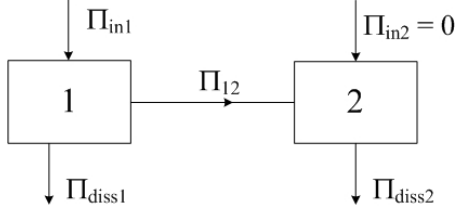


Figure 4.1: Block diagram for power flows between the structure and the reverberant field

and randomly excited oscillators [11] and can be expressed in power dissipation terms,

$$\langle \Pi_{12} \rangle = \eta_{12} n_1 \omega \{ \langle E_1 \rangle / n_1 - \langle E_2 \rangle / n_2 \}, \quad (4.3)$$

where n_1 and n_2 are the modal densities of the two groups of oscillators. n_{ij} is the coupling loss factor, describing the flow of energy from subsystem i to subsystem j , and $\langle E_j \rangle / n_j$ is the modal energy of group j .

Now consider a two-subsystem model with numerous modes in each subsystem where one subsystem is driven by external forces and the other subsystem is driven through the coupling. The typical application is the response of a structure excited in a reverberant field. The model is illustrated in Fig 4.1. The steady state power flow balance equations for the two groups of oscillators are,

$$\Pi_{\text{in}1} = \Pi_{\text{diss}1} + \Pi_{12}, \quad \Pi_{\text{in}1} = \omega \eta_1 E_1 + \omega \eta_{12} n_1 (E_1 / n_1 - E_2 / n_2), \quad (4.4)$$

$$\Pi_{\text{in}2} = \Pi_{\text{diss}2} - \Pi_{12}, \quad 0 = \omega \eta_2 E_2 - \omega \eta_{12} n_1 (E_1 / n_1 - E_2 / n_2), \quad (4.5)$$

where $\Pi_{\text{in}1}$ is the power input to subsystem 1, the structure; $\Pi_{\text{in}2} = 0$, is the power input to subsystem 2, the acoustic field. n_1 and n_2 are the modal densities. η_1 and η_2 are the internal loss factors. η_{12} and η_{21} are the coupling loss factors associated with energy flow from subsystem 1 to 2 and subsystem 2 to 1, respectively. E_1 and E_2 are the vibration energies associated with subsystems 1 and 2. All fluctuating terms are assumed to be both time- and space-averaged, and the brackets have been removed for convenience. Since the products of the modal density and coupling loss factor are equal in each pair of subsystems [15], $n_i\eta_{ij} = n_j\eta_{ji}$, the Eqs. (4.4) and (4.5) can be written in matrix form,

$$\omega \begin{bmatrix} n_1\eta_1 + n_1\eta_{12} & -n_1\eta_{12} \\ -n_2\eta_{21} & n_2\eta_2 + n_2\eta_{21} \end{bmatrix} \begin{Bmatrix} E_1/n_1 \\ E_2/n_2 \end{Bmatrix} = \begin{Bmatrix} \Pi_{\text{in}1} \\ 0 \end{Bmatrix}. \quad (4.6)$$

By rearranging the bottom equation of the matrix Eqs. (4.6), the steady state modal energy ratio between the two subsystems is,

$$\frac{E_2/n_2}{E_1/n_1} = \frac{\eta_{21}}{\eta_2 + \eta_{21}}. \quad (4.7)$$

The modal energy of subsystem 2 is always less than that of subsystem 1. If $\eta_2 \ll \eta_{21}$, the ratio approaches 1, which indicates that the additional damping provided to subsystem 2, the reverberant field, will be ineffective unless η_2 is about the same as η_{21} .

The two-subsystem model can be extended to a multiple-subsystem. In the general case, N groups of oscillators yield N simultaneous power flow balance equations which can

be written in matrix form. The steady state power flow balance matrix is,

$$\omega \mathbf{A} \begin{Bmatrix} E_1/n_1 \\ E_2/n_2 \\ \dots \\ E_N/n_N \end{Bmatrix} = \begin{Bmatrix} \Pi_{\text{in}1} \\ \Pi_{\text{in}2} \\ \dots \\ \Pi_{\text{in}N} \end{Bmatrix}, \quad (4.8)$$

$$\text{with } \mathbf{A} = \begin{bmatrix} (\eta_1 + \sum_{j \neq 1}^N \eta_{1j})n_1 & -\eta_{12}n_1 & \dots & -\eta_{1N}n_1 \\ -\eta_{21}n_2 & (\eta_2 + \sum_{j \neq 2}^N \eta_{2j})n_2 & \dots & -\eta_{2N}n_2 \\ \dots & \dots & \dots & \dots \\ -\eta_{N1}n_N & \dots & \dots & (\eta_N + \sum_{j \neq N}^N \eta_{Nj})n_N \end{bmatrix}.$$

4.3 Transmission suite model

A transmission suite is considered to consist of three coupled systems as illustrated in Fig. 4.2. The power flow balance equations for the three subsystems are written as,

$$\Pi_{\text{in}1} = \Pi_{\text{diss}1} + \Pi_{12} + \Pi_{13}, \quad \Pi_{\text{in}1} = \omega \begin{bmatrix} \eta_1 E_1 + \eta_{12}n_1(E_1/n_1 - E_2/n_2) \\ +\eta_{13}n_1(E_1/n_1 - E_3/n_3) \end{bmatrix}, \quad (4.9)$$

$$\Pi_{\text{in}2} = \Pi_{\text{diss}2} - \Pi_{12} + \Pi_{23}, \quad \Pi_{\text{in}2} = \omega \begin{bmatrix} \eta_2 E_2 - \eta_{12}n_1(E_1/n_1 - E_2/n_2) \\ +\eta_{23}n_2(E_2/n_2 - E_3/n_3) \end{bmatrix}, \quad (4.10)$$

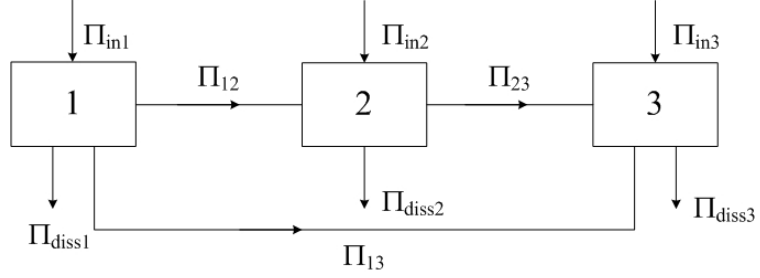


Figure 4.2: Block diagram for power flows between the structure and two reverberation rooms

$$\Pi_{\text{in}3} = \Pi_{\text{diss}3} - \Pi_{13} - \Pi_{23}, \quad \Pi_{\text{in}3} = \omega \begin{bmatrix} \eta_3 E_3 - \eta_{13} n_1 (E_1/n_1 - E_3/n_3) \\ -\eta_{23} n_2 (E_2/n_2 - E_3/n_3) \end{bmatrix}, \quad (4.11)$$

where Π_{13} is the power flow from subsystem 1 to subsystem 3 when there are no modes excited in subsystem 2 in the frequency band under consideration. The non-resonant power flow modes Π_{13} is due to modes which are resonant outside of the frequency band under consideration.

For transmission loss measurements, a panel is clamped between two reverberation rooms and excited by noise in the source room, $\Pi_{\text{in}2} = \Pi_{\text{in}3} = 0$, as shown in Fig. 4.3.

Equations (4.9) ~ (4.11) can be written in matrix form,

$$\omega \mathbf{A} \begin{Bmatrix} E_1/n_1 \\ E_2/n_2 \\ E_3/n_3 \end{Bmatrix} = \omega \begin{bmatrix} a_{11} & a_{12} & a_{13} \\ a_{21} & a_{22} & a_{23} \\ a_{31} & a_{32} & a_{33} \end{bmatrix} \begin{Bmatrix} E_1/n_1 \\ E_2/n_2 \\ E_3/n_3 \end{Bmatrix} = \begin{Bmatrix} \Pi_{\text{in}1} \\ 0 \\ 0 \end{Bmatrix}, \quad (4.12)$$

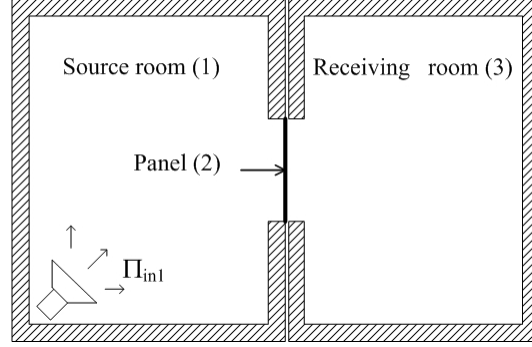


Figure 4.3: The transmission suite

$$\text{with } \mathbf{A} = \begin{bmatrix} (\eta_1 + \eta_{12} + \eta_{13})n_1 & -\eta_{12}n_1 & -\eta_{13}n_1 \\ -\eta_{21}n_2 & (\eta_2 + \eta_{21} + \eta_{23})n_2 & -\eta_{23}n_2 \\ -\eta_{13}n_1 & -\eta_{23}n_2 & \eta_3n_3 + \eta_{13}n_1 + \eta_{23}n_2 \end{bmatrix}.$$

Then, we have the modal energies,

$$\frac{E_1}{n_1} = \frac{F_{11}}{|A|} \Pi_{in1} = \frac{\begin{vmatrix} a_{22} & a_{23} \\ a_{32} & a_{33} \end{vmatrix}}{|A|} \Pi_{in1}, \quad \frac{E_3}{n_3} = \frac{F_{13}}{|A|} \Pi_{in1} = \frac{\begin{vmatrix} a_{21} & a_{22} \\ a_{31} & a_{32} \end{vmatrix}}{|A|} \Pi_{in1}, \quad (4.13)$$

where $|A|$ is the determinant of the matrix \mathbf{A} and F_{ij} is the cofactor of element a_{ij} .

Hence the modal energy ratio is,

$$\frac{E_1/n_1}{E_3/n_3} = \frac{a_{22}a_{33} - a_{23}a_{32}}{a_{21}a_{32} - a_{22}a_{31}} = 1 + \frac{2\eta_{\text{rad}}n_2\eta_3n_3 + (\eta_3n_3 + \eta_{\text{rad}}n_2)\eta_2n_2}{\eta_{\text{rad}}^2n_2^2 + \eta_{13}(2\eta_{\text{rad}} + \eta_2)n_1n_2}, \quad (4.14)$$

with $\eta_{21} = \eta_{23} = \eta_{\text{rad}}$.

The successful prediction of the modal energy ratio using SEA depends to a large extent on knowledge of the modal densities, internal loss factors and coupling loss factors associated with the subsystems.

4.4 Modal densities

The modal density of the volume of an acoustic space depends on whether the volume is one-dimensional, two-dimensional, or three-dimensional. The modal density of a volume, a three-dimensional enclosure, is,

$$n(f) = \frac{4\pi f^2 V}{c^3} + \frac{\pi f S}{2c^2} + \frac{P}{8c}, \quad (4.15)$$

where V is the volume of the enclosure, A is the total surface area, and P is the total length of the edges.

The modal density of structures depends on their boundary conditions and the governing equation of motion. For simply supported panels, the wave number for a freely propagating wave is,

$$k_{mn} = \sqrt{k_x^2 + k_y^2} = \sqrt{(m\pi/l_x)^2 + (n\pi/l_y)^2}, \quad (4.16)$$

where m and n are the mode numbers, l_x and l_y are the dimensions of the panel.

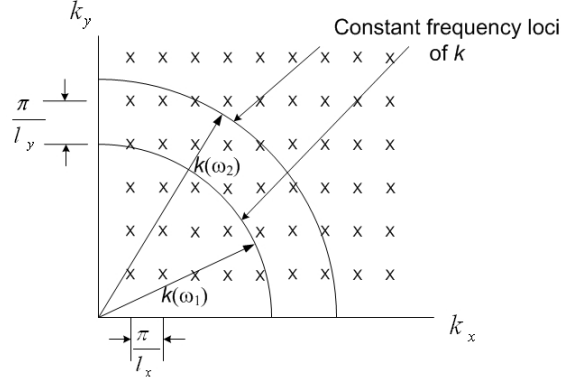


Figure 4.4: Constant frequency loci for transverse wave numbers of a simply supported panel

Then the modal density is associated with the constant frequency loci of the wave number, as illustrated in Fig. 4.4.

$$n(\omega) = \frac{\pi/4\Delta k^2}{(\pi/l_x)(\pi/l_y)\Delta\omega} = \frac{A_p dk^2}{4\pi d\omega}, \quad n(f) = 2\pi n(\omega) = \frac{A_p dk^2}{2 d\omega}. \quad (4.17)$$

The governing equation for free motion of a single-layer panel is,

$$D \frac{\partial^4 w}{\partial x^4} + m \frac{\partial^2 w}{\partial t^2} = 0, \quad \text{with } D = \frac{Et^3}{12(1-\nu^2)}, \quad m = \rho t, \quad (4.18)$$

where D is the bending rigidity, m is the surface density, E is the Young's modulus, and ν is the Poisson's ratio.

Then the wave number k must satisfy,

$$Dk^4 - m\omega^2 = 0 \quad \text{or} \quad k^2 = \omega \sqrt{m/D}. \quad (4.19)$$

Hence, for a simply supported single-layer panel, the modal density is constant, independent of frequency.

$$n(f) = \frac{A_p}{2} \sqrt{\frac{12(1 - \nu^2)\rho}{Et^2}}. \quad (4.20)$$

For boundary conditions other than simply supported, analytical expressions for the wave number of free motion are not available. High order modes of free motion are less sensitive to boundary conditions than low order modes. Thus, except for the first several modes, the modal density for simply supported panels provides an approximation for that of panels with other boundary conditions.

The modal densities of sandwich panels are more complicated because not only are they frequency dependent, but this frequency dependence is not a linear function. Clarkson and Ranky [22] derived the square wave number, k^2 , from the sixth-order equation given by Mead and Markus [23], by assuming the bending rigidity of the face sheets D_t is negligible,

$$k^2 \approx \frac{\mu\omega^2 + \omega\sqrt{(\mu\omega)^2 + 4\mu g^2 D_t(1 + Y)}}{2gD_t(1 + Y)}, \quad (4.21)$$

$$\text{with } Y = \frac{[h + (t_1 + t_3)/2]^2 E_1 t_1 E_3 t_3}{D_t(E_1 t_1 + E_3 t_3)}, \quad g = \frac{G_c}{h} \left(\frac{1}{E_1 t_1} + \frac{1}{E_3 t_3} \right), \quad D_t = \frac{E_1 t_1^3 + E_3 t_3^3}{12},$$

where E_j is the Young's modulus of the face sheet j and G_c is the shear modulus of the core; t_j and h are the thickness of the face sheet j and the core, respectively; and μ is the

surface density of the sandwich panel.

$$\text{Hence, } n(f) = \frac{\pi\mu A_p f}{gD_t(1+Y)} \left(1 + \frac{\mu\omega^2 + 2g^2 D_t(1+Y)}{\sqrt{(\mu\omega^2)^2 + 4\mu(g\omega)^2 D_t(1+Y)}} \right). \quad (4.22)$$

Ferguson and Clarkson [41] presented the modal density derived from the same sixth-order equation,

$$n(f) = \frac{A_p}{9} \left\{ P^{-2/3} \frac{dP}{d\omega} \cos\left(\frac{\theta}{3}\right) - P^{1/3} \frac{dP}{d\omega} \sin\left(\frac{\theta}{3}\right) \right\}, \text{ with} \quad (4.23)$$

$$P = 3\sqrt{3} \left\{ \frac{\mu\omega^2}{D_t} + g^2 \frac{(1+Y)^2}{2} \right\}^{3/2}, \quad \cos(\theta) = -\frac{27}{2P} \left[\frac{2}{27} g^3 (1+Y)^3 + \frac{\mu g \omega^2}{D_t} \left(\frac{1+Y}{3} - 1 \right) \right].$$

It was found that the modal density presented above produced a considerable difference from that derived by Clarkson and Ranky [22], as shown later in this section.

For sandwich panels with stiff cores, such as honeycomb cores, the anti-symmetric motion is dominant in the frequency range of interest. The governing equation for anti-symmetric motion of sandwich panels can be written as a cubic equation with respect to k^2 ,

$$k^6 + a_2 k^4 + a_1 k^2 + a_0 = 0. \quad (4.24)$$

The standard solutions are,

$$\{k^2\}_1 = -\frac{1}{3} a_2 + (S + T), \quad (4.25)$$

$$\{k^2\}_2 = -\frac{1}{3}a_2 - \frac{(S+T)}{2} + i\frac{\sqrt{3}}{2}(S-T), \quad (4.26)$$

$$\{k^2\}_3 = -\frac{1}{3}a_2 - \frac{(S+T)}{2} - i\frac{\sqrt{3}}{2}(S-T), \quad (4.27)$$

where

$$S = \sqrt[3]{R + \sqrt{D}}, \quad T = \sqrt[3]{R - \sqrt{D}}, \quad D = Q^3 + R^2,$$

$$Q = (3a_1 - a_2^2)/9, \quad R = (9a_2a_1 - 27a_0 - 2a_2^3)/54.$$

In the absence of damping, the wave number of free anti-symmetric transverse motion is always real. Then the freely propagating wave number must satisfy the equation,

$$k^2 = -(a_2/3) + (S+T). \quad (4.28)$$

Hence the modal density can be obtained from,

$$\frac{dk^2}{d\omega} = \left[-\frac{1}{3} \frac{da_2}{d\omega} + \left(\frac{dS}{d\omega} + \frac{dT}{d\omega} \right) \right], \quad (4.29)$$

with

$$\frac{dS}{d\omega} = \frac{1}{3}S^{-2} \left(\frac{dR}{d\omega} + \frac{1}{2\sqrt{D}} \frac{dD}{d\omega} \right), \quad \frac{dT}{d\omega} = \frac{1}{3}T^{-2} \left(\frac{dR}{d\omega} - \frac{1}{2\sqrt{D}} \frac{dD}{d\omega} \right),$$

$$\frac{dD}{d\omega} = 3Q^2 \frac{dQ}{d\omega} + 2R \frac{dR}{d\omega}, \quad \frac{dR}{d\omega} = \frac{a_1}{6} \frac{da_2}{d\omega} + \frac{a_2}{6} \frac{da_1}{d\omega} - \frac{1}{2} \frac{da_0}{d\omega} - \frac{a_2^2}{9} \frac{da_2}{d\omega},$$

$$\frac{dQ}{d\omega} = \frac{1}{3} \frac{da_1}{d\omega} - \frac{2a_2}{9} \frac{da_2}{d\omega}.$$

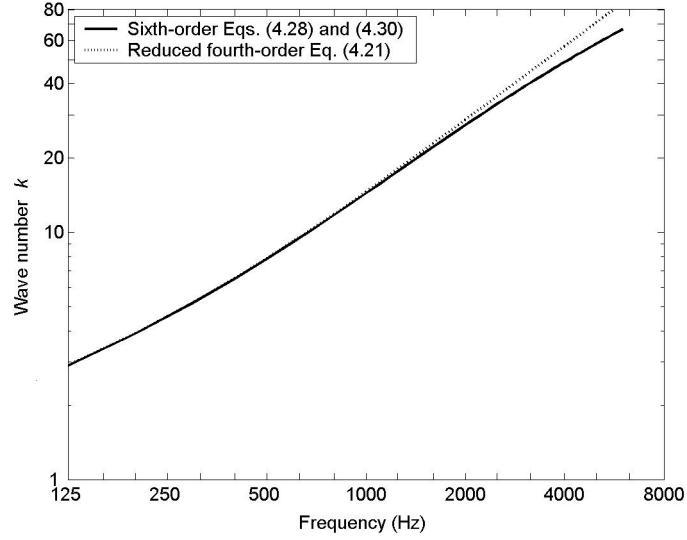


Figure 4.5: Wave numbers for free transverse wave in x -axis of panel A

Equation (4.24) is equivalent to the sixth-order governing equation for free motion of sandwich panels presented by Mead and Markus [23], if

$$a_2 = g(1 + Y), \quad a_1 = -\mu\omega^2/D_t, \quad a_0 = -\mu g\omega^2/D_t. \quad (4.30)$$

The wave numbers and modal densities of sandwich panel A , were computed, shown in Figs. 4.5 and 4.6. The properties of panel A are given in Table 3.1, and the dimensions are $1.22 \text{ m} \times 2.44 \text{ m}$. It is shown that the effect of bending rigidity of the face sheets, D_t , on wave numbers is noticeable above 2000 Hz. While the effect of bending rigidity of the face sheets on modal densities is apparent above 2000 Hz. The modal density presented by Ferguson and Clarkson, Eq. (4.23), generates quite different data from the data obtained

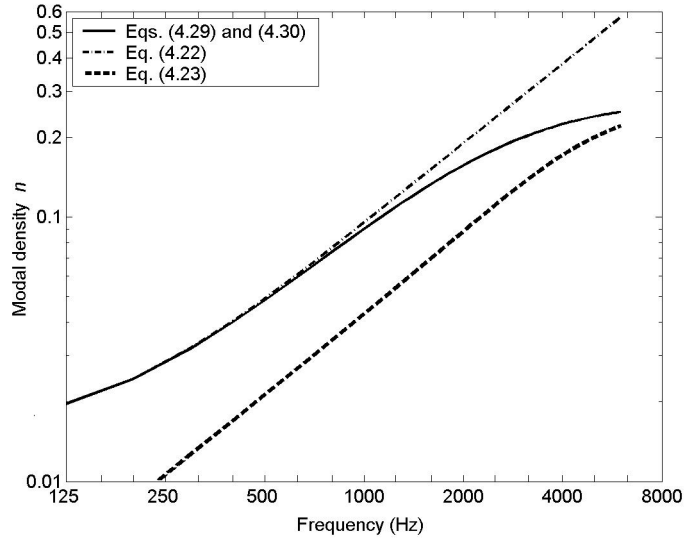


Figure 4.6: Modal densities of free transverse wave in x -axis of panel A

from the other two equations. Some factors might be missing. Two other sixth-order anti-symmetric equations, Nilsson and Nilsson's, Eq. (3.67) and the one developed in previous chapter, Eq. (3.60), also were employed to compute the wave numbers and the modal densities. It was found that the results from these two more complicated equations are the same as those from the sixth-order equation given by Mead and Markus, Eq. (4.30).

4.5 Internal loss factors

Internal loss factors of the volumes of acoustic spaces can be obtained from the reverberation time T_{60} , the reverberation time being the time that the energy level in the volume takes to decay to 10^{-6} of its original value. The internal loss factor of an acoustic volume

is given by,

$$\exp(-\eta\omega T_{60}) = 10^{-6}. \quad (4.31)$$

Hence,

$$\eta = \frac{2.2}{fT_{60}}. \quad (4.32)$$

Analytical expressions are not generally available for internal loss factors of structural components. Very little consistent information is readily available about the internal loss factors of structural elements. The internal loss factor often varies from mode to mode, and it is widely recognized that it is the major source of uncertainty in the estimation of the dynamic response of a system.

4.6 Coupling loss factors

The coupling loss factors for the SEA transmission suite model have two classes of factor, the structure-acoustic volume coupling loss factor and the acoustic-acoustic volume coupling loss factor. The structure-acoustic volume coupling loss factor can be associated with the radiation resistance of the structure.

The power radiated by a structure is given by,

$$\Pi = R_{\text{rad}}\langle v_p^2 \rangle. \quad (4.33)$$

The power dissipated due to radiation is,

$$\Pi = \eta_{\text{rad}} \omega M_p \langle v_p^2 \rangle. \quad (4.34)$$

Hence, the coupling loss factor due to radiation damping is,

$$\eta_{\text{rad}} = \frac{R_{\text{rad}}}{\omega M_p}. \quad (4.35)$$

When a structure is excited in a reverberant acoustic field, the radiation resistance can be expressed as [11, 13],

$$R_{\text{rad}} = (16/\pi) \rho c k^2 \int \int d\vec{r}_1 d\vec{r}_2 \Psi(\vec{r}_1, \vec{r}_2) \Phi(\vec{r}_1, \vec{r}_2), \quad (4.36)$$

where k is the wave number in the air; Ψ is the cross correlation of the vibrational field and Φ is the cross correlation of the pressure field; and ρ and c are the mass density and the speed of sound in air, respectively.

For free transverse waves on an infinite structure, yields

$$\frac{R_{\text{rad}}}{A_p} = \begin{cases} 0, & k_p > k \\ \rho c (1 - k_p^2/k^2)^{-1/2}, & k_p < k \end{cases}, \quad (4.37)$$

where k_p is the wave number in the structure and A_p is the area of the panel.

The equation above shows that a free wave on an infinite structure will not radiate sound if its wavelength is smaller than the acoustic wavelength.

Consider the single mode radiation resistance of a finite baffled simply supported single-layer panel. The cross correlation of the vibrational field is given by,

$$\Psi(\vec{r}_1, \vec{r}_2) = \begin{cases} \prod_{i=1}^2 [\sin(x_i k_{px}) \sin(y_i k_{py})], & 0 < x_i < l_x \text{ and } 0 < y_i < l_y \\ 0, & 0 > x_i > l_x \text{ and } 0 > y_i > l_y \end{cases}, \quad (4.38)$$

where the wave number in the panel is, $k_p = \sqrt{k_{px}^2 + k_{py}^2}$. The cross correlation of the pressure field is given by,

$$\Phi(\vec{r}_1, \vec{r}_2) = \frac{\sin k|\vec{r}_1 - \vec{r}_2|}{k|\vec{r}_1 - \vec{r}_2|}. \quad (4.39)$$

Then the radiation resistance can be written as,

$$R_{\text{rad}} = (64\rho c k^2 / \pi^2) \int_0^1 I_x I_y d\beta, \quad \text{with} \quad (4.40)$$

$$I_x = \left(\frac{k_{px}^2}{k^4} \right) \frac{\begin{pmatrix} \cos^2 \\ \sin^2 \end{pmatrix}}{[\beta^2 - (k_{px}^2/k^2)]^2} \frac{k l_x \beta}{2}, \quad I_y = \left(\frac{k_{py}^2}{k^4} \right) \int_0^{\pi/2} \frac{\begin{pmatrix} \cos^2 \\ \sin^2 \end{pmatrix}}{[(k_{py}^2/k^2) - (\alpha \sin \theta)^2]^2} \frac{k l_y \alpha}{2} \sin \theta d\theta,$$

$$\alpha = \sqrt{f/f_c}, \quad \beta = \sqrt{1 - \alpha^2},$$

where f_c is the critical frequency of the single-layer panel. The \cos^2 and \sin^2 are to be chosen according to whether the mode, either in x or y direction, is odd or even, respectively.

The resonant modes of a panel can be divided into three classes. Modes which have wave phase speeds in both edge directions less than the speed of sound are termed “corner” modes. Modes having wave phase speeds in one edge direction greater than the speed of sound and wave phase speeds in the other edge direction less than the speed of sound are termed “edge” modes. Modes having wave phase speeds greater than the speed of sound in air are termed “surface” modes.

The approximated radiation resistance of the modes is,

$k_p < k$, **above coincidence, surface mode**

$$R_{\text{rad}} = \frac{A_p \rho c}{\sqrt{1 - (k_p/k)^2}}; \quad (4.41)$$

$k_p = k$, **at coincidence,**

$$R_{\text{rad}} = \frac{A_p \rho c}{3\sqrt{\pi}} \left[\sqrt{\frac{l_x k_p^2}{k_{px}}} + \sqrt{\frac{l_y k_p^2}{k_{py}}} \right];$$

$k_p > k$, $k_{py} > k$, $k_{px} < k$, **below coincidence, x -edge mode,**

$$R_{\text{rad}}^x = \left[\frac{A_p \rho c k}{k_{py}^2 l_y} \right] \left\{ \frac{1 + (k_p^2 - k^2)/k_{py}^2}{[(k_p^2 - k^2)/k_{py}^2]^{3/2}} \right\};$$

$k_p > k$, $k_{py} < k$, $k_{px} > k$, **below coincidence, y -edge mode,**

$$R_{\text{rad}}^y = \left[\frac{A_p \rho c k}{k_{px}^2 l_x} \right] \left\{ \frac{1 + (k_p^2 - k^2)/k_{px}^2}{[(k_p^2 - k^2)/k_{px}^2]^{3/2}} \right\};$$

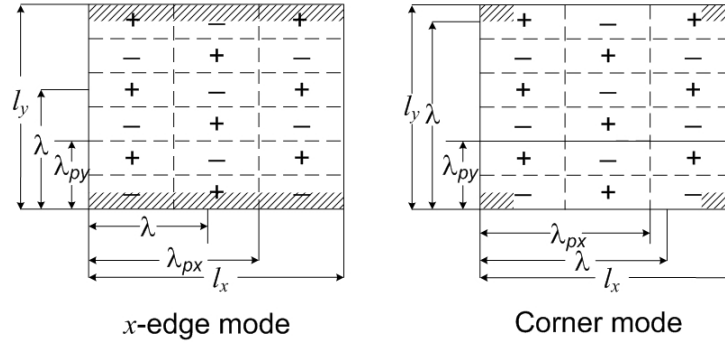


Figure 4.7: Effective radiation areas for edge and corner modes

$k_{py} > k$, $k_{px} > k$, **corner mode**,

$$R_{\text{rad}} = \frac{8\rho ck^2}{\pi k_{px}^2 k_{py}^2}.$$

It is shown theoretically that surface modes have high radiation efficiencies. Corner modes have lower radiation efficiencies than edge modes. The theoretical results for the radiation and classification of modes can also be given a simple physical explanation. Figure 4.7 shows a typical modal pattern in a baffled simply-supported panel. The dotted lines represent panel nodes. For corner modes, the fluid will produce pressure waves which will travel faster in the fluid than the panel transverse waves and the acoustic pressures created by the quarter wave cells will be cancelled everywhere except at the corners as shown. For edge modes, cancellation can only occur in one edge direction and the quarter wave cells shown will cancel everywhere except at x -edges. For surface modes, the fluid cannot produce

pressure waves which will move fast enough to cause any cancellation. The modes radiate from the whole surface area of a panel.

The results for the single mode can be extended to the reverberant vibrational field radiation resistance. The modal averaged radiation resistance of a baffled simply supported single-layer panel in an acoustic reverberant field given by [13] is, as corrected in Ref. [18],

$$R_{\text{rad}}^{2\pi} = A_p \rho c \begin{cases} \sigma_{\text{corner}} + \sigma_{\text{edge}}, & f < f_c \\ \sqrt{l_x/\lambda_c} + \sqrt{l_y/\lambda_c}, & f = f_c \\ [1 - (f_c/f)]^{-1/2}, & f > f_c \end{cases} \quad \text{with} \quad (4.42)$$

$$\sigma_{\text{corner}} = \begin{cases} (\lambda_c \lambda_a / A_p) \alpha^2 (8/\pi^4) [(1 - 2\alpha^2)/\alpha / \sqrt{1 - \alpha^2}], & f < f_c/2 \\ 0, & f > f_c/2 \end{cases},$$

$$\sigma_{\text{edge}} = \frac{1}{4\pi^2} \frac{P\lambda_c}{A_p} \frac{(1 - \alpha^2) \ln [(1 + \alpha)/(1 - \alpha)] + 2\alpha}{(1 - \alpha^2)^{3/2}},$$

$$\lambda_a = \frac{c}{f}, \quad \lambda_c = \frac{c}{f_c}, \quad \alpha = \sqrt{\frac{f}{f_c}}.$$

Maidanik [13] also noted that well below the critical frequency, the radiation resistance of a clamped panel is twice that of a simply supported panel. Later Nikiforov [44] and Berry *et al.* [24] showed that this conclusion is restricted to large structures or high order modes.

Typical frequency-averaged radiation resistances of baffled simply supported single-layer panels are illustrated in Fig. 4.8. The radiation resistances of two different dimensions of aluminum panels, 1.22 m × 2.44 m and 0.42 m × 0.84 m, were calculated. The thicknesses

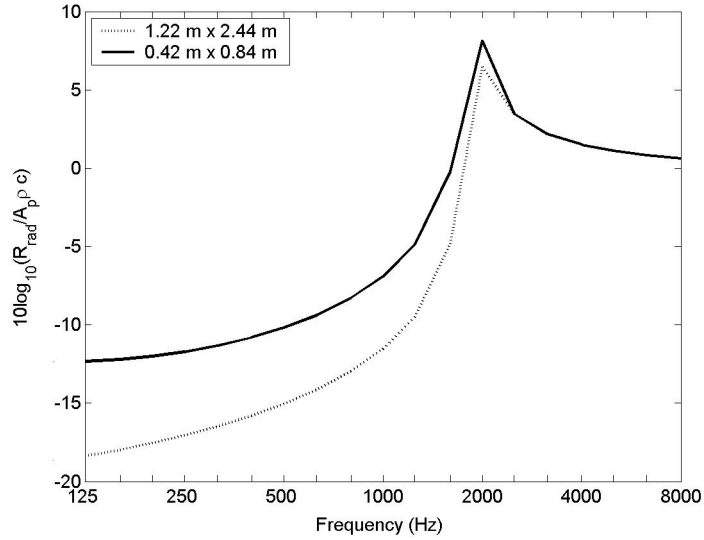


Figure 4.8: Normalized radiation resistances of baffled simple supported aluminum panels

of both panels are 6.35 mm. It is shown that the small panel has higher values of radiation efficiency than the large panel below the critical frequency. This is because more effective radiation areas per unit area exist in the small panel.

The acoustic-acoustic volume coupling loss factors describe the power flow between two reverberation rooms when there are no modes excited in the structure in the frequency band of interest.

During steady state conditions, the sound power flowing from the source room to the receiving room due to sound transmission is,

$$\Pi_{\text{tr}} = \tau I_p A_p, \text{ with } I_p = \frac{\langle p^2 \rangle}{4\rho c}, \quad (4.43)$$

where I_p is the incident sound intensity on the structure in the source room and τ is the transmission coefficient of the structure. The power flow can be written in dissipation terms,

$$\Pi_{\text{tr}} = \eta_{\text{tr}} \omega E = \eta_{\text{tr}} \omega \frac{\langle p^2 \rangle}{\rho c^2} V. \quad (4.44)$$

Hence, the source-receiving coupling loss factor is associated with the non-resonant transmission coefficient, τ_{nr} ,

$$\eta_{13} = \eta_{\text{nr}} = \frac{c A_p}{4 V_1 \omega} \tau_{\text{nr}}, \quad (4.45)$$

where V_1 is the volume of the source room.

Since mass law transmission is derived by assuming zero stiffness and damping in the infinite structure and off resonance, then η_{13} can be obtained from the field incidence mass law transmission coefficient,

$$10 \log_{10} \left(\frac{1}{\tau_{\text{nr}}} \right) = 20 \log_{10} \left(\frac{\omega \mu}{2 \rho c} \right) - 5 \text{ dB}, \quad (4.46)$$

where μ is the surface mass density of the structure.

Sewell [20] derived the transmission coefficient due to forced vibration,

$$10 \log_{10} \left(\frac{1}{\tau_{\text{nr}}} \right) \approx 20 \log_{10} \left[\frac{\omega \mu}{2 \rho c} \left(1 - \frac{\omega^2}{\omega_c^2} \right) \right] - 10 \log_{10} \left[\ln(k \sqrt{A_p}) + \frac{1}{4 \pi k^2 A_p} \right] - 5 \text{ dB}, \quad (4.47)$$

where ω_c is the critical frequency of the structure. This formula is not for lightweight panels, and it requires, $\mu > 10 \text{ kg/m}^2$.

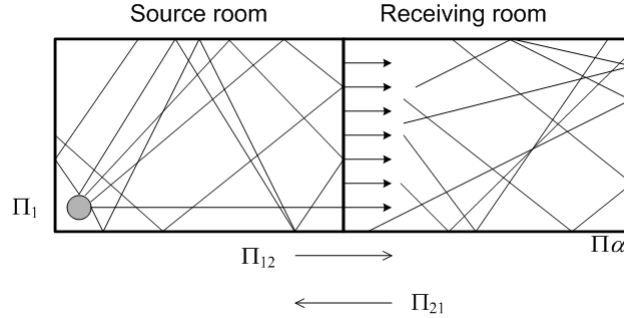


Figure 4.9: Sound transmission measurements from the two-room method

4.7 Sound transmission loss

The sound transmission loss of partition can be obtained experimentally by the two-room method. The sound power Π_{12} flowing from the source room to the receiving room must equal the sound power Π_{21} flowing back into the source room from the receiving room plus the sound power Π_α , which is absorbed within the receiving room, as illustrated in Fig. 4.9.

$$\Pi_{12} = \Pi_{21} + \Pi_\alpha. \quad (4.48)$$

The sound power, Π_1 , incident upon the surface of the partition is,

$$\Pi_1 = \frac{\langle p_1^2 \rangle}{4\rho c} A_p, \quad (4.49)$$

where A_p is the surface area of the partition between two rooms, and $\langle p_1^2 \rangle$ is the mean square sound pressure in the source room. Likewise, the sound power incident upon the

receiving room side of the partition is,

$$\Pi_2 = \frac{\langle p_2^2 \rangle}{4\rho c} A_p, \quad (4.50)$$

where $\langle p_2^2 \rangle$ is the mean square sound pressure in the receiving room. The sound power which is transmitted from the source room to the receiving room and the sound power transmitted from the receiving room back to the source room are,

$$\Pi_{12} = \Pi_1 \tau, \quad \Pi_{21} = \Pi_2 \tau, \quad (4.51)$$

where τ is the transmission coefficient of the partition. The sound power absorbed by the receiving room is,

$$\Pi_\alpha = \frac{\langle p_2^2 \rangle}{4\rho c} A_p S_2 \alpha_2, \quad (4.52)$$

where S_2 is the total surface area of the receiving room and α_2 is the average absorption coefficient in the receiving room.

Substituting Eqs. (4.52) and (4.51) into Eq. (4.48), yields

$$\frac{1}{\tau} = \frac{A_p}{S_2 \alpha_2} \left(\frac{\langle p_1^2 \rangle}{\langle p_2^2 \rangle} - 1 \right) = \frac{\langle p_1^2 \rangle}{\langle p_2^2 \rangle} \frac{A_p}{S_2 \alpha_2 + \tau A_p}. \quad (4.53)$$

The energy density ratio of the transmission suite SEA model can be evaluated by Eq. (4.14). Since the mean square sound pressure ratio is equivalent to the sound energy density

ratio between the two reverberation rooms,

$$\frac{E_1/V_1}{E_3/V_3} = \frac{\langle p_1^2 \rangle}{\langle p_2^2 \rangle}. \quad (4.54)$$

The transmission loss of the structure in a transmission suite SEA model can be estimated from,

$$\text{TL} = 10 \log_{10} \left(\frac{1}{\tau} \right) = 10 \log_{10} \left[\frac{A_p}{S_3 \alpha_3} \left(\frac{E_1/V_1}{E_3/V_3} - 1 \right) \right], \quad (4.55)$$

where S_3 is the total surface area of the receiving room. α_3 is the average absorption coefficient in the receiving room. $S_3 \alpha_3$ is associated with the reverberation time of the receiving room T_3 , which is related to the internal loss factor of the receiving room, η_3 .

The modal density of large acoustic volumes is generally approximated by the first term of Eq. (4.15). Hence, the transmission loss can be expressed as,

$$\text{TL} = 10 \log_{10} \left[\frac{A_p T_3}{0161 V_3} \left(\frac{E_1/V_1}{E_3/V_3} - 1 \right) \right] = 10 \log_{10} \left[4\pi \frac{13.7 f A_p}{n_3 \eta_3 c^3} \left(\frac{E_1/V_1}{E_3/V_3} - 1 \right) \right], \quad (4.56)$$

$$\text{with,} \quad \frac{E_1/n_1}{E_3/n_3} - 1 = \frac{2\eta_{\text{rad}} n_2 \eta_3 n_3 + (\eta_3 n_3 + \eta_{\text{rad}} n_2) \eta_2 n_2}{\eta_{\text{rad}}^2 n_2 n_3 + \eta_{13} (2\eta_{\text{rad}} + \eta_2) n_1 n_2}.$$

The transmission coefficient due to non-resonant modes is,

$$\frac{1}{\tau} = \frac{4\pi f}{c^3} \frac{13.7 A_p}{\eta_{13} n_1} = \frac{1}{\tau_{\text{nr}}}, \quad \text{with } \eta_{\text{rad}} = 0. \quad (4.57)$$

The transmission coefficient due to resonant modes is,

$$\frac{1}{\tau} = 4\pi \frac{13.7fA_p}{c^3} \frac{2\eta_{\text{rad}} + [1 + (\eta_{\text{rad}}n_2)/(n_3\eta_3)]\eta_2}{\eta_{\text{rad}}^2 n_2}, \text{ with } \eta_{13} = 0. \quad (4.58)$$

In the absence of structural damping, the transmission coefficient becomes,

$$\frac{1}{\tau} = 4\pi \frac{13.7fA_p}{c^3} \frac{2}{\eta_{\text{rad}}n_2 + 2\eta_{13}n_1}. \quad (4.59)$$

4.8 Numerical results

Since most transmission loss measurements are conducted in reverberation rooms, the reverberation times were assumed in this numerical study instead of the internal loss factors of the two rooms. The reverberation times of two rooms were assumed to be 1.4 seconds at all frequencies.

Two non-resonant transmission coefficients, Eqs. (4.46) and (4.47), were used in calculating the sound transmission loss of an aluminum panel, panel *D*, as shown in Fig. 4.10. The estimates were compared with the measured values in Ref. [18]. The material properties of the aluminum panels were assumed as, Young's modulus $E = 70$ GPa, Poisson's ratio $\nu = 0.3$, mass density $\rho = 2700$ kg/m³, energy loss factor $\eta_{\text{int}} = 0.001$. The thickness and the dimensions are given in Table 4.1. The volumes of the two reverberation rooms were, 127.4 m³ [18]. The estimates using the field incidence mass law as the non-resonant

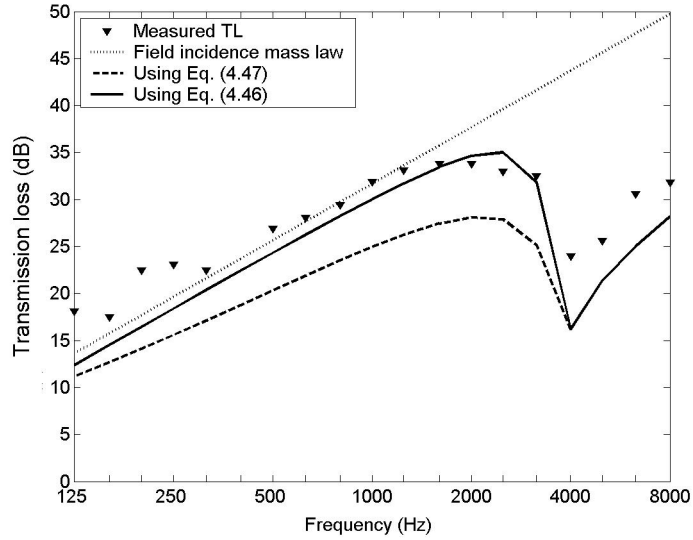


Figure 4.10: Estimated transmission loss values of panel *D*

Table 4.1: Properties of aluminum panels *D*, *E* and *F*

Property	Panel <i>D</i>	Panel <i>E</i>	Panel <i>F</i>
Thickness (mm)	3.175	6.35	6.35
Dimension (m×m)	1.97×1.55	1.22×2.44	0.42×0.84

transmission coefficient are much closer to the measured values than those using Sewell's formula, Eq. (4.47), below the critical frequency.

The sound transmission loss values due to resonant and non-resonant modes were also computed, as shown in Fig. 4.11. The non-resonant coupling loss factors were obtained from field incidence mass law, Eq. (4.46). Below the critical frequency, non-resonant modes are dominant in transmission, and above that frequency, resonant modes are substantial.

Two sets of modal densities were employed in the calculation of sound transmission loss for honeycomb sandwich panel *A*. The predictions of sound transmission loss are shown

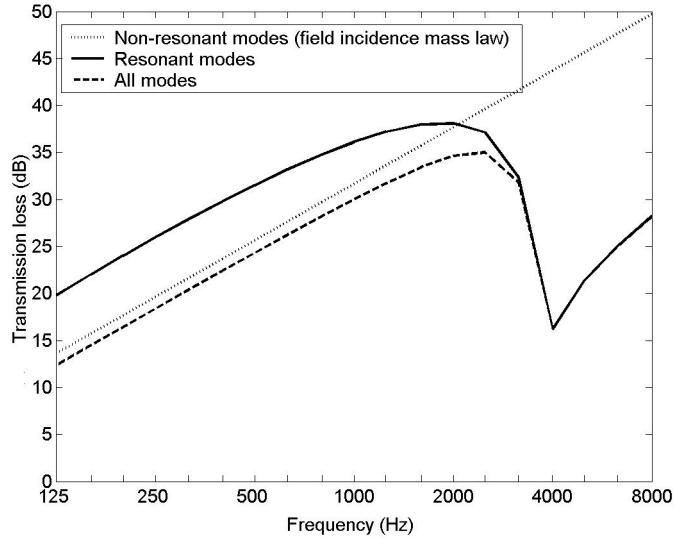


Figure 4.11: Resonant and non-resonant modes on the sound transmission loss of panel D

and compared with the measured values [6]. The properties of panel A are given in Table 3.1. The internal loss factor was assumed to be $\eta_{\text{int}} = 0.03$. The volumes of the two rooms were taken as 100 m^3 .

The theoretical radiation resistances for sandwich panels are not readily available. From the previous chapter, the critical frequency of panel A is near to 200 Hz, and the radiation resistance is independent of the wave number for structures above the critical frequency, then the radiation resistances of sandwich panels are only associated with the critical frequencies above that frequency. The predictions using SEA were computed from 250 Hz, above the critical frequency. Both predictions using SEA produced similar values of sound transmission loss, the difference between them is noticeable above 2000 Hz, as shown in Fig. 4.12. Since the approximate modal density function overestimates modal densities

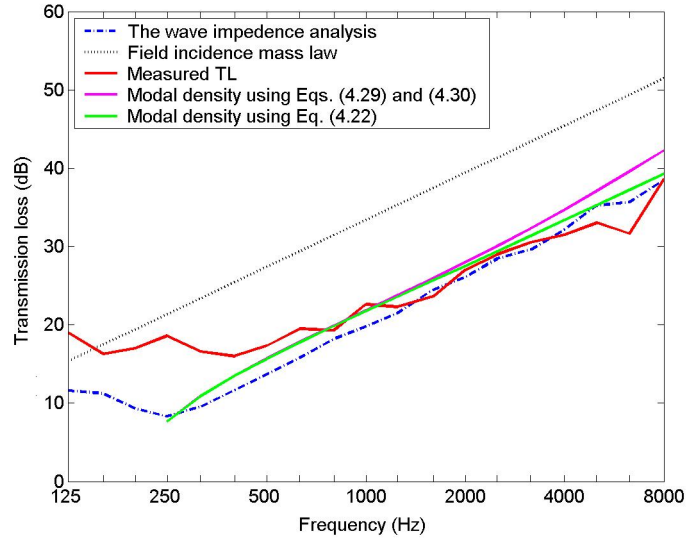


Figure 4.12: Estimated sound transmission loss values of panel *A*

at high frequencies, as shown in Fig. 4.6, the estimated sound transmission loss values are smaller than those using the modal densities derived from the sixth-order governing equation.

The effects of dimensions of panels and volumes of rooms on sound transmission loss were studied, as illustrated in Fig. 4.13. The volumes of the large rooms were 127.4 m^3 , and 52 m^3 for the small rooms. Both panels are made of aluminum, and have the same material properties as those of panel *D*. The thicknesses and the dimensions are given in Table 4.1. Two panels with the identical thickness, then yields the same surface mass density and critical frequency. The sound transmission loss predictions from SEA are insensitive to the size of the panels and the volumes of the rooms above the critical frequency. The sound

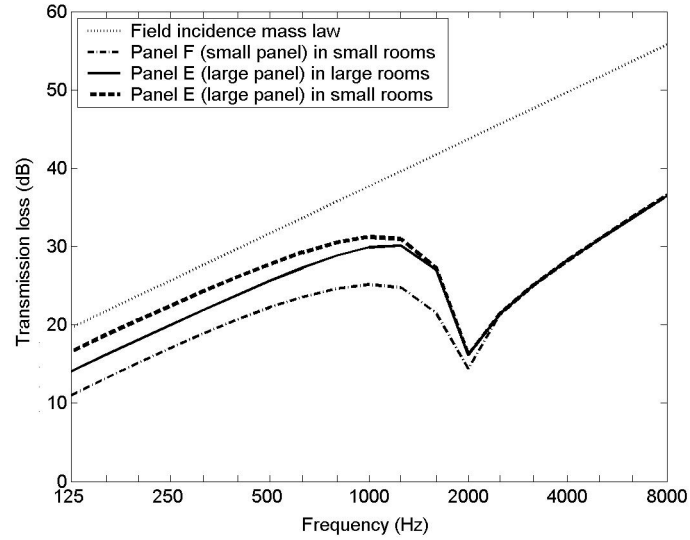


Figure 4.13: The effects of dimensions of panels and volumes of rooms on sound transmission loss

transmission loss predictions for the panels reduces with decreasing the size of the panels or increasing the volumes of the rooms below the critical frequency.

4.9 Conclusions

It is shown that for lightweight panels, the SEA model using non-resonant coupling loss factor associated with the field incidence mass law generates better results than the model using Sewell's formula. For sandwich panels with stiff cores, anti-symmetric motions dominant in the frequency range of interest, SEA produces reliable sound transmission loss estimates above the critical frequency. The derived modal density of a traditional honeycomb sandwich panel was found to be one half of the approximate modal density

that was obtained from a fourth-order governing equation, which yields a 2 dB difference in the sound transmission loss. SEA produces similar sound transmission loss estimates for single-layer panels made of the identical material and with the same thickness above the critical frequency. Below that critical frequency, the estimates depend on the dimension of the panels and the volumes of the rooms.

CHAPTER 5

BOUNDARY ELEMENT ANALYSIS

5.1 Introduction

For a baffled planar structure, boundary element analysis has the advantage over finite element analysis of avoiding the discretization of the fluid domain. Thus it is efficient for solving exterior interactions, where the fluid occupies an unbounded domain. Three-domain, fluid-structure-fluid systems have been modeled as coupled systems [32, 34, 46] and uncoupled systems [33, 35, 45]. The uncoupled approach assumes that the structure is rigid, and that the external load of the structure is only associated with the sound pressure in the incident and reflected waves at the interface. The coupled approach considers the effect of the sound pressure in the radiated waves at the interfaces.

In this chapter, finite element models of sandwich structures are reviewed and some simulation results from MSC Nastran are compared with the exact solutions from the classic analysis. The concepts of boundary element analysis are introduced. The coupled boundary element analysis model for fluid-structure-fluid systems is discussed. A computer program in MATLAB language is developed to compute the sound transmission loss of a baffled simply supported aluminum panel. The estimates of sound transmission loss for the aluminum panel from a sound transmission loss model in a commercial boundary element analysis software, LMS SYSNOISE, are provided and compared with the results from the computer

program. Finally, a coupled boundary element analysis model for the sound transmission loss of three-layer symmetric sandwich panels is presented.

5.2 Finite element analysis models for sandwich structures

The displacement compatibility over the entire interfaces between the core and the face sheets is required for modeling of sandwich structures. Some authors have developed finite element programs for sandwich beams [35, 49], while others presented modeling methods using commercially available finite element analysis softwares [48]. Finite element programs for sandwich beams follow the same procedure for the development of the governing equation for transverse motion of three-layer sandwich panels described in Sec. 3.2. The face sheets are treated as elementary bent plates. The mid-plane displacements of the face sheets and the displacements of the core are assumed to satisfy the displacement compatibility over the face sheet-core interfaces.

Earlier finite element methods implemented with MSC Nastran required four layers of nodes and extensive constraint equations to achieve the proper bending-shearing behavior of a three-layer sandwich structure [47]. Johnson and Kienholz [48] proposed a finite element model for sandwich structures with viscoelastic cores using only two layers of nodes, as illustrated in Fig 5.1. The face sheets are modeled with plate elements, such as CQUAD and CTRIA, with two rotational and three translational degrees of freedom per node. The viscoelastic core is modeled with solid elements, such as HEXA and PENTA, with three translational degrees of freedom per node. The plate elements are offset to one surface of

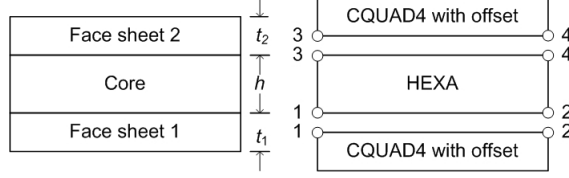


Figure 5.1: Finite element model for sandwich structures using MSC Nastran

the plate, coincident with the nodes of the adjoining solid elements. The plate elements are able to account for the stretching and bending of the face sheets. The modal loss factor is defined as,

$$\eta^{(r)} = \eta_v [V_v^{(r)} / V^{(r)}], \quad (5.1)$$

where η_v is the energy loss factor of the viscoelastic core evaluated at the r th calculated resonance frequency and $V_v^{(r)} / V^{(r)}$ is the fraction of elastic strain energy attributable to the core when the structure deforms in the r th mode shape.

The sixth-order differential equation of motion formulated in terms of the transverse displacement w , for a three-layer sandwich beam with a viscoelastic core is [23],

$$\frac{\partial^6 w}{\partial x^6} - g(1 + Y) \frac{\partial^4 w}{\partial x^4} + \frac{\mu}{D_t} \left(\frac{\partial^4 w}{\partial x^2 \partial t^2} - g \frac{\partial^2 w}{\partial t^2} \right) = \frac{1}{D_t} \left(\frac{\partial^2 q}{\partial x^2} - gq \right), \quad (5.2)$$

$$\text{with } D_t = \frac{E_1 t_1^3 + E_3 t_3^3}{12}, \quad g = \frac{G_c}{h} \left(\frac{1}{E_1 t_1} + \frac{1}{E_3 t_3} \right), \quad Y = \frac{[h + (t_1 + t_3)/2]^2 E_1 t_1 E_3 t_3}{D_t (E_1 t_1 + E_3 t_3)},$$

Table 5.1: Classic boundary conditions

Clamped	$w = 0$	$\nabla w = 0$	$\nabla^5 w - gY\nabla^3 w = 0$
Free	$\nabla^2 w = 0$	$\nabla^4 w - (\mu/D_t)\omega^2 w = 0$	$\nabla^5 w - g(1+Y)\nabla^3 w - (\mu/D_t)\omega^2 \nabla w = 0$

where G_c is the shear modulus of the core, q is the external load, and μ is the surface mass density.

The exact solution of Eq. (5.2), is of the form,

$$w = (A_1 e^{-ik_1 x} + A_2 e^{-ik_2 x} + A_3 e^{-ik_3 x} + A_4 e^{-ik_4 x} + A_5 e^{-ik_5 x} + A_6 e^{-ik_6 x}) e^{i\omega t}. \quad (5.3)$$

The amplitude A_j can be determined from the boundary conditions [23, 50], given in Table 5.1.

For a cantilever sandwich beam, as shown in Fig. 5.2, the equations for amplitudes A_j of free transverse motion can be written in matrix form as,

$$\begin{bmatrix} b_{11} & b_{12} & b_{13} & b_{14} & b_{15} & b_{16} \\ b_{21} & b_{22} & b_{23} & b_{24} & b_{25} & b_{26} \\ b_{31} & b_{32} & b_{33} & b_{34} & b_{35} & b_{36} \\ b_{41} & b_{42} & b_{43} & b_{44} & b_{45} & b_{46} \\ b_{51} & b_{52} & b_{53} & b_{54} & b_{55} & b_{56} \\ b_{61} & b_{62} & b_{63} & b_{64} & b_{65} & b_{66} \end{bmatrix} \begin{Bmatrix} A_1 \\ A_2 \\ A_3 \\ A_4 \\ A_5 \\ A_6 \end{Bmatrix} = \begin{Bmatrix} 0 \\ 0 \\ 0 \\ 0 \\ 0 \\ 0 \end{Bmatrix}, \quad (5.4)$$

with, $b_{1j} = 1$, $b_{2j} = -ik_j$, $b_{3j} = -i(k_j^5 + gYk_j^3)$, $b_{4j} = -k_j^2 e^{-ik_j L}$,

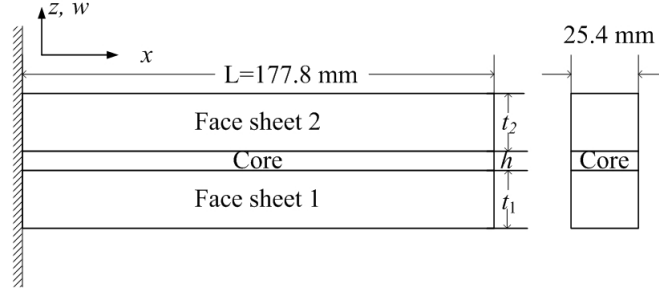


Figure 5.2: A cantilever sandwich beam with viscoelastic core (beam G)

$$b_{5j} = \left(k_j^4 - \frac{\mu}{D_t} \omega^2 \right) e^{-ik_j L}, \quad b_{6j} = \left[-ik_j^5 - ik_j^3 g(1 + Y) + ik_j \frac{\mu}{D_t} \omega^2 \right] e^{-ik_j L}.$$

The modal loss factor η is determined by the perturbation method [51],

$$\eta = \frac{\text{Im}(\omega^2)}{\text{Re}(\omega^2)}, \quad \text{where } \omega^2 = \frac{D_t k^6 + g(1 + Y)k^4}{\mu k^2 + g}. \quad (5.5)$$

The cantilever beam, beam G , has identical aluminum face sheets and a viscoelastic core, the properties are given in Table 5.2. The results for beam G , as obtained from the sixth-order equation and two finite element models using MSC Nastran, are presented in Table 5.3. One finite element model had CQUAD4 elements offset from the solid nodes by a half of the thickness of the face sheets, as shown in Fig. 5.1, and the other was without reference to the surface offset. Both finite element models had 50 CQUAD4 plate elements and 50 HEXA solid elements in the lengthwise direction, x -axis.

Table 5.2: Properties of beam G

Property	Face sheet	Core
Young's modulus (Pa)	69×10^9	2.1×10^6
Shear modulus (Pa)	26.5×10^9	6.23×10^5
Poisson's ratio	0.3	0.685
Thickness (mm)	1.524	0.127
Mass density (kg/m^3)	2800	970

Table 5.3: Comparisons of natural frequencies for beam G

Mode	Sixth-order Eq.	Finite element model		Finite element model
	Natural frequency(Hz)	CQUAD4 with offset	V_v/V	CQUAD4 without offset
	Natural frequency(Hz)	Natural frequency(Hz)		Natural frequency(Hz)
1	63	63	0.29	39
2	291	291	0.23	241
3	735	734	0.14	675
4	1383	1381	0.08	1325
5	2249	2243	0.05	2193

The natural frequencies predicted from Johnson and Kienholz's model and the sixth-order equation are almost the same for the first five modes, while the finite element model without offset predicts large differences for low order modes.

5.3 Basic concepts of boundary element analysis

A time-harmonic sound pressure field is represented by,

$$p(x, y, z, t) = p(x, y, z)e^{i\omega t}. \quad (5.6)$$

The Helmholtz equation is,

$$\nabla^2 p + k^2 p = 0. \quad (5.7)$$

The acoustic particle velocity is related to the normal derivative of the sound pressure as,

$$v = \frac{i}{\rho\omega} \frac{\partial p}{\partial n}. \quad (5.8)$$

The fundamental solution to the Helmholtz equation, Eq. (5.7) in three dimensions is,

$$G(\mathbf{x}, \mathbf{X}') = \frac{e^{-ikr}}{4\pi r}, \quad (5.9)$$

where r is the distance between the field point \mathbf{x} and the source point \mathbf{X}' . The above fundamental solution satisfies,

$$\nabla^2 G(\mathbf{x}, \mathbf{X}') + k^2 G(\mathbf{x}, \mathbf{X}') = -\delta(\mathbf{x}, \mathbf{X}'), \quad (5.10)$$

where δ is the Dirac delta function.

The boundary integral equation can be found from Green's second identity,

$$\int_S \left(p \frac{\partial G}{\partial n} - G \frac{\partial p}{\partial n} \right) dS = \int_V \left(p \nabla^2 G - G \nabla^2 p \right) dV. \quad (5.11)$$

Substituting the Laplacian $\nabla^2 p$ on the left-hand side of Eq. (5.7), yields

$$\int_S \left(p \frac{\partial G}{\partial n} - G \frac{\partial p}{\partial n} \right) dS = \int_V \left(\nabla^2 G + k^2 G \right) p dV. \quad (5.12)$$

Equations (5.10) and (5.12) give the boundary integral representation of the sound pressure field,

$$p(\mathbf{x}) = \int_S \frac{\partial p(\mathbf{X}')}{\partial n} G(\mathbf{x}, \mathbf{X}') dS - \int_S p(\mathbf{X}') \frac{\partial G(\mathbf{x}, \mathbf{X}')}{\partial n} dS. \quad (5.13)$$

The normal derivative of the fundamental solution is,

$$\frac{\partial G}{\partial n} = -\frac{e^{-ikr}}{4\pi r} \left(ik + \frac{1}{r} \right) \frac{\partial r}{\partial n}. \quad (5.14)$$

For infinite regions, a far-field boundary condition is necessary to guarantee that the solution of the mathematical problem will be a sound wave propagating from the source to infinity, and not vice versa. This condition is called the Sommerfeld radiation condition at infinity,

$$\lim_{r \rightarrow \infty} r \left| \frac{\partial}{\partial r} + ik \right| = 0. \quad (5.15)$$

For larger values of r ,

$$\frac{\partial r}{\partial n} \rightarrow 1, \quad \frac{1}{r} \rightarrow 0, \quad (5.16)$$

then Eq. (5.14) reduces to,

$$\frac{\partial G}{\partial n} + ikG = 0. \quad (5.17)$$

Consider the domain V limited by an infinite rigid plane boundary, S_H , baffle, and another boundary S , as shown in Fig. 5.3. The plane is rigid, so that total reflection occurs

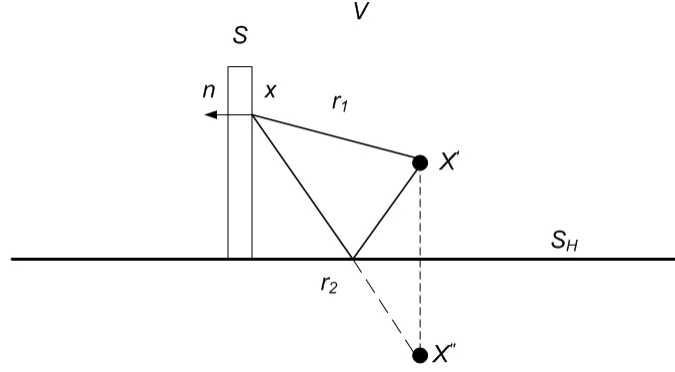


Figure 5.3: Half-space V limited by an infinite rigid plane S_H and boundary S

for waves at any angle of incidence at S_H ,

$$v = 0 \Rightarrow \partial p / \partial n = 0. \quad (5.18)$$

Then the boundary integral equation for the sound pressure field becomes,

$$p(\mathbf{x}) = \int_S \frac{\partial p(\mathbf{X}')}{\partial n} G(\mathbf{x}, \mathbf{X}') dS - \int_{S+S_H} p(\mathbf{X}') \frac{\partial G(\mathbf{x}, \mathbf{X}')}{\partial n} dS. \quad (5.19)$$

The sound pressure p is not zero at S_H . To avoid the discretization of the infinite boundary, the fundamental solution G has to be modified to be satisfied over S_H ,

$$\frac{\partial G(\mathbf{x}, \mathbf{X}')}{\partial n} = 0. \quad (5.20)$$

Using the method of images, the half-space Green's function can be of the form,

$$G(\mathbf{x}, \mathbf{X}') = \frac{e^{-ikr_1}}{4\pi r_1} + \frac{e^{-ikr_2}}{4\pi r_2}, \quad (5.21)$$

where r_1 denotes the distance from \mathbf{x} to \mathbf{X}' and r_2 is the distance from \mathbf{x} to \mathbf{X}'' (the image of \mathbf{X}' with respect to S_H). The second term of Eq. (5.21) represents the reflected waves due to the presence of the infinite plane S_H .

The normal derivative of the half-space Green's function is,

$$\frac{\partial G(\mathbf{x}, \mathbf{X}')}{\partial n} = \frac{1}{4\pi} \left[\left(-\frac{1}{r_1^2} - \frac{ik}{r_1} \right) e^{-ikr_1} \frac{\partial r_1}{\partial n} + \left(-\frac{1}{r_2^2} - \frac{ik}{r_2} \right) e^{-ikr_2} \frac{\partial r_2}{\partial n} \right], \quad (5.22)$$

where n' is the image of n with respect to the plane S_H . For any point \mathbf{x} along S_H , we have

$$r_2 = r_1, \text{ while } \partial r_2 / \partial n = -\partial r_1 / \partial n. \quad (5.23)$$

Then the integral Eq. (5.19) reduces to

$$p(\mathbf{x}) = \int_S \frac{\partial p(\mathbf{X}')}{\partial n} G(\mathbf{x}, \mathbf{X}') \, dS - \int_S p(\mathbf{X}') \frac{\partial G(\mathbf{x}, \mathbf{X}')}{\partial n} \, dS. \quad (5.24)$$

5.4 Boundary element analysis model for fluid-structure-fluid systems

For the conventional multi-domain systems, the acoustic domains are first divided into several subdomains, and the Helmholtz integral equation is applied to each subdomain. Two

interface conditions, the continuity of normal particle velocity and the continuity of sound pressure, are then enforced at the interface between two neighboring subdomains. For the fluid-structure-fluid system, the structure involved is elastic, and the sound pressure has a step across the interface. The fluid-structure-fluid interaction requires a slight modification of the interface conditions. The continuity of normal particle velocity is the same as for fluid-fluid systems, and the second condition becomes the continuity of the normal stress, which relates the normal displacement and the stiffness and mass matrices of the structure to the pressure step across the structure. The stiffness and mass matrices can be obtained from the finite element analysis.

Consider a fluid-structure-fluid system, as illustrated in Fig. 5.4. An elastic panel, occupies the domain Σ on the plane $z = 0$ in a three-dimensional space. The baffle occupies the region Σ' and is perfectly rigid. The two half spaces Ω_1 ($z < 0$) and Ω_2 ($z > 0$) contain a fluid. The system is excited by a simple harmonic sound source, $O(Q)e^{i\omega t}$, located in Ω_1 at point Q , (x, y, z) .

Let $w(U) = w(x, y)$ be the panel normal displacement of node U , located at $(x, y, 0)$; $p_2(Q) = p_2(x, y, z)$ and $p_1(Q) = p_1(x, y, z)$ denote the sound pressure fields, in Ω_2 and Ω_1 fields, respectively. The sound pressure step $q(Q) = q(x, y)$ across the panel, is defined by,

$$q(x, y) = \lim_{l \rightarrow 0} |p_1(x, y, -l) - p_2(x, y, l)|, \quad l > 0. \quad (5.25)$$

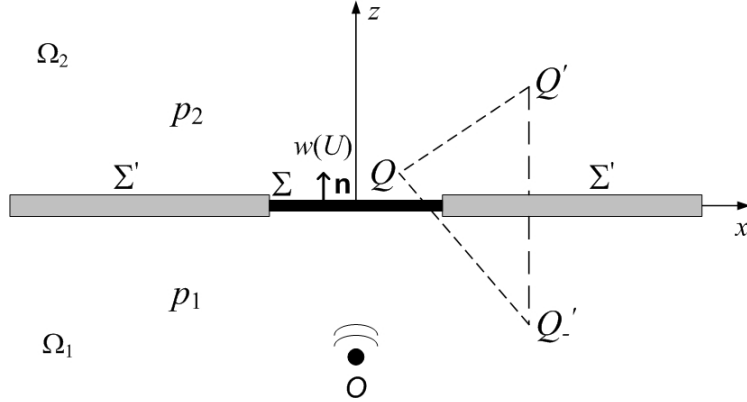


Figure 5.4: Sound fields Ω_1 and Ω_2 created by a baffled planar vibrating structure

Then the sound pressure functions $p_2(Q)$ and $p_1(Q)$ satisfy the Helmholtz equation,

$$(\nabla^2 + k^2)p_2(Q) = 0, \quad Q \in \Omega_2 \quad \text{and} \quad (\nabla^2 + k^2)p_1(Q) = O(Q), \quad Q \in \Omega_1. \quad (5.26)$$

At the interface, the continuity of normal stress produces,

$$(K - M\omega^2)w(U) = q(U), \quad U \in \Sigma, \quad (5.27)$$

where K and M are the stiffness and the mass matrix of the panel, respectively.

The continuity of normal velocity gives,

$$\frac{\partial p_2(U)}{\partial n} = -\frac{\partial p_1(U)}{\partial n} = \rho_f \omega^2 w(U), \quad U \in \Sigma. \quad (5.28)$$

where ρ_f is the mass density of the fluid, and \mathbf{n} is the unit normal vector to the surface Σ , outward to the sound pressure field Ω_2 .

On the baffle plane, we have,

$$\frac{\partial p_2(U)}{\partial n} = \frac{\partial p_1(U)}{\partial n} = 0 \text{ and } w(U) = 0, U \in \Sigma'. \quad (5.29)$$

The half-space Green's function is expressed as,

$$G(Q, Q') = \frac{e^{-ikr(Q, Q')}}{4\pi r(Q, Q')} + \frac{e^{-ikr(Q, Q'_-)}}{4\pi r(Q, Q'_-)}, \quad (5.30)$$

where the coordinates of the points Q' and Q'_- are (x', y', z') and $(x', y', -z')$, respectively.

The structure and the baffle are coplanar. Thus, the normal derivative of the modified Green's function is zero along Σ . The sound pressure fields can be written as,

$$p_2(Q) = \omega^2 \rho_f \int_{\Sigma} w(U') G(Q, U') dS(U'), \quad Q \in \Omega_2, \quad (5.31)$$

$$p_1(Q) = p_0(Q) - \omega^2 \rho_f \int_{\Sigma} w(U') G(Q, U') dS(U'), \quad Q \in \Omega_1, \quad (5.32)$$

where $p_0(Q)$ is the sound pressure generated by the source and its image, in the presence of the baffle.

Hence, we have the equation for the panel displacement:

$$(K - M\omega^2)w(U) + 2\rho_f\omega^2 \int_{\Sigma} w(U') G(U, U') dS(U') = p_0(U), \quad U \in \Sigma. \quad (5.33)$$

The discretization by finite elements of the panel yields the matrix equation,

$$[\mathbf{K} - (\mathbf{M} + 2\mathbf{B})\omega^2]\mathbf{w} = \mathbf{F}, \quad (5.34)$$

where \mathbf{B} is the complex symmetric matrix associated with the fluid, which depends on the wave number in the z direction, k_z , and \mathbf{F} is the loading matrix acting on the plane structure. The equation above is similar to the equation derived by Mariem and Hamdi [32], although the factor of \mathbf{B} is 4 in their work.

The sound pressure in the incident plane wave can be written as,

$$p_{\text{inc}} = P_{\text{inc}} \exp\{i\omega t - ik(x \sin \theta \cos \phi + y \sin \theta \sin \phi + z \cos \theta)\}, \quad (5.35)$$

where P_{inc} is the amplitude of the source, θ is the angle of incidence, and ϕ is the angle of rotation. Then the wave number k in Eq. (5.30) is evaluated as $k \cos \theta$.

The sound transmission coefficient is defined as,

$$\tau = \frac{W_r}{W_i}, \quad (5.36)$$

where W_i denotes the virtual sound power flow, which would pass through the surface of the panel, if the panel were removed.

$$W_i = \frac{|P_{\text{inc}}|^2 S \cos \theta}{2\rho_f c_f}, \quad (5.37)$$

where c_f is the sound speed in the fluid. The sound power radiated by the panel in the semi-infinite fluid domain, W_r , is given by,

$$W_r = \frac{1}{2} \operatorname{Re} \left(\int_S v_n^*(U) p_r(U) dS(U) \right) = \frac{1}{2} \operatorname{Re} \left(- \int_S i\omega w^*(U) p_r(U) dS(U) \right), \quad U \in \Sigma. \quad (5.38)$$

with $p_r(U) = \omega^2 \rho_f \int_{\Sigma} w(U') G(U, U') dS(U')$.

Theoretically, modal superposition method is numerically equivalent to the direct response method if the modal basis consists of all modes of the structure. The modal superposition method can be used to evaluate the frequency response of the normal displacement in the form of a linear combination of modal eigenvectors,

$$\mathbf{w} = \sum_j a_j \{\psi_j\} = [\psi] \{a\}, \quad (5.39)$$

where $\{a\}$ contains the modal participation factors, and $[\psi]$ is a matrix, whose columns are the modal eigenvectors. Compared to the direct response method, the modal superposition method has the advantage of allowing faster calculations once the modes are determined.

Then Eq. (5.34) can be expressed as,

$$([\psi]^T [\mathbf{K} - (\mathbf{M} + 2\mathbf{B})\omega^2] [\psi]) \{a\} = [\psi]^T \mathbf{F}. \quad (5.40)$$

The structural damping can be introduced by adding a fraction matrix η ,

$$([\psi]^T[\mathbf{K}(1 + i\eta) - (\mathbf{M} + 2\mathbf{B})\omega^2][\psi])\{a\} = [\psi]^T\mathbf{F}. \quad (5.41)$$

When the modal eigenvectors are generalized with respect to mass, the following relations are obtained,

$$\{\psi_i\}^T\mathbf{K}\{\psi_j\} = \begin{cases} \lambda_i = \omega_i^2 & i = j \\ 0 & i \neq j \end{cases}, \text{ and } \{\psi_i\}^T\mathbf{M}\{\psi_j\} = \begin{cases} 1 & i = j \\ 0 & i \neq j \end{cases}. \quad (5.42)$$

Hence Eqs. (5.40) and (5.41) are only associated with the element mesh, the eigenvalues λ , and the generalized modal eigenvectors, ψ .

The natural frequency f_{mn} of a simply supported single-layer panel can be evaluated by,

$$Dk^4 = m\omega^2, \text{ with } k_{mn}^2 = (m\pi/l_x)^2 + (n\pi/l_y)^2, \omega = 2\pi f, \quad (5.43)$$

where l_x and l_y are the dimensions of the panel. The modal eigenvectors of normal displacements can be expressed as,

$$\phi_{mn} = V_{mn} \sin(m\pi x/l_x) \sin(m\pi y/l_y), \quad (5.44)$$

where the amplitude V_{mn} can be obtained from finite element analysis.

Table 5.4: Natural frequencies and generalized modal amplitudes of panel H

Mode	(m, n)	From Eq.(5.43)	MSC Nastran	V_{mn}
		Frequency (Hz)	Frequency (Hz)	
1	(1,1)	52.9	52.9	1.1414531
2	(2,1)	85.5	85.5	1.1432148
3	(3,1)	140.0	140.2	1.1461568
4	(1,2)	178.7	179.5	1.1463532
5	(2,2)	211.4	211.9	1.1481224
6	(4,1)	216.2	217.2	1.1502883
7	(3,2)	265.8	266.1	1.1510770
8	(5,1)	314.2	316.9	1.1556219
9	(4,2)	342.1	342.5	1.1552263
10	(1,3)	388.4	392.8	1.1545663
11	(2,3)	421.1	424.9	1.1563482
12	(6,1)	434.0	440.0	1.1621734
13	(5,2)	440.1	441.6	1.1605831
14	(3,3)	475.6	478.5	1.1593239
15	(4,3)	551.8	554.0	1.1635029
16	(6,2)	559.9	563.8	1.1671624

The generalized modal eigenvectors of a 3.175 mm thick aluminum panel, panel H , were computed by MSC Nastran. The 0.84 m \times 0.428 m panel was divided into 40 \times 24 CQUAD4 elements. The generalized modal amplitudes V_{mn} with respect to the mass are given in Table 5.4.

A boundary element method (BEM) computer program in MATLAB language was developed to calculate the sound transmission loss of the aluminum panel H . The modal supposition method was employed and the first 16 modes were included. The structural modal damping was assumed to be constant over all frequencies. Two different structural loss factors were examined, $\eta = 0.001, 0.005$. The frequency increment used was 1 Hz. The calculated sound transmission loss values of the aluminum panel H for sound waves at normal incidence are shown in Fig. 5.5.

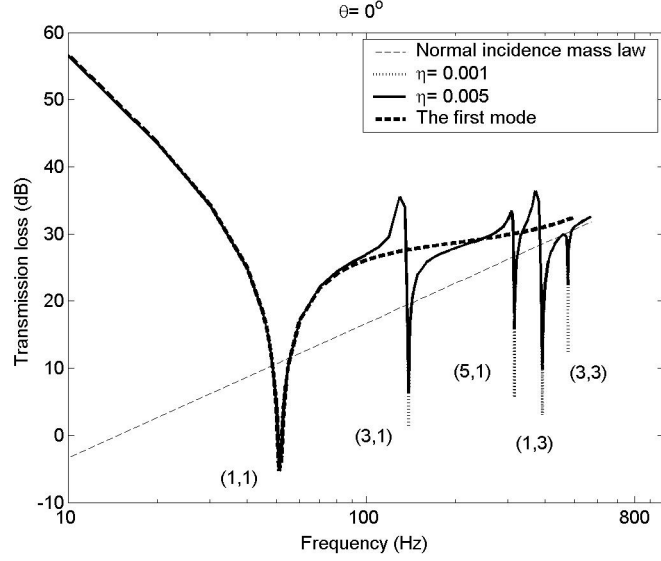


Figure 5.5: Calculated sound transmission loss values of the aluminum panel H for sound waves at normal incidence using the BEM computer program

It was found that the presence of the fluid modifies the resonance characteristics of the panel, slightly shifting modal frequencies to lower frequencies. The effect of damping on sound transmission loss is noticeable around resonance frequencies. It is seen that the radiated power is greater than the virtual power flow at the resonance frequencies of the first several modes.

The specific acoustic impedance of the half-space Green's function, Eq. (5.30), is identical to that of a spherical wave,

$$Z = \frac{i\rho_f c_f k r}{1 + ikr} = \rho_f c_f \left(\frac{k^2 r^2}{1 + k^2 r^2} + i \frac{kr}{1 + k^2 r^2} \right). \quad (5.45)$$

Unlike the specific acoustic impedance of a plane sound wave, the specific acoustic impedance of a spherical sound wave has both resistive and reactive components. When $kr \gg 1$, the specific acoustic impedance approaches $\rho_f c_f$, the specific acoustic impedance of a plane wave. For boundary element analysis, both the resistive and reactive components are required. The virtual sound power flow, Eq. (5.37), is defined by using plane wave concepts, and the radiated power, Eq. (5.38), is associated with the specific acoustic impedance of spherical waves. That may explain why the radiated sound power is greater than the virtual sound power flow at low order resonance frequencies.

When a plane wave is normally incident on the panel, the sound pressure generated by the source and its image on the panel, $p_0(U)$, is uniform (see Eq. (5.35)). Only odd-odd (volume displacing) modes are excited, so only odd-odd modes radiate power. It is seen that the transmission loss curve generated by the first mode, (1,1), is much higher than the mass law curve above its resonance frequency, and it approaches the mass law curve with increasing frequency.

The sound pressure in a plane wave obliquely incident on the panel, depends on the angle of incidence, θ , and the angle of rotation, ϕ . Thus it should be expected that the transmission loss of the aluminum panel will also depend on the angle of rotation, ϕ . A comparison of the sound transmission loss values of the aluminum panel H for sound waves at oblique incidences predicted using the computer program is presented in Fig. 5.6.

When a plane wave is obliquely incident on the panel, along the x -axis direction, ($\phi = 0^\circ$), the sound pressure generated by the source and its image on the panel, $p_0(U)$, is constant

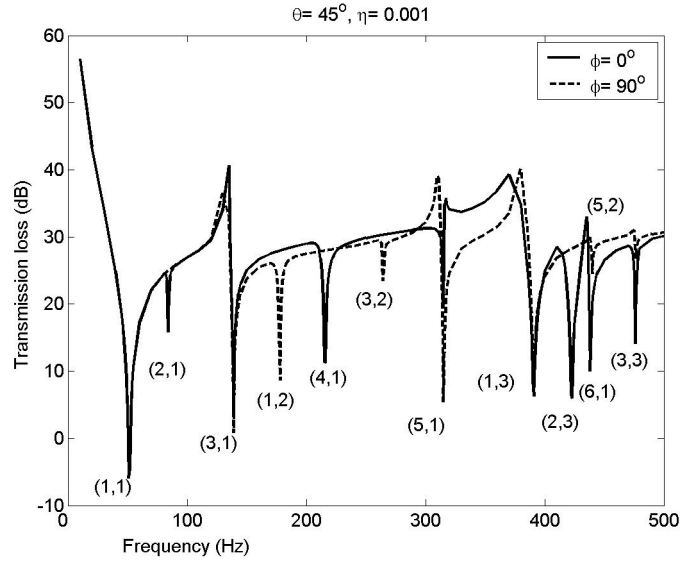


Figure 5.6: Calculated sound transmission loss values of the aluminum panel H for sound waves at oblique incidence using the BEM computer program

along the y -axis direction. Then the radiated power for odd-even or even-even modes of the panel is quite small. Hence the resonance dips in the predicted sound transmission loss along the x -axis direction ($\phi = 0^\circ$), occur at the resonance frequencies whose y -axis mode numbers are odd. Likewise, the resonance dips in the predicted transmission loss along the y -axis direction ($\phi = 90^\circ$), occur at the resonance frequencies whose x -axis mode numbers are odd (see Table 5.4). Since the sound pressure generated by the source and its image on the panel, $p_0(U)$, is less sensitive to the angles of incidence and rotation at low frequencies, the effect of angle of rotation on sound transmission loss is negligible in that region.

A commercial boundary element analysis software, LMS SYSNOISE, was also used to calculate the sound transmission loss of the aluminum panel H . A finite element model

database and a boundary element indirect baffled model database were defined in the software. The element mesh, 40×24 CQUAD4 elements, was imported to the software as the structural meshes for both databases and to occupy on the plane $z = 0$. The computed eigenvectors of the first 16 modes obtained from MSC Nastran were imported to the software as the structural modes in the finite element model database. A plane wave source was defined in the boundary element model database at 5 m below the center of the panel. The two databases were linked to solve the displacement of the aluminum panel. LMS SYSNOISE does not directly calculate the radiated power of planar structures, but it does provide an alternative method to estimate the radiated sound intensity from planar structures, by integration of the sound power through a field point mesh, which covers the receiver side of the structure. A hemisphere with 1 m radius was used for the field point mesh.

Comparisons of sound transmission losses of the aluminum panel H for plane sound waves at normal and oblique incidences calculated using the BEM computer program and the transmission loss model in the boundary element analysis software are given in Figs. 5.7 and 5.8. In both cases, the structural damping was assumed to be constant for all modes and the structural loss factor was assumed to be $\eta = 0.001$; the frequency increment used was 1 Hz.

The predictions from the BEM computer program and the TL model in the boundary element analysis software are quite similar, although there are some differences. In the software, the velocity field is obtained by differentiation of the pressure field at the Gauss

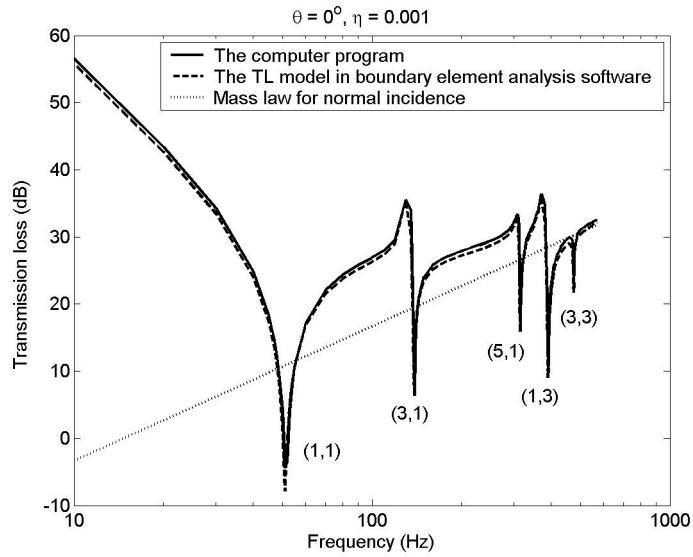


Figure 5.7: Predicted sound transmission loss values of the aluminum panel H for sound waves at normal incidence

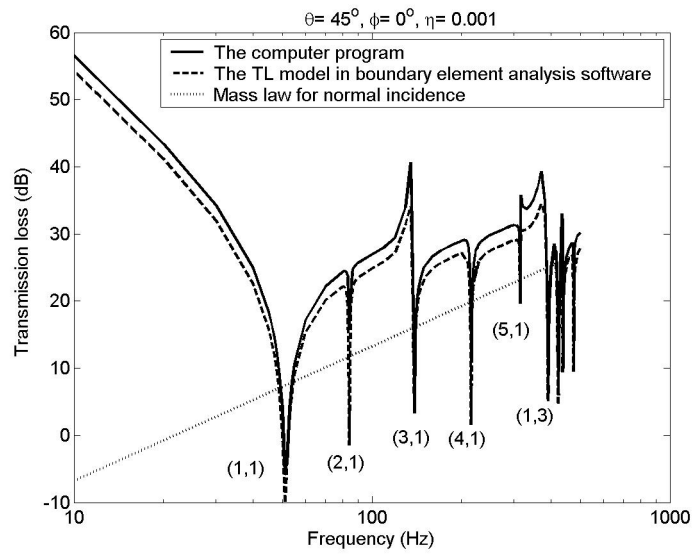


Figure 5.8: Predicted sound transmission loss values of the aluminum panel H for sound waves at oblique incidence

points of the elements of the field point mesh and then extrapolation and averaging are carried out at the nodes. Hence the estimated sound power radiated depends on the field point mesh and the Gauss points. The estimates of radiated sound power can become more accurate if a finer field point mesh or more Gauss points are used.

5.5 Boundary element analysis model for three-layer symmetric sandwich panels

For a three-layer sandwich panel, the generalized modal eigenvectors of the normal displacements of the face sheets can be written as,

$$\phi_{mn} = \begin{cases} V_{mn,2}\text{func}(m, n, x, y, z), & z > 0 \\ V_{mn,1}\text{func}(m, n, x, y, z), & z < 0 \end{cases}. \quad (5.46)$$

These generalized eigenvectors can be obtained from the finite element model for sandwich structures given by Johnson and Kienholz [48]. In their model, for symmetric sandwich panels, the normal displacements of the face sheets are the same. Hence the three-layer symmetric sandwich panel can be treated as an equivalent single-layer panel whose generalized modal eigenvectors satisfy,

$$\psi'_{mn} = V'_{mn}\text{func}(m, n, x, y) \text{ with } V'_{mn} = V_{mn,2} = V_{mn,1}. \quad (5.47)$$

In the previous section, it was shown that Eqs. (5.40) and (5.41) are only associated with the element mesh, the eigenvalues λ , and the generalized modal eigenvectors of the structure. Then only the generalized eigenvectors for one face sheet of the symmetric sandwich panel are required in this boundary element analysis model. The sound transmission coefficient can be computed from Eqs. (5.36) \sim (5.38) and the sound transmission loss can be determined with Eq. (3.41).

To verify the proposed model, the aluminum panel H was modeled as a single-layer panel and a three-layer panel using the finite element model presented by Johnson and Kienholz [48], $t_1 = t_2 = 0.24$ mm, $h = 2.195$ mm. The finite element mesh of the three-layer panel was generated in MSC Nastran, and consisted of 40×24 CQUAD4 elements for each face sheet, and 40×24 HEXA elements for the core. The finite element mesh of the single-layer panel consisted of 40×24 CQUAD4 elements. The calculated natural frequencies and generalized amplitudes V_{mn} , with respect to the mass, for the clamped aluminum panel H , are given in Table 5.5. It is seen that the two finite element models predict almost the same natural frequencies and generalized amplitudes.

The sound transmission characteristics of the clamped aluminum panel H in the single-layer model case and the three-layer model case were computed by using LMS SYSNOISE. In the single-layer model case, the sound transmission loss values were obtained by using the TL model described in Sec. 5.4. In the three-layer model case, the structural mesh used in the boundary element analysis is not the entire element mesh that consists of CQUAD4 and HEXA elements. Only the element mesh of one face sheet, 40×24 CQUAD4 elements,

Table 5.5: Natural frequencies and generalized amplitudes of the clamped aluminum panel H

Mode	(m,n)	Single-layer model		Three-layer model	
		Frequency (Hz)	Amplitude V_{mn}	Frequency (Hz)	Amplitude V_{mn}
1	(1,1)	104.9	1.3873931	104.5	1.3862565
2	(2,1)	137.0	1.3394921	136.4	1.3382779
3	(3,1)	194.6	1.3268757	193.5	1.3257434
4	(1,2)	273.6	1.2870189	271.5	1.2858151
5	(4,1)	277.6	1.3145773	275.6	1.3140515
6	(2,2)	304.4	1.2745483	302.1	1.2627527
7	(3,2)	357.7	1.2642025	355.1	1.3862565
8	(5,1)	385.4	1.3166149	381.7	1.3161944

was imported to the software as the structural meshes for both databases and to occupy on the plane $z = 0$. Then the computed eigenvectors of the face sheet were imported to the software as the structural modes in the finite element model database. The estimates of the radiated sound powers were found to be almost the same for both cases.

5.6 Conclusions

The presence of fluid modifies the resonance characteristics of the structure. The radiated sound power of a planar structure can be higher than the virtual sound power flow near the lower order resonance frequencies. The damping increases the sound transmission loss near the resonance frequencies. For finite single-layer isotropic rectangular panels, the sound transmission loss also depends on the angle of rotation, ϕ . The contribution of other than odd-odd modes on the sound transmission loss for single-layer isotropic panels is negligible for plane sound waves at normal incidence, while those can be substantial for plane sound waves at oblique incidence. The sound transmission loss values are less sensitive

to the damping and the angle of incidence at low frequencies. Good agreement was found between the predications obtained from the BEM computer program and the TL model of the boundary element analysis software.

A boundary element analysis model is presented to obtain the sound transmission loss of three-layer symmetric sandwich panels. Only the eigenvectors of one face sheet are required in the analysis. Hence, this incurs only a minimum increase in computation effort relative to single-layer structures.

CHAPTER 6

MATERIALS AND MATERIAL PROPERTIES

6.1 Introduction

A sandwich structure consists of three or more constituents, the face sheets, the core and the adhesive joints. The introduction of fiber composites allows the choice of a great number of face sheet materials. The number of available cores also has increased because of the introduction of cellular plastics. Since the material properties of composites are very dependent on the manufacturing process, there is usually a large number of material data for composites, especially data for fiber composites. In a few papers on sound transmission through sandwich composite structures, parameters of material properties used in predictions were determined experimentally, based on resonance frequency measurements [6, 8]. Moore and Lyon [6] determined the core material parameters experimentally, based on resonance frequency measurements with a layer of core material sandwiched between rigid metal discs. Nilsson and Nilsson [8] separated the face sheets from the foam core and simulated a free-free beam boundary condition to determine the E -moduli of the face sheets and foam core.

In this chapter, the materials commonly used in sandwich structures are reviewed, especially the composite materials for the sandwich structures investigated in this study. The experimental methods used to obtain material properties of the face sheets and core

of sandwich structures are discussed. The estimated material properties of the sandwich structures used in this study are also presented.

6.2 Materials

“Almost any structural material which is available in the form of a thin sheet may be used to form the faces of a sandwich panel” [52], gives a good view of material selection for the face sheets of sandwich structures. The properties of primary interest for the face sheets of sandwich structures are stiffness, strength, impact resistance, surface finish, environmental resistance and wear resistance. Common face sheet materials can be divided into two main groups: metallic and non-metallic materials.

The advantages of using metal for the face sheets include high stiffness and strength, low cost, good surface finish, and high impact resistance. The drawbacks include high mass density and difficulty in manufacturing sandwich structures.

Most non-metallic composites offer strength properties similar to those of metals. The manufacturing of non-metallic composite sandwich structures is much easier than the manufacturing of metal face sheet sandwich structures. The most important non-metallic materials are fiber reinforced composites. Glass fibers have good mechanical and environmental resistance properties. Their main drawbacks are that their elastic moduli are fairly low and their mass densities are higher than those of other reinforcements.

Aramid fibers made from aromatic polyimide, have low mass densities, and high stiffness and high strength properties. It is difficult to machine aramid fibers, however, because

of their extremely wear resistance. Graphite fibers are built-up from long carbon-carbon molecular chain yielding very strong fibers. Graphite fibers are among the strongest and stiffest composite materials when they are combined with matrix systems to produce high-performance structures. Graphite fibers have a low coefficient of thermal expansion, and good friction properties. Their main drawbacks are their high cost and relatively brittleness.

Common composite face sheet material forms can be divided into two main groups, laminate and textile structures. Textile structures include unitapes and 2-D woven fabrics. Unitapes have maximum structural properties in the fiber direction, while they are much poorer in the direction transverse that in the fiber direction. 2-D woven fabrics are more expensive than unitapes, however the lay-up lab requirements are reduced in manufacturing operations. Common 2-D woven fabrics include unidirectional fabrics, plain weave fabrics and satin weave fabrics. Among them, plain weave is the most stable construction and has minimum slippage. The strength is uniform in both directions. A laminate is a stack of lamina comprised of a layer of fibers in a matrix. The rule-of-mixtures is used to estimate the properties of a lamina [62]. Classical lamination theory is applied to calculate the properties of a laminate.

Core materials are of the same importance as the face sheet materials and the least knowledge exists about their properties. Cores in sandwich structures can be divided into two main groups, honeycombs and foams. The properties of primary interest of the core include mass density, shear modulus, shear strength, stiffness perpendicular to the face sheets, thermal insulation and acoustic insulation.

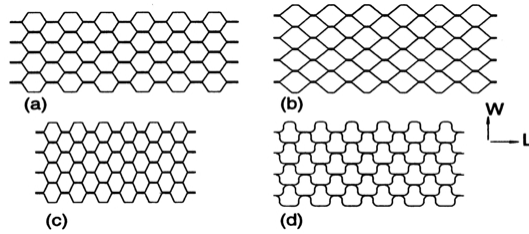


Figure 6.1: Commonly used cell configurations for honeycomb core materials (a) hexagonal (b) square (c) over expanded hexagonal (d) flex

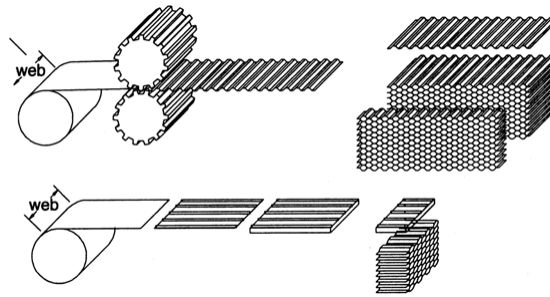


Figure 6.2: Manufacture of honeycomb cores - corrugating (top) and expansion (bottom) processes

Honeycomb core materials have been developed and used primarily in aerospace applications. Honeycomb materials can be manufactured with a variety of cell shapes. The commonly used cell configurations for honeycombs are shown in Fig. 6.1.

The manufacture of honeycombs is conducted in two different ways, as illustrated in Fig. 6.2. The corrugating process requires that pre-corrugated metal sheets are stacked into blocks and bonded together. When the adhesive has cured, blocks with the required thickness can be cut from the stack. The corrugating process is usually used for high density metal honeycombs.

The expansion process begins with the stacking of thin plane sheets of the web material on which adhesive node lines have been printed. When the adhesive has cured, the honeycomb block may be expanded by pulling in the W -direction until a desired cell shape has been achieved (see Fig. 6.1). Metal honeycombs are cut into the desired thickness prior to expansion, and when expanded they retain their shapes since the material yields plastically. Non-metallic materials, such as impregnated fiber mats or paper, are heat treated after expansion to retain their shapes. Then the materials are dipped in resin, which is cured in an oven. After this process is completed, the core is sliced.

Due to the manufacturing methods involved, most honeycombs have not only different out-of-plane properties but also different in-plane properties from each other. Honeycombs have excellent mechanical properties. These include very high stiffness perpendicular to the plane, and the highest shear stiffness- and strength-to-weight ratios of all available core materials. Their main drawbacks are high cost and difficult handling during lay up of sandwich element.

Gibson and Ashby [53] derived an expression for the out-of-plane shear moduli of regular hexagonal honeycomb cores,

$$G_{LT} = G_{WT} = 1.15G_s t/s, \quad (6.1)$$

where t is the cell wall thickness, s is the diameter of a circle inscribed in the hexagonal cell, and G_s is the shear modulus of the cell wall material. In practice, regular hexagonal

honeycomb cores have double cell walls in the L -direction due to their manufacture (see Fig. 6.1). Then the shear modulus estimation is modified to [54],

$$G_{LT} = 4tG_s/(3s), \quad G_{WT} = 16tG_s/(30s). \quad (6.2)$$

For square cells the shear moduli are [54],

$$G_{LT} = G_{WT} = tG_s/s. \quad (6.3)$$

Foams do not offer the same high stiffness- and strength-to-weight ratios as honeycombs. Foams can be manufactured from a variety of synthetic polymers and are generally less expensive. Foams offer high thermal insulation and acoustical damping. The foam surface is easy for bonding. The manufacturing operation of sandwich elements with foams is much easier than that with honeycombs.

Polyurethane (PUR) foams have low thermal conductivity, very good insulation properties and poor mechanical properties. PUR foams are probably the least expensive of all available core materials. That PUR foams can also be foamed in-situ gives an integrating manufacturing in conjunction with the manufacturing of the sandwich elements.

Polystyrene (PS) foams have good mechanical and thermal insulation properties, and they are low cost. Their main drawback is their sensitivity to solvent. Polyvinylchloride (PVC) foams are the most frequently used foams and they have quite good mechanical

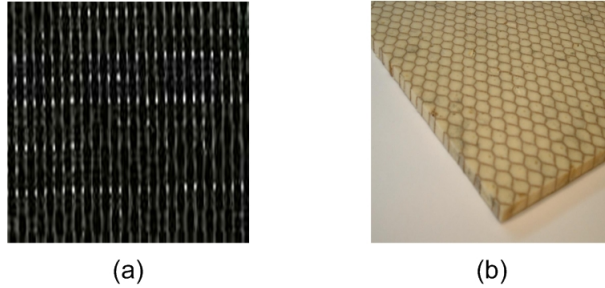


Figure 6.3: The face sheet (a) and core (b) materials of sandwich structures in this study

properties. Polymethacrylimide (PMI) foams have the best mechanical properties and are more expensive than other foams.

All sandwich structures tested in this study have plain weave fabric-reinforced graphite composites as the face sheet materials, and PUR foam-filled paper honeycombs as the core materials. The combination of PUR foam and honeycomb materials gives the core the advantage of possessing both foam and honeycomb properties, a high shear modulus, and a large bonding area.

6.3 Measurement methods for materials

Moore and Lyon [6] estimated the honeycomb stiffnesses from resonance frequency measurements on a test sample consisting of a thin layer of honeycomb sandwiched between rigid metal disks. They found that such tests gave values for the main diagonal axial stiffnesses C_{11} , C_{22} , C_{44} and C_{55} . The off-diagonal stiffnesses C_{13} , C_{23} , and C_{12} were arbitrarily assumed to be equal to 0.1 times the softer of the axial stiffnesses.

Nilsson [8] simulated a free-free beam boundary condition by suspending a beam by strings. The beam was excited by an impact in a direction perpendicular to the plane of the beam. The loss factors were derived from half-power bandwidth measurements for various resonances.

In this study, a free-free beam boundary condition was simulated in two ways. In one case the beam was excited with white noise by a shaker mounted at its center. Since the force is applied at the center of the beam, then the center can be considered approximately as a node of the standing waves. It is expected that only odd modes of the beams are excited successfully. In the other case the beam was suspended by strings at the two ends. The beam was excited by an impact in a direction perpendicular to the plane of the beam. In both cases, the response functions were measured by an accelerometer mounted on the beam. The modal loss factors were derived from half-power bandwidth method at various resonances determined from the response function measurements.

In order to verify the hypotheses concerning free-free boundary conditions, a 61 cm long, 2.54 mm wide, 6.35 mm thick, aluminum beam was excited in both ways. The admittance-frequency response functions of the aluminum beam for two cases are shown in Figs 6.4 and 6.5.

It is seen that the even modes are suppressed when the beam is excited by a shaker mounted at the center. The resonance frequencies of odd modes are slightly lower than those obtained from the impact set-up. There is more noise in the impact system than in

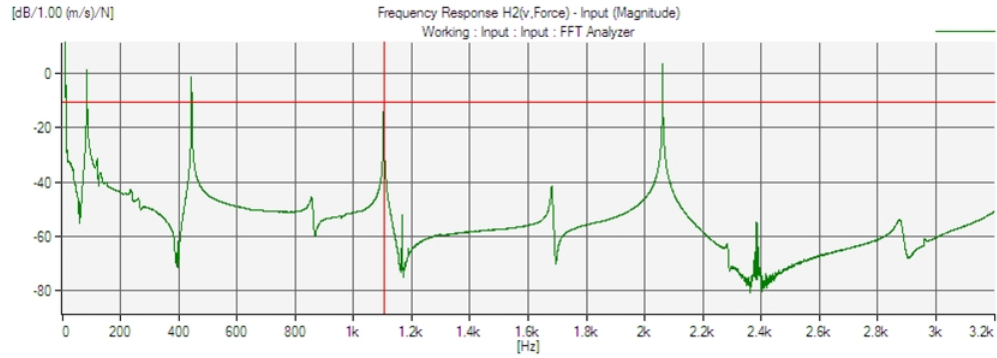


Figure 6.4: The frequency response function of the aluminum beam for the shaker set-up

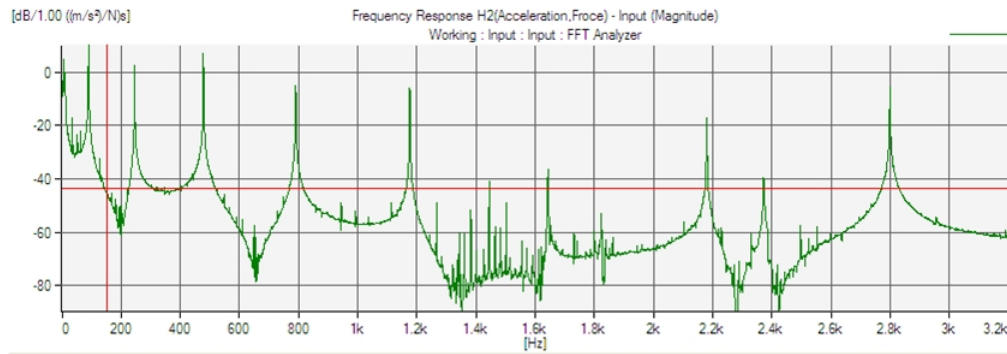


Figure 6.5: The frequency response function of the aluminum beam for the impact set-up

the shaker system. The measured resonance frequencies and loss factors of the aluminum beam are given in Table 6.1.

The natural frequencies of a free-free single-layer beam are,

$$f = \xi \frac{\pi}{8L^2} \sqrt{\frac{Et^2}{12\rho}}, \quad \xi = 3.011^2, 5^2, 7^2, \dots, \quad (6.4)$$

The exact natural frequencies were computed by assuming $E = 70 \text{ GPa}$, $\rho = 2700 \text{ kg/m}^3$.

Table 6.1: Measured resonance frequencies and loss factors of the aluminum beam

Mode		1	2	3	4	5	6	7	8
Shaker	f (Hz)	83		442		1102		2060	
	η (%)	1.8		0.21		0.1		0.04	
Impact	f (Hz)	88	244	476	789	1174	1642	2178	2798
	η (%)	1.15	0.41	0.22	0.12	0.1	0.09	0.06	0.05
Exact	f (Hz)	89	246	483	790	1192	1665	2216	2847

The resonance frequencies obtained from the impact set-up are all within 2% of the predicted values, when a free-free boundary condition is assumed. The resonance frequencies obtained from the shaker set-up are within 9% of the predicted values for the same condition. The two set-ups give the similar modal loss factor values, of the order 0.1%, except in the low frequency region. The experimental loss factor includes both the internal loss in the structure and the loss at the boundaries of the structure element in the low frequency region. This fact may explain the high values of the first few modal loss factors.

6.4 Experimental resonance frequencies of sandwich beams

Honeycomb materials have different stiffnesses in planes perpendicular and parallel to the direction of the cells. It was assumed that the cells of the honeycomb are aligned perpendicular to the plane of the sandwich structures in this study. Most foam cores are only moderately anisotropic and have fairly similar in-plane properties. Thus the foam-filled honeycomb cores were assumed to be orthotropic.

Measurements were performed on beams representing the two main in-plane directions of the panels. For materials tested in two directions of the structure, the results are assigned subscripts x or y to indicate the orientations of the beam. Test samples in the form of beams

Table 6.2: Properties of the sandwich beams

Beam	Face sheets				Core	
	Length (cm)	Width (cm)	Thickness (mm)	Density (kg/m ³)	Thickness (cm)	Density (kg/m ³)
I_x	114.3	3.0	0.33	1900	0.635	160
I_y	53.3	3.2	0.33	1900	0.635	160
J_x	103.8	3.2	0.50	1600	0.635	160
J_y	54.5	3.2	0.50	1600	0.635	160
K_x	101.6	4.4	0.50	1600	1.27	120
K_y	53.0	4.1	0.50	1600	1.27	120
L_x	104.8	3.2	0.33	1900	2.54	70
L_y	54.9	3.5	0.33	1900	2.54	70

were cut out from four symmetric composite sandwich panels. The configurations are given in Table 6.2. The estimated densities of the face sheets include the density of the plain weave fabrics and the adhesive. The sandwich structures were assumed to be homogenous.

Beams I_x , I_y , J_x and J_y have the same foam-filled honeycomb core. Beams J_x , J_y , K_x and K_y with two layers of plain weave fabrics for each face sheet were treated as three-layer sandwich structures. All sandwich beams are lightweight, ~ 3 kg/m². In order to minimize effects of mass loading, an Endevco model 22 piezoelectric accelerometer, mass of 0.14 g, was employed to measure the responses of the beams. For each test specimen, the measurements were repeated several times. The resonance frequencies of all sandwich beams were obtained by using the impact method discussed in the previous section. The admittance-frequency functions of all eight beams are shown in Figs. 6.6 \sim 6.13.

For sandwich beams I_x , J_x and K_x , at least the first 10 modes can be identified, and for sandwich beams I_y , J_y and K_y , the first six modes can be identified, corresponding to

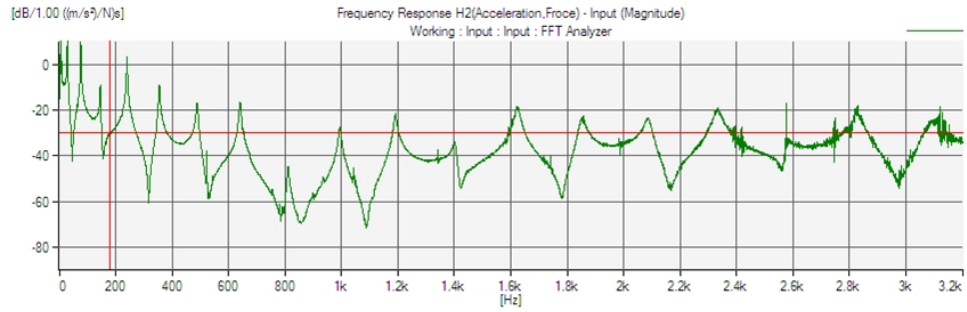


Figure 6.6: The frequency response function of beam I_x

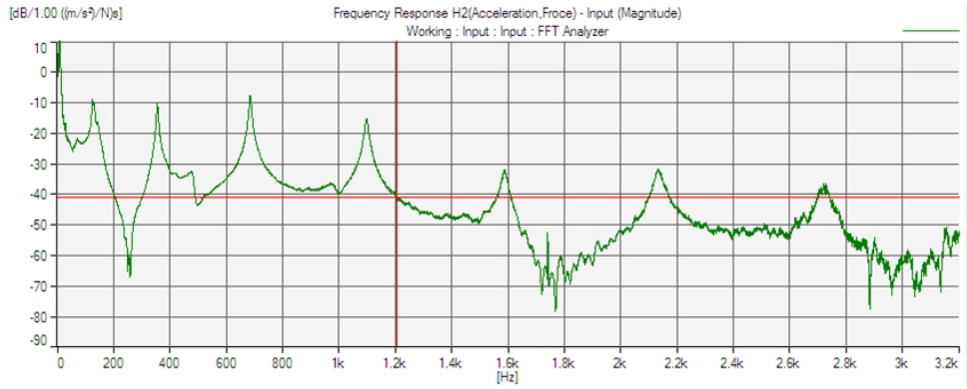


Figure 6.7: The frequency response function of beam I_y

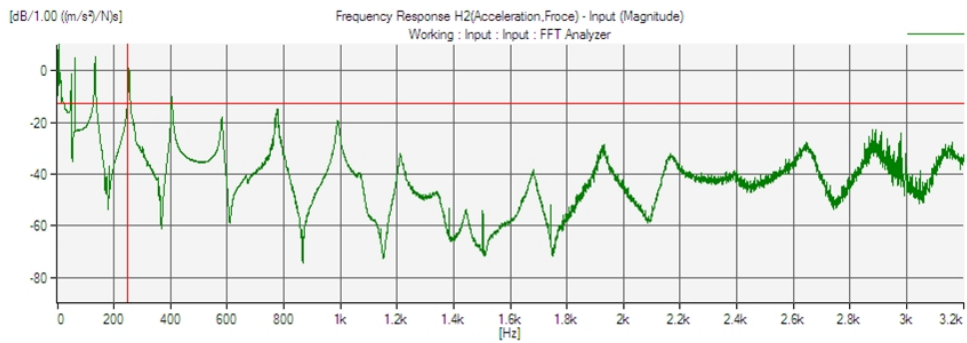


Figure 6.8: The frequency response function of beam J_x

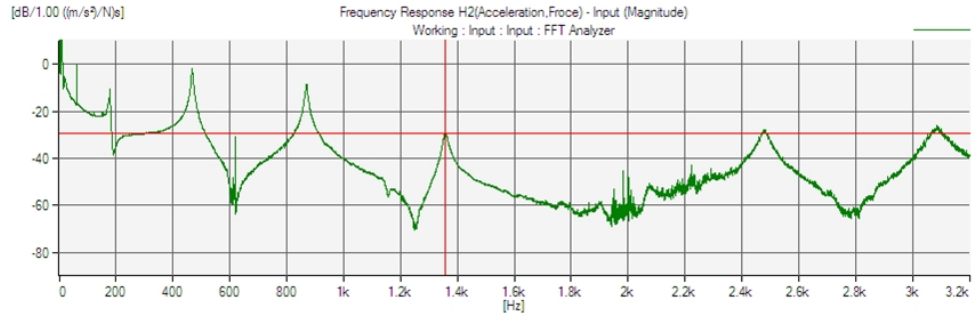


Figure 6.9: The frequency response function of beam J_y

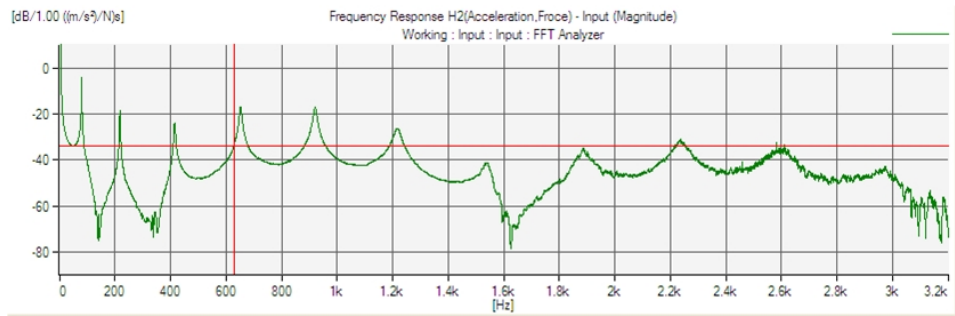


Figure 6.10: The frequency response function of beam K_x

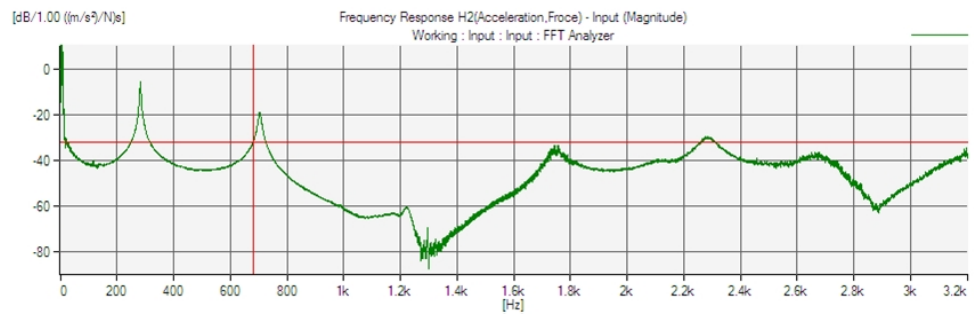


Figure 6.11: The frequency response function of beam K_y

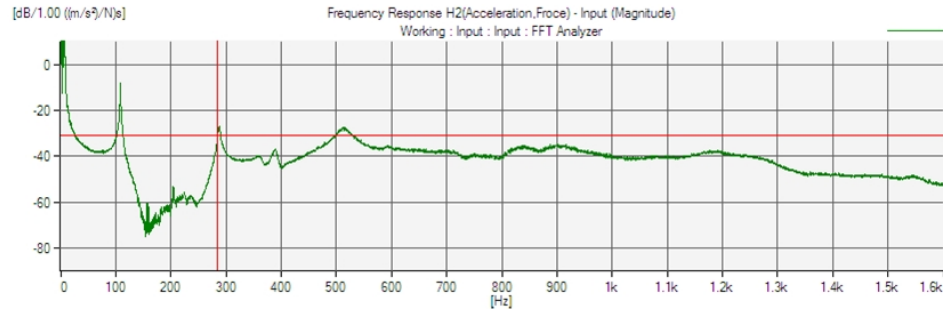


Figure 6.12: The frequency response function of beam L_x

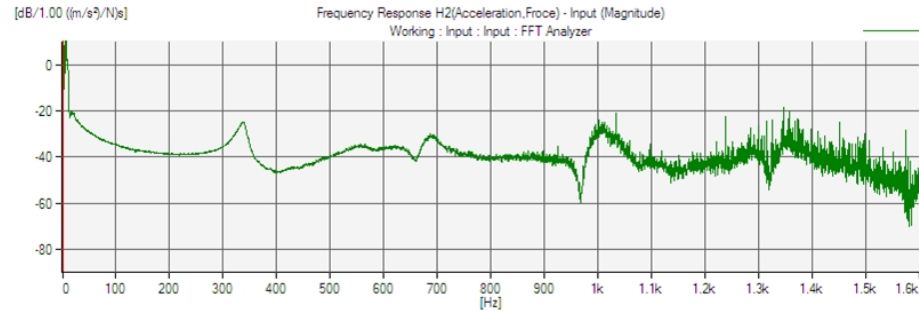


Figure 6.13: The frequency response function of beam L_y

frequencies up to 2 kHz. While for beams L_x and L_y , only a few resonant modes can be registered. The modal loss factors of beams I_x , J_x , I_y and J_y are similar, of the order 1%, as shown in Fig. 6.14. The modal loss factors of beams K_x and K_y are about 2% around 1200 Hz, as shown in Fig. 6.15.

The effects of the mass loading of the accelerometer on the frequency response function were also investigated. Both a laser Doppler vibrometer and an accelerometer were employed to measure the response of a light single-layer beam, $\sim 1.9 \text{ kg/m}^2$. The beam was excited with white noise by a shaker mounted at its center. The length, width and thickness of the

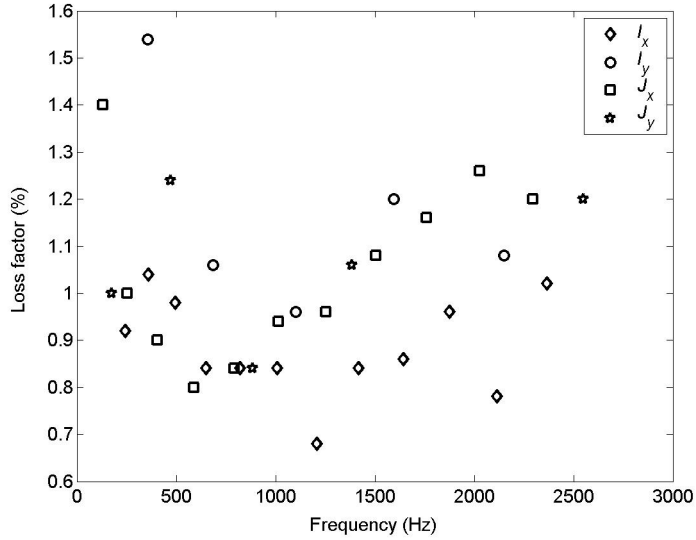


Figure 6.14: Loss factors of beams I_x , I_y , J_x and J_y

beam are 61 cm, 2.54 cm, and 6.35 mm, respectively. The frequency response functions of the beam are shown in Fig. 6.16.

The frequency response functions of the two transducers are seen to be similar. The resonance frequencies measured by the accelerometer are slightly lower than those measured by the laser vibrometer. The laser vibrometer and the accelerometer all require some mass to be attached the beam. The mass of the accelerometer is 0.14 g, while the mass of the metal piece needed for the laser vibrometer measurement is much smaller. There is about 5 dB difference between the measured amplitudes of the two frequency response functions. The modal loss factors were determined by the half-power point method. The resonance frequencies and modal loss factors are given in Table 6.3.

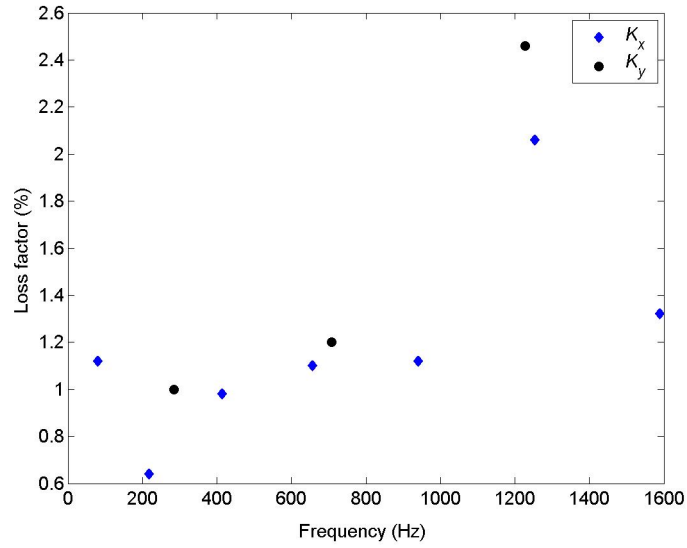


Figure 6.15: Loss factors of beams K_x and K_y

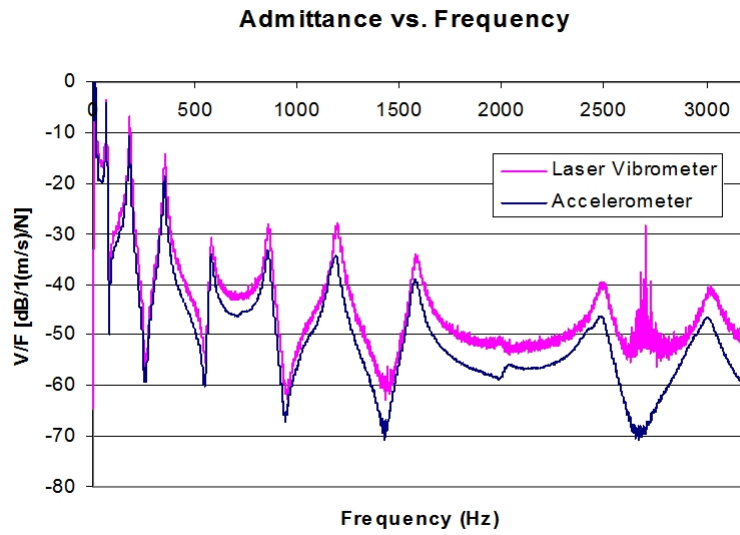


Figure 6.16: The frequency response functions of the aluminum beam

Table 6.3: Resonance frequencies and modal loss factors of the beam

Laser	$f(\text{Hz})$	67	182	352	580	859	1193	1582	2486	3020
vibrometer	$\eta(\%)$	4.2	3.2	2.6	2.7	~ 2.2	~ 1.8	~ 1.9	~ 2.0	~ 2.0
Accelerometer	$f(\text{Hz})$	67	180	350	580	856	1188	1577	2482	3002
	$\eta(\%)$	3.0	2.8	2.6	2.7	2.6	3.5	2.8	3.9	~ 3.1

The effect of mass loading of the accelerometer on the resonance frequencies of the beam was found to be negligible. The resonance frequencies measured by the accelerometer system are all within 1% of those obtained by the laser system. The laser system has more noise than the accelerometer system, and it cannot provide precise resonance frequencies and modal loss factors except at low frequencies.

6.5 Material properties of sandwich panels

The well known sixth-order governing differential equation of transverse displacement for a sandwich beam was originally developed by Mead and Markus for sandwich beams with viscoelastic cores [23]. In general these beams have thin cores, which are different from the sandwich structures examined in this study. Nilsson and Nilsson [37] developed a sixth-order governing equation for symmetric sandwich beams with thick honeycomb and foam cores, which includes rotatory inertia effects of the face sheets and core. They assumed that the total transverse displacement w of a honeycomb sandwich is primarily caused by bending, shear and rotation in the core, as shown in Fig. 6.17.

$$\partial\omega/\partial x = \beta + \gamma. \quad (6.5)$$



Figure 6.17: Transverse displacement caused by (a) bending and (b) shear

The differential equation governing w , β and γ is determined using Hamilton's principle. The total potential energy of a honeycomb sandwich beam is assumed to be caused by pure bending of the entire beam, bending of both face sheets and shear in the core. The kinetic energy of the honeycomb sandwich beam is due to the transverse motion of the beam and the rotation of a section of the beam.

Then the equation governing w can be written as,

$$\begin{aligned}
 -2D_2 \frac{\partial^6 w}{\partial x^6} + \frac{2D_2}{D_1} I_\rho \frac{\partial^6 w}{\partial x^4 \partial t^2} - \left(\mu + \frac{2D_2}{D_1} \mu + \frac{I_\rho G_e h}{D_1} \right) \frac{\partial^4 w}{\partial x^2 \partial t^2} + G_e h \left(\frac{\partial^4 w}{\partial x^4} + \frac{\mu}{D_1} \frac{\partial^2 w}{\partial t^2} \right) \\
 + \frac{I_\rho}{D_1} \mu \frac{\partial^4 w}{\partial t^4} = - \left(1 + \frac{2D_2}{D_1} \right) \frac{\partial^2 q}{\partial x^2} + \frac{G_e h}{D_1} q + \frac{I_\rho}{D_1} \frac{\partial^2 q}{\partial t^2}, \tag{6.6}
 \end{aligned}$$

$$\begin{aligned}
 \text{with } D_1 = \frac{E_2 h^3}{12} + E_1 \left(\frac{h^2 t}{2} + h t^2 + \frac{2t^3}{3} \right), \quad I_\rho = \frac{\rho_c h^3}{12} + \rho_t \left(\frac{h^2 t}{2} + h t^2 + \frac{2t^3}{3} \right) \\
 D_2 = \frac{E_1 t^3}{12}, \quad \mu = 2\rho_t t + \rho_c h, \quad G_e = G_2 \left(1 + \frac{t}{h} \right)^2,
 \end{aligned}$$

where h and t are the thickness of the face sheets and core, respectively. The mass densities of the face sheets and the core are ρ_t and ρ_c , respectively.

Assuming $w = \sum_j A_j e^{i\omega t} e^{-ik_j x}$, and allowing the external load q to equal zero, the wave number k_j must satisfy the following expression,

$$2D_2 k^6 + \left(G_e h - \frac{2D_2}{D_1} I_\rho \omega^2 \right) k^4 - \left(\mu + \frac{2D_2}{D_1} \mu + \frac{I_\rho G_e h}{D_1} \right) k^2 \omega^2 - \frac{\mu G_e h}{D_1} \omega^2 + \frac{I_\rho}{D_1} \mu \omega^4 = 0. \quad (6.7)$$

Nilsson and Nilsson presented the boundary conditions, given in Table 6.4, in terms of w , and β . It was shown that β can be expressed in a similar way to w , $\beta = \sum_j B_j e^{i\omega t} e^{-ik_j x}$, and it must satisfy the following equation,

$$-D_1 \frac{\partial^2 \beta}{\partial x^2} + 2D_2 \left(\frac{\partial^3 w}{\partial x^3} - \frac{\partial^2 \beta}{\partial x^2} \right) + I_\rho \frac{\partial^2 \beta}{\partial t^2} - G_e h \left(\frac{\partial w}{\partial x} - \beta \right) = 0. \quad (6.8)$$

Then the amplitude B_j can be determined as a function of A_j ,

$$B_j = A_j \frac{2D_2 k_j^3 + G_e h k_j}{(D_1 + 2D_2) k_j^2 + G_e h - I_\rho \omega^2} = A_j X_j. \quad (6.9)$$

Since both composite face sheet and core materials have losses, the damping is introduced by a complex E -modulus,

$$E = E_R(1 + i\eta), \text{ where } E_R \text{ is real.} \quad (6.10)$$

Table 6.4: Basic boundary conditions

Clamped	$w = 0$	$\beta = 0$	$\nabla w = 0$
Free	$\nabla^2 w = 0$	$\nabla \beta = 0$	$D_1 \frac{\partial^2 \beta}{\partial x^2} = I_\rho \frac{\partial^2 \beta}{\partial t^2}$

For a free-free boundary sandwich beam, the six boundary conditions in combination with Eq. (6.9), yield the equations for A_j , which written in matrix form are,

$$\begin{bmatrix} b_{11} & b_{12} & b_{13} & b_{14} & b_{15} & b_{16} \\ b_{21} & b_{22} & b_{23} & b_{24} & b_{25} & b_{26} \\ b_{31} & b_{32} & b_{33} & b_{34} & b_{35} & b_{36} \\ b_{41} & b_{42} & b_{43} & b_{44} & b_{45} & b_{46} \\ b_{51} & b_{52} & b_{53} & b_{54} & b_{55} & b_{56} \\ b_{61} & b_{62} & b_{63} & b_{64} & b_{65} & b_{66} \end{bmatrix} \begin{Bmatrix} A_1 \\ A_2 \\ A_3 \\ A_4 \\ A_5 \\ A_6 \end{Bmatrix} = \begin{Bmatrix} 0 \\ 0 \\ 0 \\ 0 \\ 0 \\ 0 \end{Bmatrix}, \quad (6.11)$$

with $b_{1j} = -k_j^2$, $b_{2j} = -ik_j X_j$, $b_{3j} = D_1 X_j k_j^2 - I_\rho X_j \omega^2$, $b_{4j} = -k_j^2 e^{-ik_j L}$,

$$b_{5j} = -ik_j X_j e^{-ik_j L}, \quad b_{6j} = (D_1 X_j k_j^2 - I_\rho X_j \omega^2) e^{-ik_j L}.$$

The material properties of the face sheets and cores of the sandwich structures tested in this study were estimated using Eqs. (6.7) and (6.11), based on the experimental data for free-free sandwich beams. It is well known that the motion of sandwich structures is primarily determined by the face sheets at low frequencies. Thus the E -moduli of the face sheets can be estimated from the first several resonance frequencies. Then the G -moduli of the cores can be estimated from the higher modes. Since only the first few modes can be

Table 6.5: The estimated moduli of sandwich panels I , J , K and L

Sandwich panel		I	J	K	L
Face sheets	E_x (GPa)	32	49	39	32
	E_y (GPa)	34	49	39	24
Cores	G_{xz} (MPa)	100	90	100	
	G_{yz} (MPa)	150	140	60	

identified for beams L_x and L_y , the shear moduli, G_{xz} and G_{yz} , of the core of panel L can't be determined from measurements. The material property parameters were assumed to be constant for all frequencies. Then the estimated main material properties for sandwich panels I , J , K and L are given in Table 6.5.

The resonance frequencies of sandwich beams are insensitive to the core E -modulus perpendicular to the plane, which was assumed to be 2.3 times the stiffer out-of-plane shear modulus of the core. Based on the estimated material properties of the face sheets and the cores, the predicted natural frequencies obtained from the models of Nilsson and Nilsson [37], Mead and Markus [23] (MM), Johnson and Kienholz [48] (FEM) are given in Tables 6.6 ~ 6.11. The FEM model had 60 CQUAD4 plate elements and 60 HEXA solid elements in the lengthwise direction, x -axis. Poisson's ratios were assumed to be 0.15. The off-diagonal stiffness constants C_{13} , C_{23} , and C_{12} were arbitrarily assumed to be equal to 0.1 times the softer of the axial stiffness constants.

The predicted resonance frequencies are seen to agree well with the measured resonance frequencies. The modal frequencies predicted from governing equations, the models of Nilsson and Nilsson, and Mead and Markus, are similar, then the effects of the rotatory inertia of the face sheets and core on modal frequencies are negligible for the sandwich

Table 6.6: The modal frequencies of beam I_x

Mode	1	2	3	4	5	6	7	8	9	10
Nilsson (Hz)	28	77	149	245	361	498	652	823	1009	1208
MM (Hz)	28	76	148	243	359	494	648	819	1004	1203
Johnson (Hz)	28	76	149	243	360	495	650	821	1007	1207
Measured (Hz)	27	74	143	238	353	486	639	808	992	1189
Mode	11	12	13	14	15					
Nilsson (Hz)	1418	1638	1867	2103	2345					
MM (Hz)	1413	1633	1862	2098	2340					
Johnson (Hz)	1419	1642	1875	2116	2366					
Measured (Hz)	1400	1622	1852	2085	2331					

Table 6.7: The modal frequencies of beam I_y

Mode	1	2	3	4	5	6	7
Nilsson (Hz)	133	360	690	1109	1601	2152	2748
MM (Hz)	131	356	684	1100	1591	2141	2738
Johnson (Hz)	131	357	685	1103	1596	2150	2750
Measured (Hz)	126	353	683	1096	1586	2132	2720

Table 6.8: The modal frequencies of beam J_x

Mode	1	2	3	4	5	6	7	8	9	10
Nilsson(Hz)	48	132	253	407	589	794	1017	1254	1501	1755
MM(Hz)	48	130	250	403	584	788	1010	1246	1492	1746
Johnson(Hz)	48	131	252	406	588	793	1016	1254	1504	1761
Measured(Hz)	47	131	251	404	583	781	999	1224	1460	1702
Mode	11	12								
Nilsson (Hz)	2015	2278								
MM (Hz)	2005	2268								
Johnson (Hz)	2026	2296								
Measured (Hz)	1950	2195								

Table 6.9: The modal frequencies of beam J_y

Mode	1	2	3	4	5	6
Nilsson (Hz)	177	474	888	1389	1949	2548
MM (Hz)	176	472	886	1387	1949	2549
Johnson (Hz)	177	472	885	1386	1947	2549
Measured (Hz)	177	467	877	1372	1929	2477

Table 6.10: The modal frequencies of beam K_x

Mode	1	2	3	4	5	6	7	8	9	10
Nilsson (Hz)	81	219	416	661	943	1253	1582	1924	2275	2630
MM (Hz)	80	216	411	655	936	1245	1574	1917	2268	2624
Johnson (Hz)	80	217	413	657	941	1254	1589	1939	2300	2671
Measured (Hz)	79	216	413	651	919	1216	1536	1987	2230	2592

Table 6.11: The modal frequencies of beam K_y

Mode	1	2	3	4	5	6
Nilsson (Hz)	285	707	1218	1759	2300	2845
MM (Hz)	283	704	1216	1758	2305	2847
Johnson (Hz)	284	708	1227	1780	2343	2904
Measured (Hz)	281	702	1227	1757	2277	2727

structures tested in this study. The difference of the predictions between the FEM model and the other two models is larger for thick sandwich beams than for thin sandwich beams.

6.6 Conclusions

The main material moduli of composite sandwich panels have been determined experimentally from data for free-free sandwich beams. The predicted natural frequencies were found to agree well with the measured resonance frequencies. Due to the small mass, 0.14 g, the effect of mass loading of the accelerometer on the measured resonance frequencies of the sandwich beams was found to be negligible. The modal loss factors of the sandwich beams are much higher than that of the aluminum beam, about 10 times.

CHAPTER 7

DYNAMIC PROPERTIES OF COMPOSITE SANDWICH PANELS

7.1 Introduction

The parameters that are used in statistical energy analysis to describe the dynamic behavior of a structure are the modal density, internal loss and coupling loss parameters of the structure. The accuracy prediction of response using SEA greatly depends on an accurate estimate of the three parameters.

In principle the modal density can be obtained by exciting the structure with a sinusoidal force of varying frequency and counting the number of modes that are excited in each frequency band. However, the mode count method is not suitable for structures that have a high modal density and a high modal overlap or those with heavily damped modes present. Because of these reasons, the point mobility technique, described by Cremer *et al.* [42] is a more suitable method for measuring modal densities. The accuracy of this technique is critically dependent on the reliable measurement of force and velocity.

Two common direct experimental techniques for obtaining internal loss factors are 1) the half-power bandwidth method and 2) the envelope decay method. Only the internal loss factors of the non-overlapping modes can be obtained from the half-power bandwidth method. For SEA applications, the primary property of interest is the band-averaged loss factor not the modal loss factor. The envelope decay method is based on the logarithmic

decrement of the transient structural response, which is obtained from measurements of the decay of the vibration after the excitation is cut off. The steady state power flow method is an indirect approach to experimentally obtain the band-averaged loss factor.

Most experiments used to measure the loss factor of a structure have been conducted in air. In such cases, the loss factor reported is the total loss factor, which includes the radiation loss factor.

In this study, modal densities, internal loss factors and radiation loss factors of four composite sandwich panels were estimated experimentally. The dimensions of all four panels are the same, 1.12 m \times 0.62 m. A three-channel spectral analysis was employed to obtain the point mobilities of the sandwich panels. The modal densities of the composite sandwich panels were experimentally determined with the spectral mass correction method. The total loss factors of the panels were evaluated by using the power flow method. The experimental radiation loss factors of the unbaffled and baffled composite sandwich panels were compared with the theoretical estimates.

7.2 Experimental modal densities

The modal density of a structure can be obtained from the measurement of the spatially averaged point mobility frequency response function [42],

$$n(f) = 4M_p \overline{\text{Re}[Y(f)]}, \quad (7.1)$$

where $Y(f) = V(f)/F(f)$ is the driving point mobility of the structure at frequency f , and M_p is the mass of the structure. The band-averaged modal density is given by,

$$n(f) = \frac{1}{\Delta f} \int 4M_p \overline{\text{Re}[Y(f)]} df. \quad (7.2)$$

In the conventional two-channel spectral analysis, the point mobility is determined by the cross-spectrum of the force, and velocity and the auto-spectrum of the input force,

$$Y(f) = \frac{G_{fv}(f)}{G_{ff}(f)}. \quad (7.3)$$

For lightly damped systems, the driving force at resonance is very small, $G_{ff}(f) \rightarrow 0$. Any feedback due to exciter-structure interaction can produce bias error which can sometimes result in negative peaks [55].

In the three-channel spectral analysis, the point mobility is determined by using the relation,

$$Y(f) = \frac{G_{sv}(f)}{G_{sf}(f)}. \quad (7.4)$$

where $G_{sv}(f)$ and $G_{sf}(f)$ are the cross-spectra between the original input and the measured velocity, and the original input and the measured force.

Mass corrections must be considered when making any frequency response measurement on a lightweight structure. In the case of point mobility measurements, there will always be some added mass between the force gauge of the impedance head and the structure. The

added mass will corrupt the force measurement because some portion of the force measured is used to drive against the inertial resistance of the added mass.

The point mobility measurement can be corrected for the mass loading effect as follows,

$$Y_c = \frac{V_m}{F_c} = \frac{V_m}{F_m - MA_m} = \frac{V_m/F_m}{1 - i\omega MV_m/F_m} = \frac{Y_m}{1 - i\omega MY_m}, \quad (7.5)$$

where A_m and F_m are the acceleration and force measured by the impedance head, V_m and Y_m are the measured velocity and point mobility, F_c and Y_c are the corrected force and point mobility, respectively. M is the added mass between the force gauge and the structure.

The added mass M can be evaluated by adding the manufacturer's specifications for the mass below the force gauge to the mass of the attachment components or by measuring the point mobility of the added mass attached to the impedance head when it is separated from the structure. The first correction method is termed as the measured mass method. The second correction method is termed as the spectral mass method.

Hence, the real and imaginary parts of the corrected point mobility are,

$$\text{Re}(Y_c) = \frac{\text{Re}(Y_m)}{[1 + \omega M \text{Im}(Y_m)]^2 + [\omega M \text{Re}(Y_m)]^2}, \quad (7.6)$$

$$\text{Im}(Y_c) = \frac{\omega M \{[\text{Im}(Y_m)]^2 + [\text{Re}(Y_m)]^2\} + \text{Im}(Y_m)}{[1 + \omega M \text{Im}(Y_m)]^2 + [\omega M \text{Re}(Y_m)]^2}. \quad (7.7)$$

In this study, the modal density of a sandwich panel was obtained by averaging the modal densities measured at four randomly chosen points on the panel. The point mobility



Figure 7.1: Set-up for the modal density and loss factor experiments

was measured at each position with a B&K impedance head type 8000 that was attached to a B&K vibration exciter type 4809 by a stud. The impedance head was attached to the panel with wax. The sandwich panel was suspended by strings and excited by a conventional electrodynamic shaker with a broadband random force, as shown in Fig. 7.1. The measured inertance of the added mass between the force gauge and the panel is between $860 \text{ (m/s}^2\text{)}/\text{N}$ and $960 \text{ (m/s}^2\text{)}/\text{N}$ in the frequency range of $200 \text{ Hz} \sim 5600 \text{ Hz}$, as shown in Fig. 7.2. Then the effective dynamic mass of the added mass is between 1.06 g and 1.14 g , which is slightly smaller than 1.2 g , the mass below the force gauge of the impedance head specified by the manufacturer.

The frequency analysis bandwidths chosen were one-third octave and a constant bandwidth of 400 Hz . The first is consistent with most previous work and the second is chosen to have at least five resonance frequencies in each analysis band. The frequency analysis

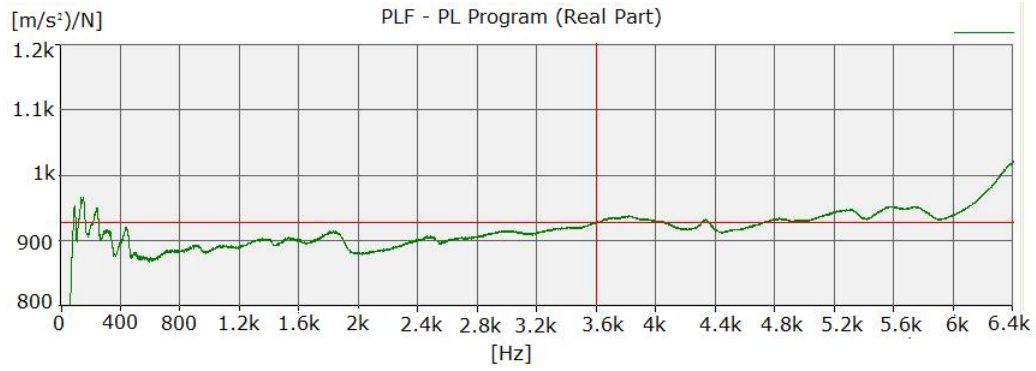


Figure 7.2: The inertance of the added mass

resolution was chosen to be 1 Hz. Four composite sandwich panels with foam-filled honeycomb cores, panels $I \sim L$, were investigated. The dimensions of the four panels are given in Table 6.2.

The measured point mobility of panel J at one location using the three-channel spectral analysis is illustrated in Fig. 7.3. It was found that only slight differences between the measured point mobilities of all four panels obtained by the two-channel and three-channel spectral analyses exist at very low frequencies.

The modal density estimates without mass correction, as shown in Fig. 7.4, only provide a reasonable approximation at low frequencies, where the effect of the added mass is negligible. The theoretical modal density predictions were derived for simply supported panels. The theoretical predictions were obtained from 1) Mead and Markus's sixth-order governing equation by following the procedure that is described in Sec. 4.4, and 2) a reduced

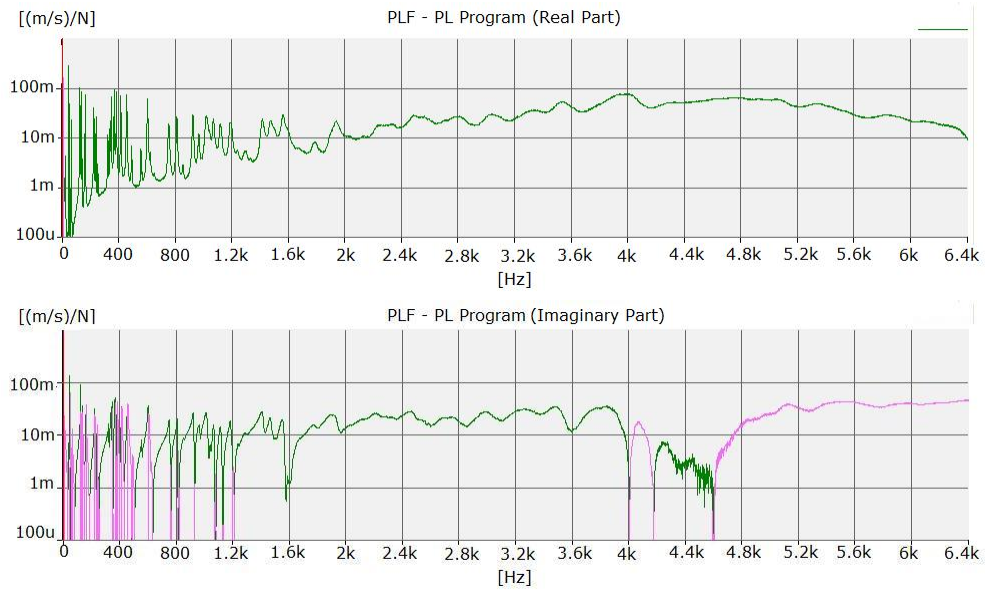


Figure 7.3: The measured point mobility of panel J using the three-channel spectral analysis (a) real part (b) imaginary part

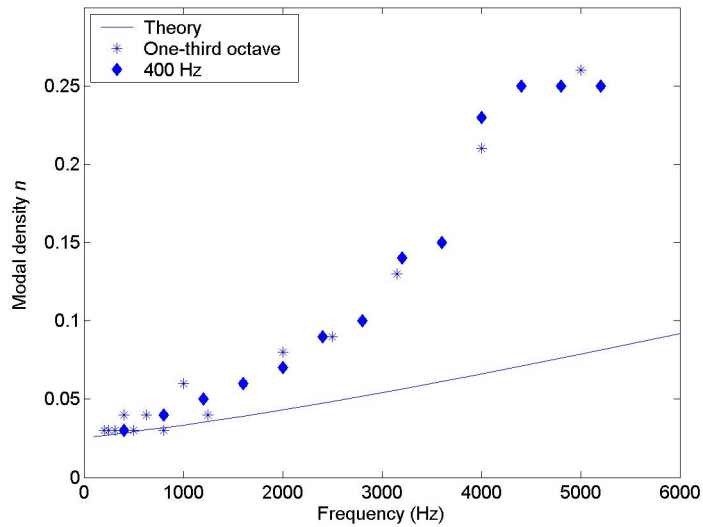


Figure 7.4: Modal density estimates for panel J without mass correction

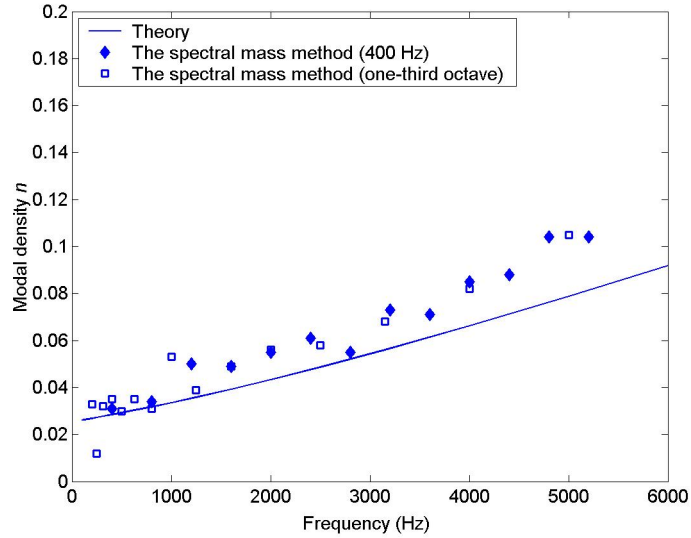


Figure 7.5: Modal density estimates for panel J with mass correction

fourth-order governing equation, by use of Eq. (4.22). It was found that both equations produce the same modal density values for all four panels at frequencies below 6000 Hz.

The modal density estimates for panel J with mass correction, agree with the theoretical predictions as shown in Fig. 7.5. The modal density estimates for the other panels, I , K and L are shown in Figs. 7.6 ~ 7.8.

Since Mead and Markus's sixth-order governing equation was developed for sandwich beams or isotropic sandwich panels, and panels J and K have similar stiffness constants along the two main in-plane directions, as shown in Table 6.5, then the modal density estimates for these two panels are closer to the theoretical predictions than those for panel I are. The core shear modulus of panel L could not be determined from the resonance measurements. So the theoretical modal density predictions were computed by assuming

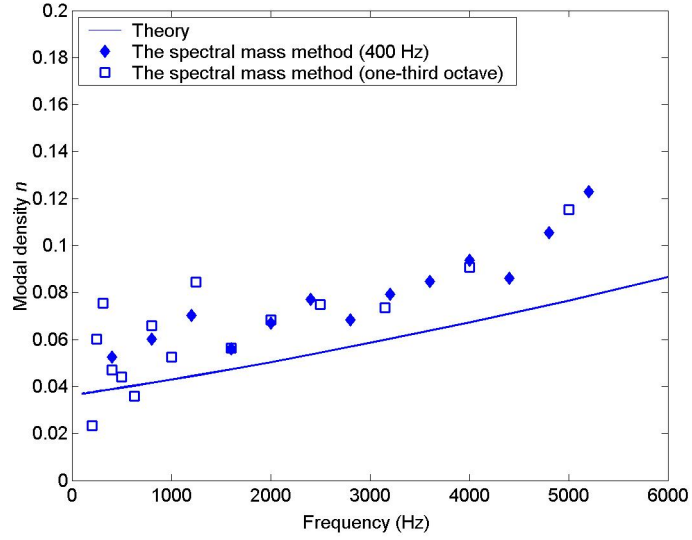


Figure 7.6: Modal density estimates for panel *I* with mass correction

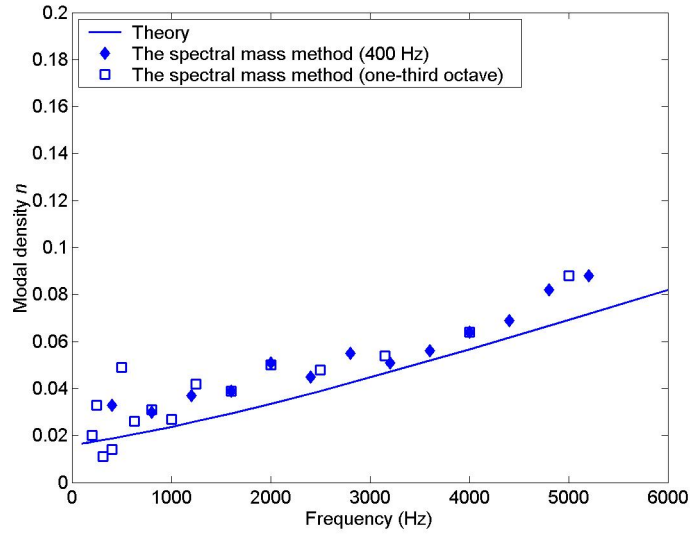


Figure 7.7: Modal density estimates for panel *K* with mass correction

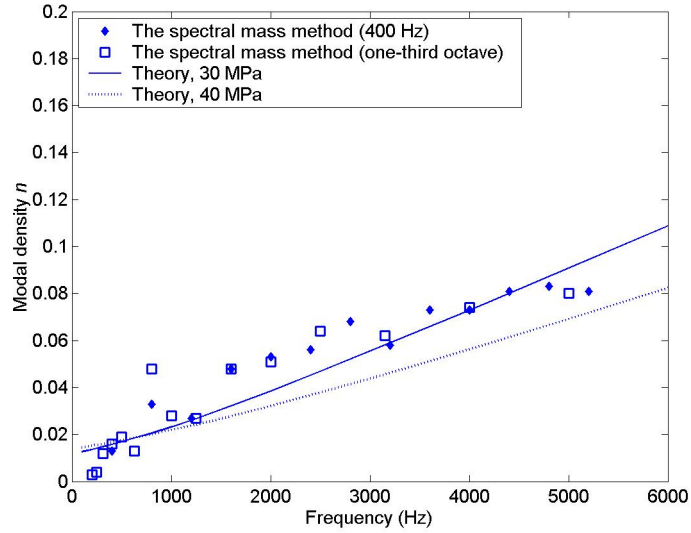


Figure 7.8: Modal density estimates for panel L with mass correction

that the equivalent shear moduli are 30 MPa and 40 MPa, respectively. The theoretical values imply that the modal density of panel L is insensitive to the core shear moduli at frequencies below 1000 Hz.

7.3 Experimental total loss factors

Unlike modal densities, theoretical expressions for loss factors of structures are not available. The loss factor of a structure can be obtained from the measurement of the force supplied to the structure and the spatially averaged square velocity produced. In steady state conditions, the average power input is equal to the average power dissipated, and then

the average loss factor is,

$$\eta = \frac{\overline{F^2(t)}\text{Re}(Y)}{M_p\langle v^2(t)\rangle 2\pi f}. \quad (7.8)$$

Thus the band-averaged loss factor is,

$$\eta(f) = \frac{1}{\Delta f} \int \frac{\overline{F^2(t)}\text{Re}(Y)}{M_p\langle v^2(t)\rangle 2\pi f} df. \quad (7.9)$$

As discussed in the previous section, the force measurement can be mass corrected as follows,

$$F_c = F_m - M A_m = F_m - i\omega M Y_c F_c \Rightarrow F_c = \frac{F_m}{1 + i\omega M Y_c}, \quad (7.10)$$

then,
$$\overline{F_c^2} = \frac{\overline{F_m^2}}{[1 - \omega M \text{Im}(Y_c)]^2 + [\omega M \text{Re}(Y_c)]^2}. \quad (7.11)$$

In the case of the measurement of high frequency vibration of lightly damped structures, considerable care should be taken when using an accelerometer because of the mass loading effect. Well below its resonance frequency, the accelerometer can be assumed to act as a pure mass. The velocity of the structure V_c can be assumed to be reduced to V_a by the presence of the accelerometer [56],

$$\frac{V_a}{V_c} = \frac{Z}{Z + i\omega m_a}, \quad (7.12)$$

where Z is the mechanical impedance of the test element, and m_a is the accelerometer mass.

In this study, the mass loading of the accelerometer was assumed to be,

$$\frac{V_a^2}{V_c^2} = \frac{1}{1 + [\omega m_a \text{Re}(\overline{Y}_c)]^2}, \quad (7.13)$$

where \overline{Y}_c is the corrected point mobility. The corrected point mobility in the loss factor analysis is the estimate obtained from the spectral mass correction method.

The frequency bandwidth of the loss factor analysis chosen was one-third octave. The frequency analysis resolution was 1 Hz. The velocities of the panels were determined by measuring the panel responses with an Endevco model 2226c piezoelectric accelerometer at five randomly chosen positions. The loss factor estimates for panel J are shown in Fig. 7.9.

The mass loading effect becomes apparent at frequencies above 3150 Hz for panel J . It was found that the corrected loss factor of panel J is less than 3%. The modal loss factors of panel J , obtained from the half-power point method are given in Table 7.1. The loss factor estimates are in good agreement with the modal loss factors.

Table 7.1: The modal loss factors of panel J

Frequency (Hz)	161	222	238	320	336	366	382	412	454	490	554	601
Loss factor η (%)	0.7	0.8	0.7	1.6	0.6	0.5	0.6	0.6	0.7	0.7	0.6	0.9

The loss factor estimates for panels I , K and L are shown in Figs. 7.10 ~ 7.12. It was found that the loss factor of panel L is much higher than those of the three other panels. The effect of the mass loading of the accelerometer is small at frequencies below 2000 Hz for all four panels.

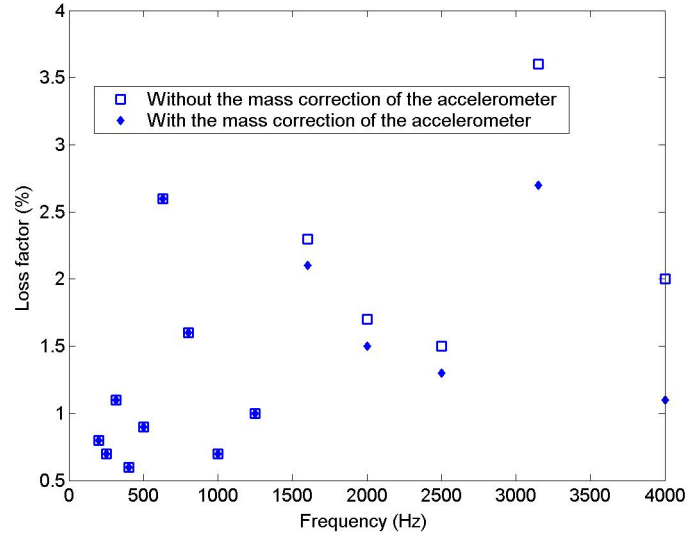


Figure 7.9: Loss factor estimates for panel *J*

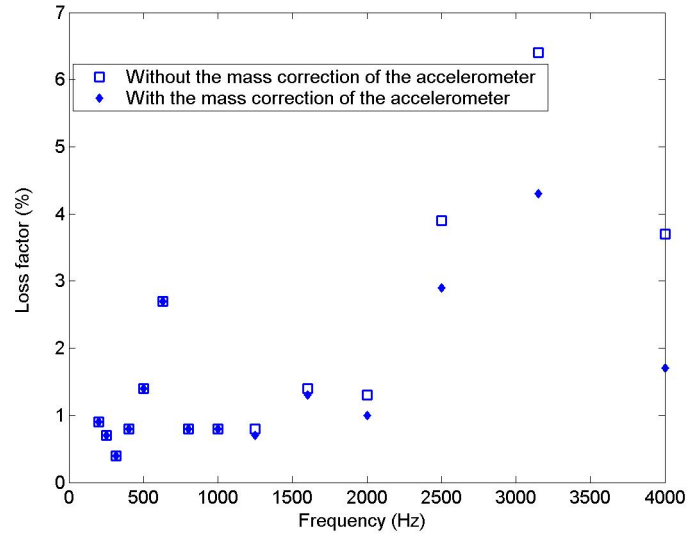


Figure 7.10: Loss factor estimates for panel *I*

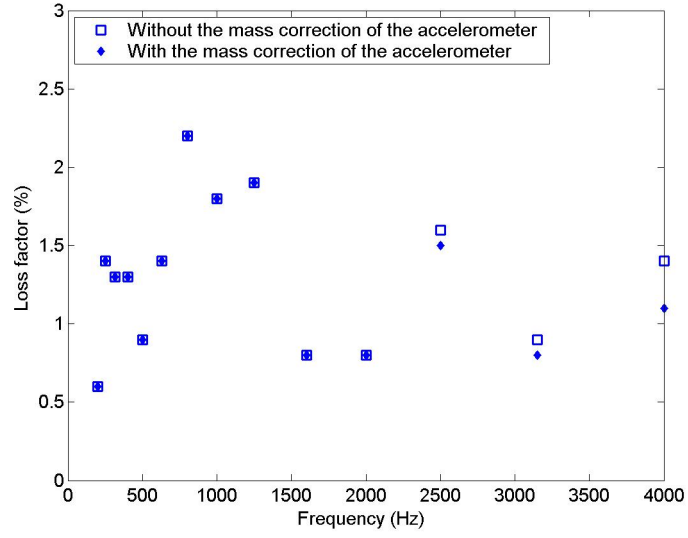


Figure 7.11: Loss factor estimates for panel K

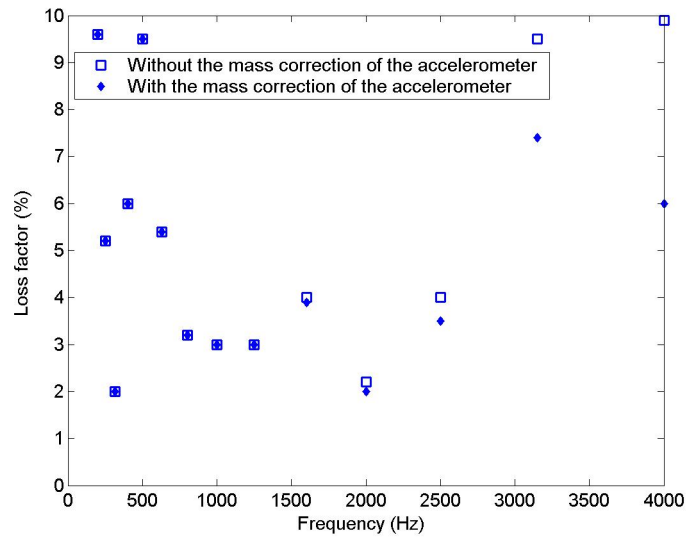


Figure 7.12: Loss factor estimates for panel L

7.4 Experimental radiation loss factors

The radiation resistance of a structure in a reverberant field can be experimentally obtained by studying the energy flow relations between the structure and the reverberation room [13]. Consider a panel that is excited by a shaker in a reverberation room. The steady state power flow balance equations are,

$$\Pi_{\text{in}1} = \Pi_{\text{diss}1} + \Pi_{12}, \quad 0 = \Pi_{\text{diss}2} - \Pi_{12}. \quad (7.14)$$

The total power supplied to the panel by the shaker is,

$$\Pi_{\text{in}1} = R_{\text{tot}} \langle v^2 \rangle = R_{\text{tot}} \frac{E_1}{M_p} = (R_{\text{int}} + R_{\text{rad}}) \langle v^2 \rangle, \quad (7.15)$$

where R_{tot} , R_{rad} and R_{int} are the total, radiation and mechanical resistances of the panel, respectively. M_p is the mass of the panel and $\langle v^2 \rangle$ is the mean square velocity of the structure. The power dissipated by the structure is,

$$\Pi_{\text{diss}1} = R_{\text{int}} \frac{E_1}{M_p} = R_{\text{int}} \langle v^2 \rangle. \quad (7.16)$$

The rate of internal energy dissipation by the reverberation room is,

$$\Pi_{\text{diss}2} = E_2 \eta_{\text{room}} \omega = \eta_{\text{room}} \omega \frac{\langle p^2 \rangle}{\rho c^2} V_{\text{room}}, \quad (7.17)$$

where η_{room} and V_{room} are the internal loss factor and the volume of the room, respectively. $\langle p^2 \rangle$ is the mean square pressure of the room.

Substitution of Eqs. (7.15) ~ (7.17) into (7.14), yields

$$R_{\text{rad}} \langle v^2 \rangle = \eta_{\text{room}} \omega \frac{\langle p^2 \rangle}{\rho c^2} V_2. \quad (7.18)$$

The equation above can be rewritten as,

$$R_{\text{rad}} = \eta_{\text{room}} \omega \frac{S_p}{S_v \rho c^2} V_{\text{room}} = \frac{13.8 S_p}{T_{\text{room}} S_v \rho c^2} V_{\text{room}}, \quad (7.19)$$

where S_p is the pressure spectral density function of the room, S_v is the velocity spectral density function of the structure, and T_{room} is the reverberation time of the room.

Similarly, the radiation resistance of structures excited by a shaker between two reverberation rooms can be estimated experimentally [18]. The steady state power flow balance equations are,

$$0 = \Pi_{\text{diss1}} + \Pi_{12} + \Pi_{13}, \quad \Pi_{\text{in2}} = \Pi_{\text{diss2}} - \Pi_{12} + \Pi_{23}, \quad 0 = \Pi_{\text{diss3}} - \Pi_{13} - \Pi_{23}. \quad (7.20)$$

Then, we have

$$\Pi_{\text{in2}} - \Pi_{\text{diss2}} = \Pi_{\text{diss1}} + \Pi_{\text{diss3}} = R_{\text{rad}} \langle v^2 \rangle = \frac{\omega}{\rho c^2} (\eta_1 \langle p_1^2 \rangle V_1 + \eta_3 \langle p_3^2 \rangle V_3). \quad (7.21)$$

Likewise, the radiation resistance of the structure between two reverberation rooms is,

$$R_{\text{rad}} = \frac{13.8}{S_v \rho c^2} \left(\frac{S_{p1}}{T_1} V_1 + \frac{S_{p3}}{T_3} V_3 \right). \quad (7.22)$$

It is noted that in both radiation resistance determinations, Eqs. (7.19) and (7.22), the radiation resistance is also termed as $R_{\text{rad}}^{4\pi}$, because that the radiating area of the panel is twice of the area of the panel.

Gomperts [58] showed that the radiation efficiency of a baffled free-edge panel at frequencies well below the critical frequency is,

$$\sigma_{\text{baf, free}} = (2/5)(f/f_c)^2 \sigma_{\text{baf, ss}} = (2/5)(f/f_c)^2 (\sigma_{\text{corner}} + \sigma_{\text{edge}}), \quad (7.23)$$

where f_c is the critical frequency of the panel. σ_{corner} and σ_{edge} are the radiation efficiencies of baffled simply supported panel for corner and edge modes, which were derived by Maidanik [13] (see Eq. (4.42)).

When the panel is unbaffled, fluid flow around the panel edges reduces the sound radiation. Oppenheimer and Dubowsky [25] have provided an expression for the radiation efficiency for unbaffled simply supported panels,

$$\sigma_{\text{unbaf, ss}} = F_{\text{plate}} (F_{\text{corner}} \sigma_{\text{corner}} + F_{\text{edge}} \sigma_{\text{edge}}), \quad f < f_c, \quad (7.24)$$

$$\text{with } F_{\text{corner}} = \frac{13\alpha}{2(1+13\alpha)}, F_{\text{edge}} = \frac{49\alpha}{2(1+49\alpha)}, F_{\text{plate}} = \frac{k^4 A_p^2 / 48\pi^2}{1 + k^4 A_p^2 / 48\pi^2},$$

where k is the wave number of the sound in air.

In this study, the four sandwich panels were clamped sequentially between two reverberation rooms and excited by a B&K vibration exciter type 4809 to obtain their radiation resistances. The clamping reduced the dimensions of the panels to 0.88 m \times 0.42 m. The frequency analysis bandwidth chosen was one-third octave. The frequency analysis resolution was 1 Hz. The sound pressure spectral density function in each room was determined by measuring the room responses with a microphone at eight positions. The velocity spectral density function of the panel was determined by measuring the panel responses at eight positions with an accelerometer. The mass loading of the accelerometer was considered in the radiation resistance calculation. The measured radiation resistances of the four clamped sandwich panels are shown in Figs. 7.13 \sim 7.16.

It was found that Eq. (4.42) provides a good approximation for the radiation resistance of the thin sandwich panels, I and J . The measured radiation resistances of the thick sandwich panels, K and L , have maximum values at frequencies above their predicted critical frequencies and are much smaller than those predicted values at frequencies near their predicted critical frequency. Those may be explained by the fact that there are not enough resonant modes below the critical frequency because of the relative small dimensions of the two sandwich panels.

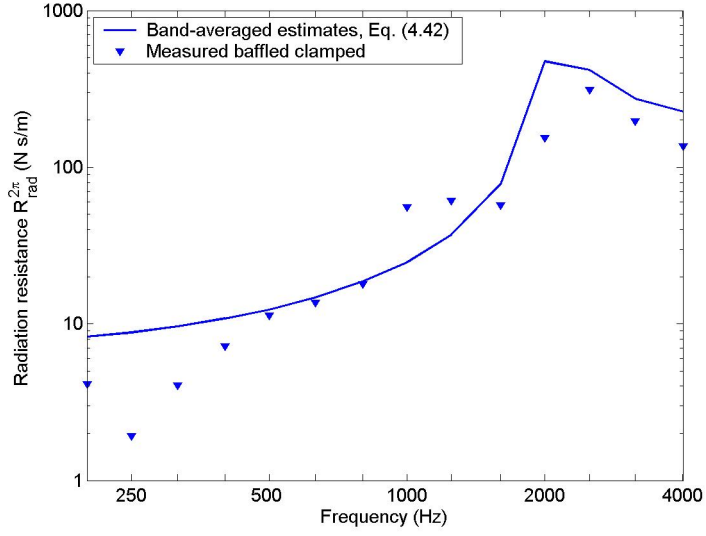


Figure 7.13: Radiation resistance estimates for baffled clamped panel *I*

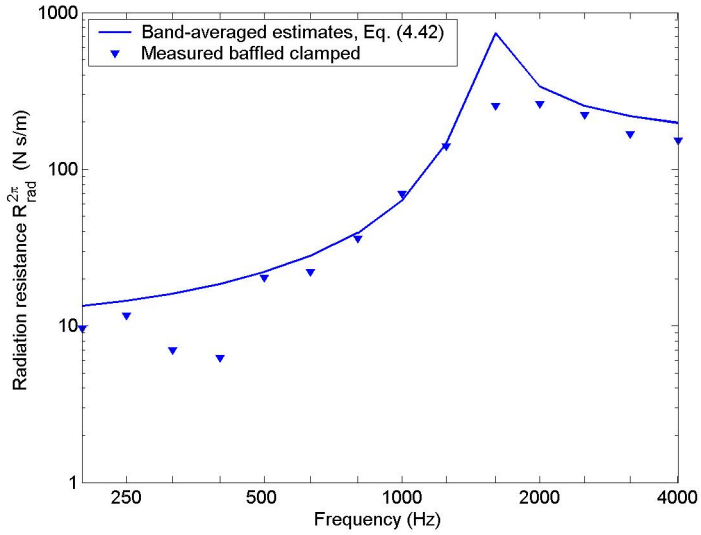


Figure 7.14: Radiation resistance estimates for baffled clamped panel *J*

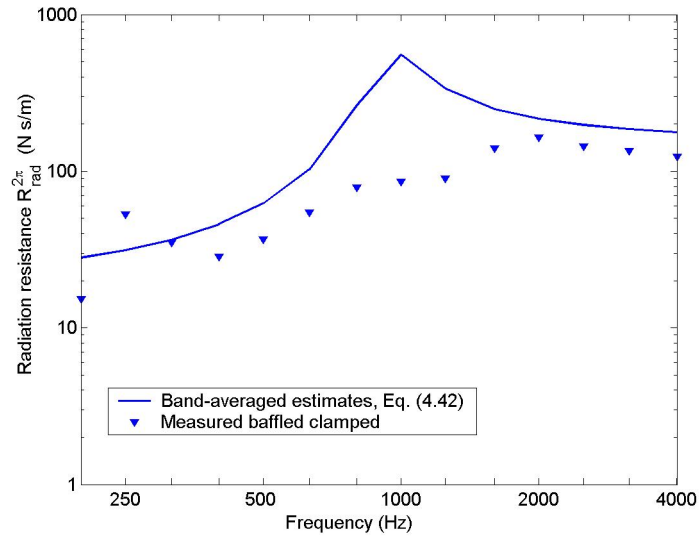


Figure 7.15: Radiation resistance estimates for baffled clamped panel K

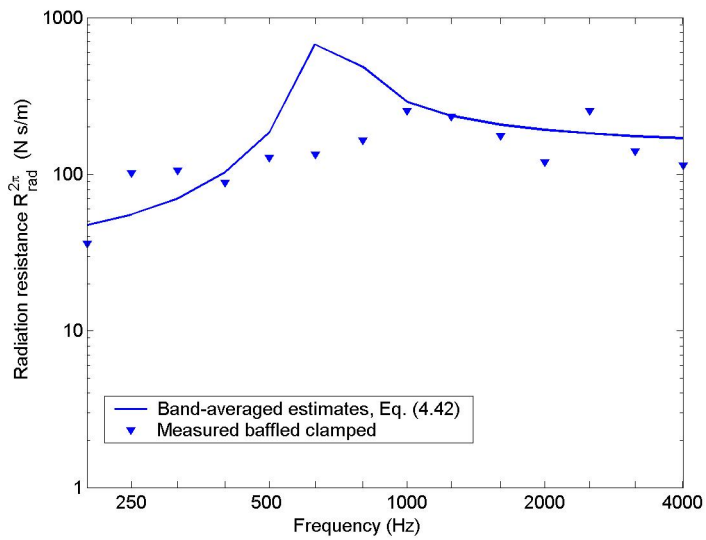


Figure 7.16: Radiation resistance estimates for baffled clamped panel L

The radiation loss factor is determined from the radiation resistance $R_{\text{rad}}^{2\pi}$ by,

$$\eta_{\text{rad}} = \frac{R_{\text{rad}}^{2\pi}}{\omega M_p}. \quad (7.25)$$

The radiation loss factor estimates for panels $I \sim L$ with clamped edges are shown in Fig. 7.17. The radiation loss factors of panels I and J are small at low frequencies, and the maximum values exist near their critical frequencies, more than 2%. The radiation loss factors of panels K and L , however, are high at low frequencies. The radiation loss factor of panel L is significantly larger than those of other panels at frequencies below 1000 Hz.

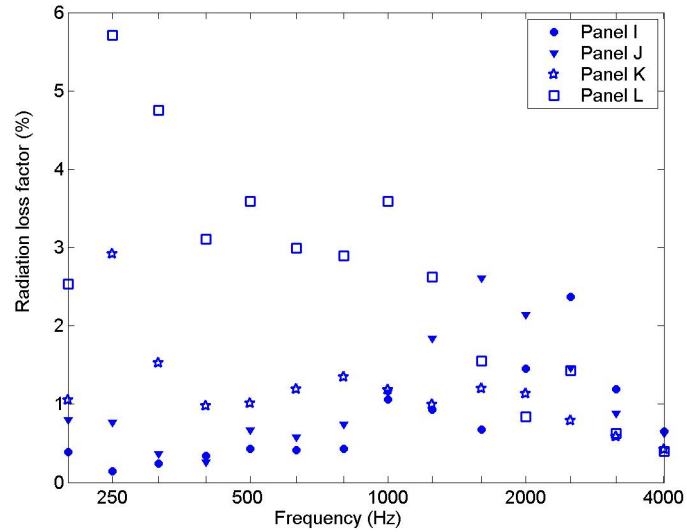


Figure 7.17: Radiation loss factor estimates for clamped panels $I \sim L$

The radiation resistances of panels $I \sim L$ with unbaffled free edges were also investigated. The panels were hung in a reverberation room. The experimental data were obtained

by following the same procedure for the baffled clamped model described early in this section, as shown in Figs. 7.18 ~ 7.21. The radiation resistances of the baffled free-edge panels and the unbaffled simply supported panels were calculated by using Eqs. (7.23) and (7.24).

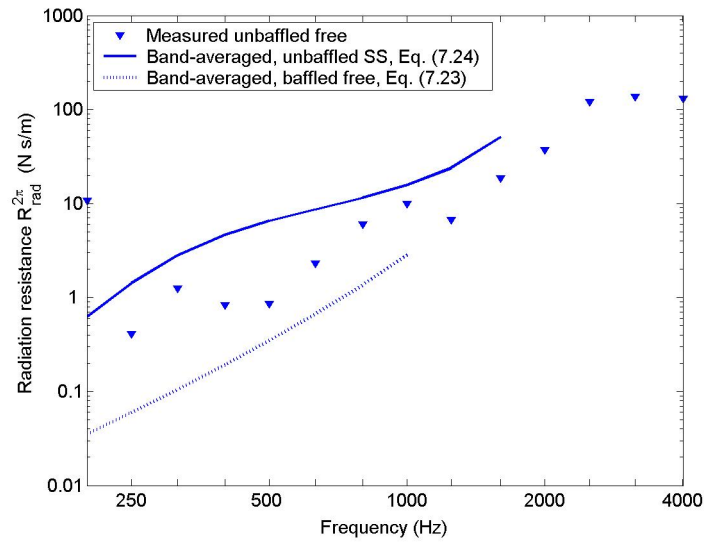


Figure 7.18: Radiation resistance estimates for unbaffled free-edge panel I

The radiation loss factor estimates for unbaffled free-edge panels are shown in Fig. 7.22. The radiation loss factor estimates for all four unbaffled free-edge panels are small at low frequencies, and become larger around their critical frequencies. The radiation loss factor estimates for all four unbaffled free-edge panels are less than 1%, much lower than those of baffled clamped panels.

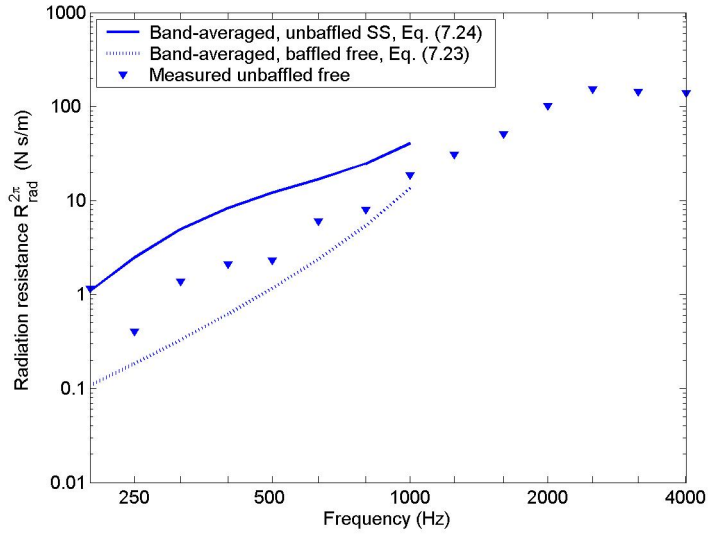


Figure 7.19: Radiation resistance estimates for un baffled free-edge panel *J*

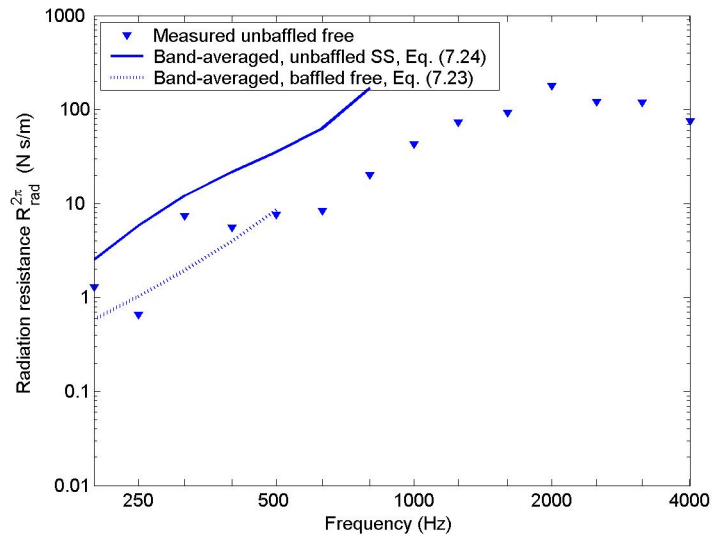


Figure 7.20: Radiation resistance estimates for un baffled free-edge panel *K*

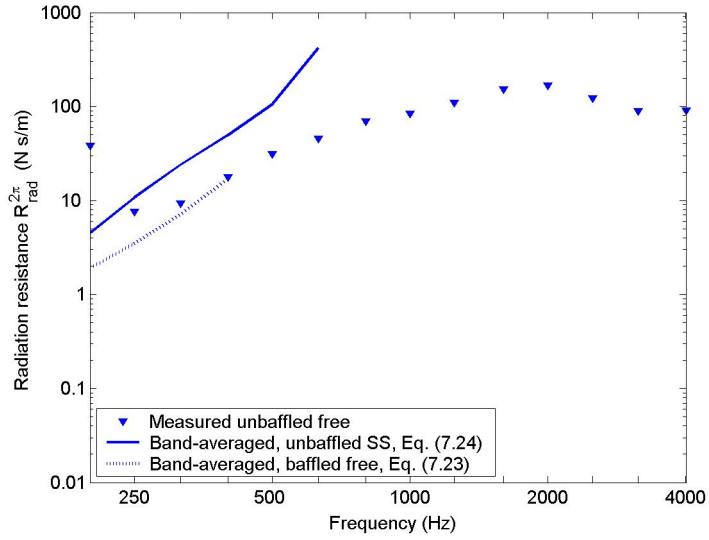


Figure 7.21: Radiation resistance estimates for un baffled free-edge panel L

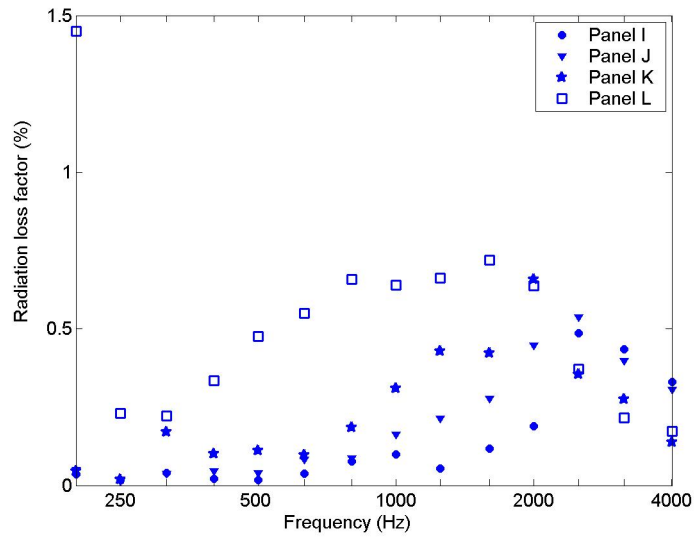


Figure 7.22: Radiation loss factor estimates for un baffled free-edge panels $I \sim L$

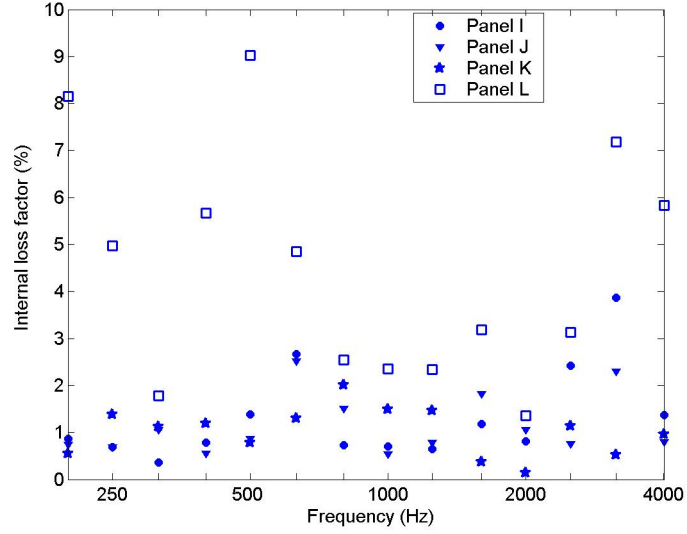


Figure 7.23: Internal loss factor estimates for panels $I \sim L$

7.5 Experimental internal loss factors

In the presence of a fluid medium, such as air, the experimental internal loss factor of a structure obtained from energy methods is the sum of three forms of damping [43],

$$\eta = \eta_{\text{int}} + \eta_{\text{rad}} + \eta_j, \quad (7.26)$$

where η_{int} is the internal loss factor, η_{rad} is the radiation loss factor, and η_j is the loss factor associated with energy dissipation at the boundaries of the structural element.

The internal loss factor estimates for the four panels, $I \sim L$, were obtained by neglecting η_j , as shown in Fig. 7.23. Since the total loss factor is for the un baffled free-edge panel, η_{rad} is used for the radiation loss factor of the un baffled free-edge panel in the computation

of the internal loss factor. The internal loss factors of panels I , J and K are similar, and less than 4%, in the frequency range of 200 Hz \sim 4000 Hz. The internal loss factor of panel L is much greater than those of other panels.

7.6 Conclusions

The experimental modal densities of composite sandwich panels are in good agreement with theory. The radiation loss factors of unbaffled free-edge composite sandwich panels are relatively small, and the total loss factors of unbaffled free-edge composite sandwich panels are dominated by the internal loss factors. On the other hand, the radiation loss factors of baffled clamped composite sandwich panels were found to be comparable to the internal loss factors near their critical frequencies, especially for thin the panels. Among the composite sandwich panels investigated, panels I , J and K have the similar internal loss factors.

CHAPTER 8

SOUND TRANSMISSION LOSS OF COMPOSITE SANDWICH PANELS

8.1 Introduction

Light composite sandwich panels are used in a wide variety of applications, including flooring of commercial aircraft. These panels typically feature orthotropic honeycomb cores bonded to high modulus composite face sheets. The sound transmission characteristics of these structures are important aspects of their design. Because the panels are stiff and light, the acoustical performance is poor. Moore and Lyon [6] developed a wave impedance analysis for sandwich panels with honeycomb cores, and their measured sound transmission loss results are in agreement with the predicted values at frequencies above coincidence. Some researchers experimentally investigated the sound transmission characteristics of honeycomb sandwich panels [10, 59, 60].

The sound transmission loss values of the four composite sandwich panels, $I \sim L$, were determined experimentally by using the conventional two-room method. The predictions of sound transmission loss were calculated from three analyses, wave impedance analysis, statistical energy analysis, and boundary element analysis. The values of loss factors used in the calculations were assumed based on the experimental values, given in Chap. 7.

8.2 Experimental sound transmission loss

Four composite sandwich panels were fabricated for sound transmission loss measurements in the Sound and Vibration Laboratory at Auburn University. The transmission suite consists of two adjacent 51.2 m³ reverberation rooms. Each room has two walls made of wood with fiberglass filled in between them, and they are separated from each other by fiberglass, and mounted on air bags. The panels were clamped in a frame between the two rooms. The panel edge conditions were intended to be fully fixed. The frame reduced the test dimensions of the panels to 0.84 m × 0.42 m. The sound transmission loss was measured according to the standard test method, ASTM E90-99. One-third octave bands of white noise were made in the source room with two loudspeakers and the sound pressure levels were measured at eight positions in each room.

The sound transmission loss for the two-room method discussed in Sec. 4.7, Eq. (4.53), can be expressed as,

$$\text{TL} = L_1 - L_3 + 10 \log_{10} \frac{A_p T}{0.161 V_3}, \quad \text{with } T = \frac{0.161 V_3}{\tau A_p + S_3 \alpha_3}, \quad (8.1)$$

where L_1 and L_3 are the space-averaged sound pressure levels measured in the two reverberation rooms, respectively; S_3 is the total surface area of the receiving room and α_3 is the average absorption coefficient in the receiving room; T is the reverberation time of the receiving room when the panel is clamped between the two rooms; V_3 is the volume of the receiving room; and A_p is the test area of the panel.

Table 8.1: The reverberation times of the receiving room

One-third octave center Frequency (Hz)	Reverberation time T (s)			
	Panel I	Panel J	Panel K	Panel L
125	0.493	0.395	0.352	0.360
160	0.636	0.659	0.699	0.634
200	0.578	0.740	0.736	0.698
250	0.903	0.818	0.856	0.860
315	1.048	1.086	1.034	1.043
400	1.240	1.162	1.155	1.110
500	1.264	1.254	1.309	1.345
630	1.316	1.407	1.324	1.344
800	1.411	1.449	1.472	1.430
1000	1.326	1.364	1.368	1.338
1250	1.238	1.248	1.224	1.247
1600	1.132	1.157	1.121	1.146
2000	1.028	1.036	1.016	1.016
2500	0.947	0.916	0.947	0.937
3150	0.846	0.809	0.865	0.830
4000	0.778	0.759	0.780	0.747
5000	0.698	0.688	0.690	0.713
6300	0.633	0.639	0.629	0.652
8000	0.556	0.545	0.555	0.538

The reverberation times of the receiving room when the four panels were clamped between the two rooms are given in Table 8.1. The reverberation time T was obtained by averaging the reverberation times at eight randomly chosen positions. There is no significant difference among the reverberation times because of the relatively small test area of the panels.

The experimental transmission loss values of all four panels $I \sim L$ are shown in Figs. 8.1 \sim 8.4. The first resonance frequencies of panels I , J , K and L are in the one-third octave bands with center frequencies of 160 Hz, 250 Hz, 315 Hz and 400 Hz, respectively. The experimental transmission loss values of panels I and J are near the field incidence

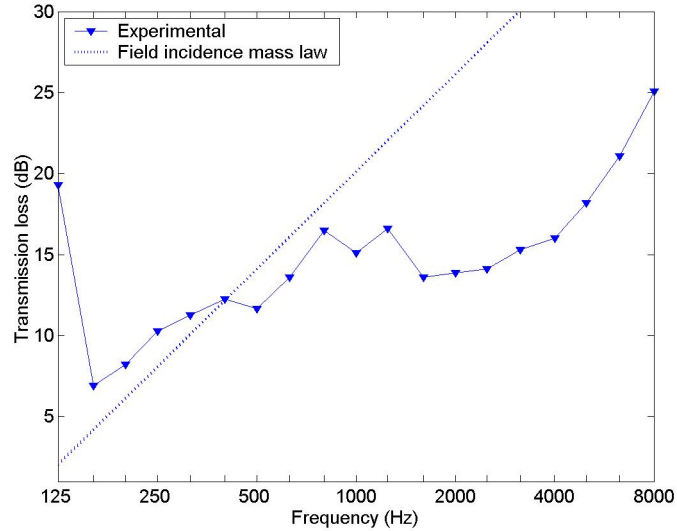


Figure 8.1: Experimental sound transmission loss values of panel *I*

mass law curves at frequencies well below the critical frequencies, while those of panels *K* and *L* are quite below the field incidence mass law curves. At low frequencies, the sound transmission loss curve of panel *K* is strongly influenced by its resonant modes, while the sound transmission loss curve of panel *L* is smoother because of its high loss factor. The coincidence dips of all four panels are not as apparent as those of metal panels. All coincidence dips do not return rapidly towards the mass law curves and the experimental transmission loss values depart from the mass law curves by about 10 dB.

8.3 Sound transmission loss from wave impedance analysis

The predictions of sound transmission loss were generated by using the wave impedance analysis model presented in Chap. 3. In the low frequency region, the transverse motion is

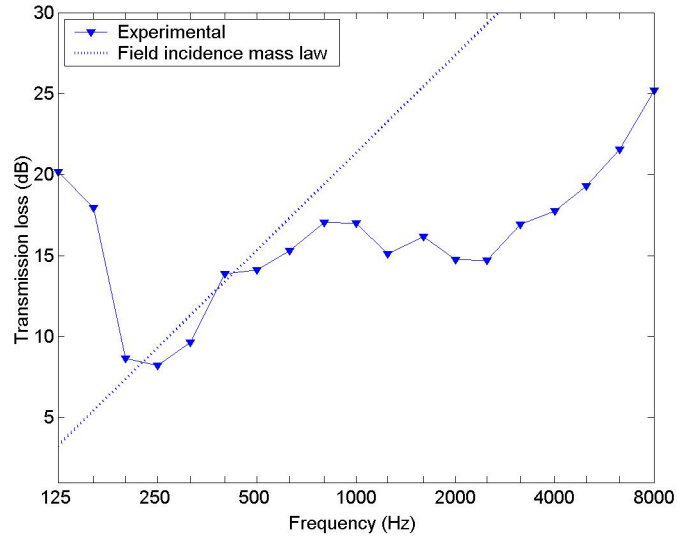


Figure 8.2: Experimental sound transmission loss values of panel J

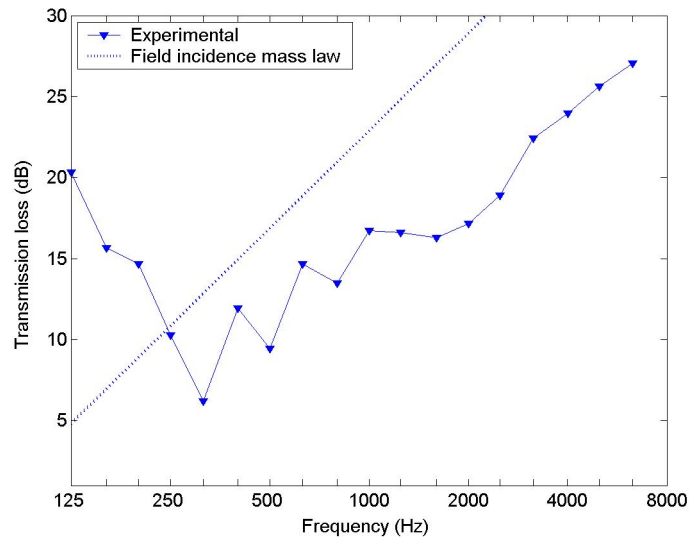


Figure 8.3: Experimental sound transmission loss values of panel K

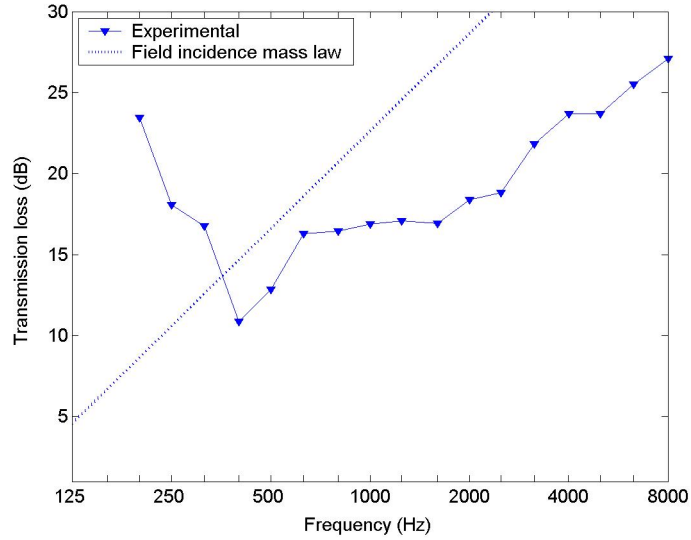


Figure 8.4: Experimental sound transmission loss values of panel L

Table 8.2: The assumed loss factors of the four panels

	Panel I	Panel J	Panel K	Panel L
Face sheets	0.01	0.01	0.01	0.02
Core	0.01, 0.04	0.01, 0.03	0.02, 0.04	0.03, 0.06

determined by pure bending, then the total losses are mostly determined by the losses of the face sheets. For increasing frequencies, the transverse motion of the panel is influenced by the shear in the core. Since both the face sheets and cores of the panels are made of composite materials, the losses of both the face sheets and core were considered in the theoretical calculations. The loss factors of the face sheets and the core of the four panels were assumed based on the results presented in Sec. 7.5, given in Table 8.2. The assumed properties of the four panels are given in Tables 6.2 and 6.5.

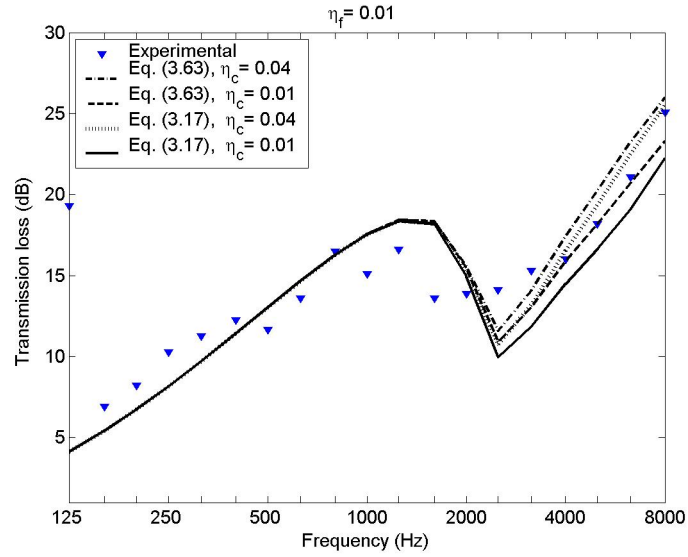


Figure 8.5: Predicted sound transmission loss values of panel I from the wave impedance analysis

All four panels under investigation are symmetric, having two identical face sheets. Then the anti-symmetric and symmetric motions of the panels are uncoupled naturally. The coincidence frequencies associated with symmetric motion of all four panels were found to occur at very high frequencies, above 8 kHz, according to the governing equations for symmetric motion of symmetric sandwich panels, Eq. (3.44). As shown in Chap. 3, the equation given by Mead and Markus [23], Eq. (3.63), is a simplified form for the governing equation developed in Chap. 3, Eq. (3.17), by neglecting symmetric motions. It is expected that the predictions by using the wave impedances calculated from the two equations should be similar at frequencies below 8 kHz. The predicted sound transmission loss values of panels $I \sim L$ obtained by using the two governing equations are shown in Figs. 8.5 \sim 8.8.

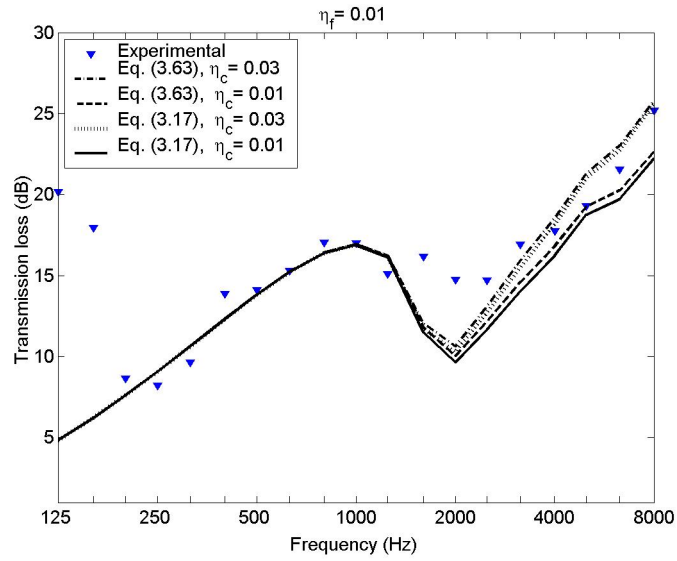


Figure 8.6: Predicted sound transmission loss values of panel J from the wave impedance analysis

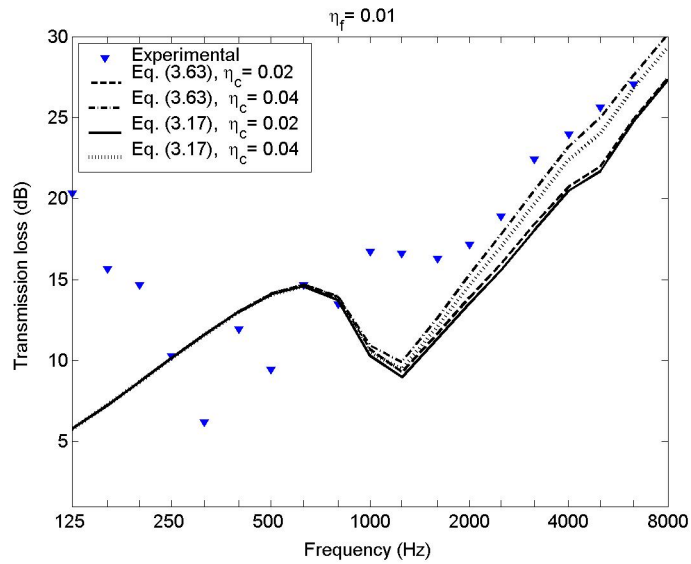


Figure 8.7: Predicted sound transmission loss values of panel K from the wave impedance analysis

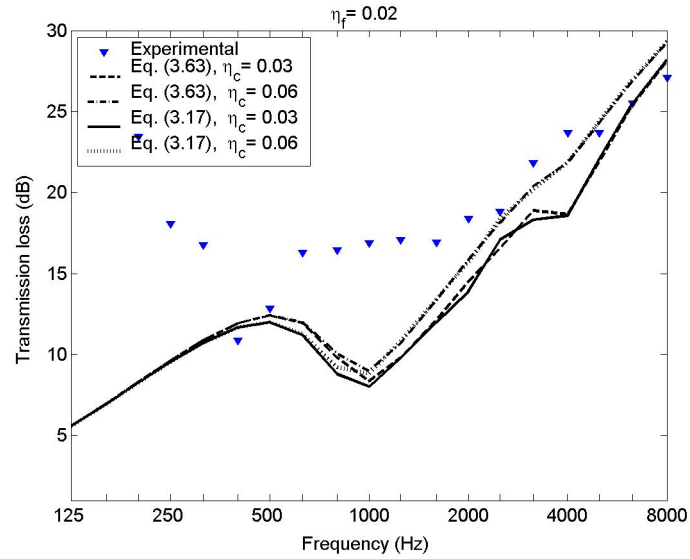


Figure 8.8: Predicted sound transmission loss values of panel L from the wave impedance analysis

The predicted critical coincidence frequencies of panels I , J , K and L associated with anti-symmetric motion are in the one-third octave bands with center frequencies of 2500 Hz, 2000 Hz, 1250 Hz and 1000 Hz, respectively. The effect of damping in the face sheets and core on the transmission loss of the sandwich panels is negligible at frequencies below the critical coincidence frequencies. The predictions of sound transmission loss are in good agreement with the experimental values of all four panels at frequencies above the critical coincidence frequencies. Also the predictions for panels I and J agree well with the measured results below their critical coincidence frequencies. It was found that the difference between the predictions from the two equations is less than 2 dB up to 8000 Hz for all four sandwich panels.

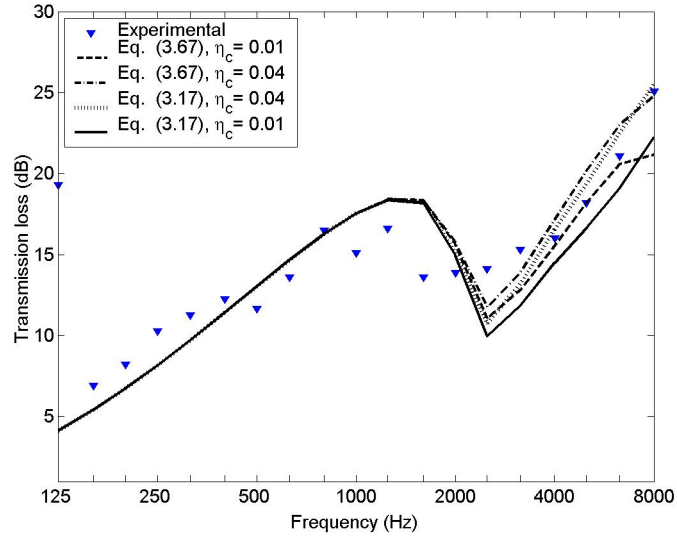


Figure 8.9: Predicted sound transmission loss values of panel I by using Eq. (3.67)

Nilsson and Nilsson [37] neglected the symmetric motion and considered the rotatory inertia of the face sheets and core in their work. Figures 8.9 ~ 8.12 show comparisons between the predictions of sound transmission loss for panels $I \sim L$ using the wave impedances calculated from their equation, Eq. (3.67) and the presented governing equation in Chap. 3, Eq. (3.17).

It is seen that the effects of rotatory inertia of the face sheets and core on the sound transmission loss of thin panels, I and J , are more apparent than those of thick panels, K and L . All three predictions from wave impedance analysis provide similar sound transmission loss values for all four sandwich panels.

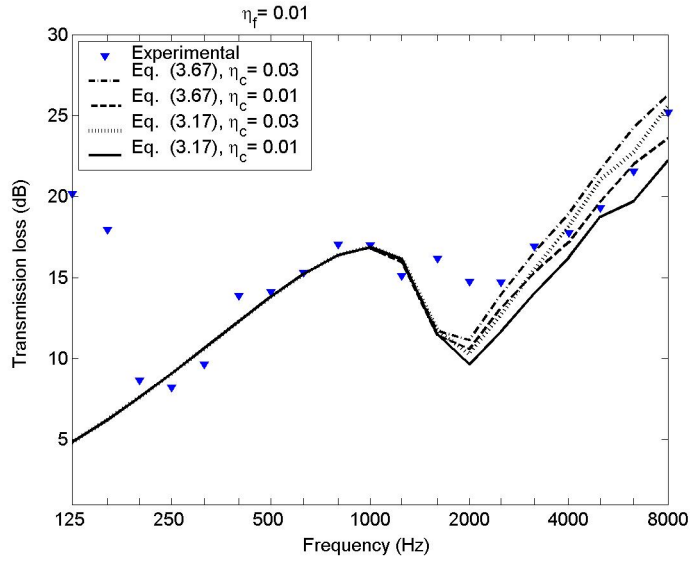


Figure 8.10: Predicted sound transmission loss values of panel *J* by using Eq. (3.67)

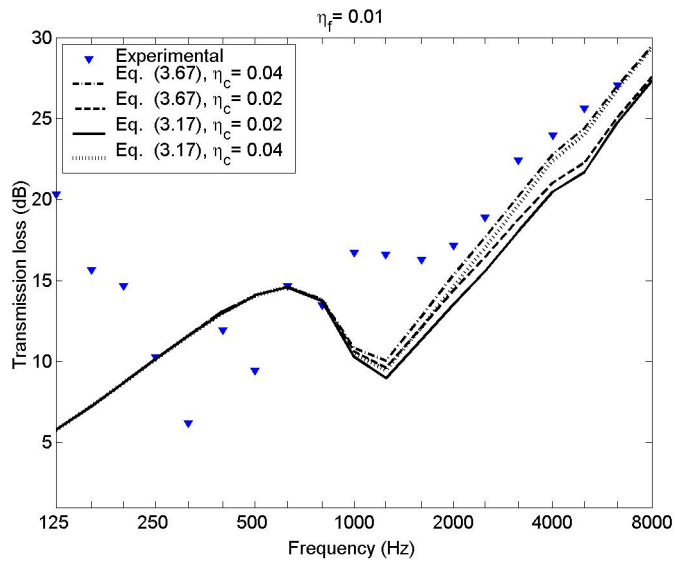


Figure 8.11: Predicted sound transmission loss values of panel *K* by using Eq. (3.67)

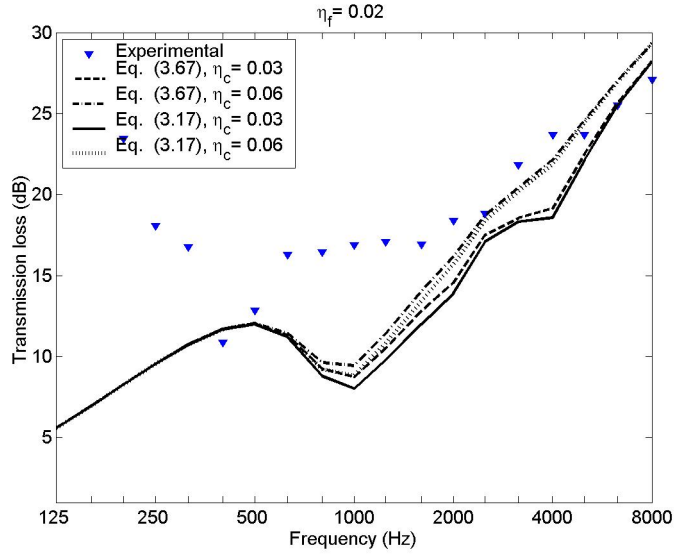


Figure 8.12: Predicted sound transmission loss values of panel L by using Eq. (3.67)

8.4 Sound transmission loss from statistical energy analysis

The sound transmission loss for the SEA model of a transmission suite as discussed in Sec. 4.7, is

$$\text{TL} = 10 \log_{10} \left[\frac{A_p T_3}{0161 V_3} \left(\frac{E_1/V_1}{E_3/V_3} - 1 \right) \right], \text{ with,} \quad (8.2)$$

$$\frac{E_1/n_1}{E_3/n_3} - 1 = \frac{2\eta_{\text{rad}} n_2 \eta_3 n_3 + (\eta_3 n_3 + \eta_{\text{rad}} n_2) \eta_2 n_2}{\eta_{\text{rad}}^2 n_2 n_2 + \eta_{13} (2\eta_{\text{rad}} + \eta_2) n_1 n_2},$$

where T_3 is the reverberation time of the receiving room. The parameters used in the SEA calculation were evaluated both experimentally and theoretically to compute the sound transmission loss of the four sandwich panels. The internal loss factor of the receiving room,

η_3 , was determined from the reverberation time of the receiving room, by using Eq. (4.32). The reverberation time of the receiving room was obtained by averaging the reverberation times at eight randomly chosen positions. The modal densities of the two reverberation rooms, n_1 and n_3 , were obtained from Eq. (4.15). The values of the radiation loss factor, η_{rad} , used were determined from Eq. (4.42). The values of the coupling loss factor, η_{13} , were determined from the field incidence mass law transmission coefficient, Eq. (4.46). Then the values of modal density, n_2 , used were the modal density for simply supported conditions and were derived from Eqs. (4.29) and (4.30). The sound transmission loss estimates for the panels were generated for two different values of internal loss factor of the panels.

The sound transmission loss estimates for panel *I* are shown in Fig. 8.13. The estimates are in good agreement with the experimental results except below the first resonance frequency and near coincidence. The disagreement near coincidence is reduced when the measured values of radiation loss factor η_{rad} near coincidence are used in the calculation, as illustrated in Fig. 8.14.

Sound transmission loss estimates for panels *J*, *K* and *L* are shown in Figs. 8.15 ~ 8.17.

The sound transmission estimates for panels *J* and *K* agree well with the experimental values when the measured values of radiation loss factor η_{rad} near coincidence are used in the calculations. The discrepancy for panel *L* is attributable to insufficient panel modes to make a correct band-averaged value of modal density. According to the finite element analysis, below 1000 Hz, there are only four modes in the clamped panel *L*. That may also

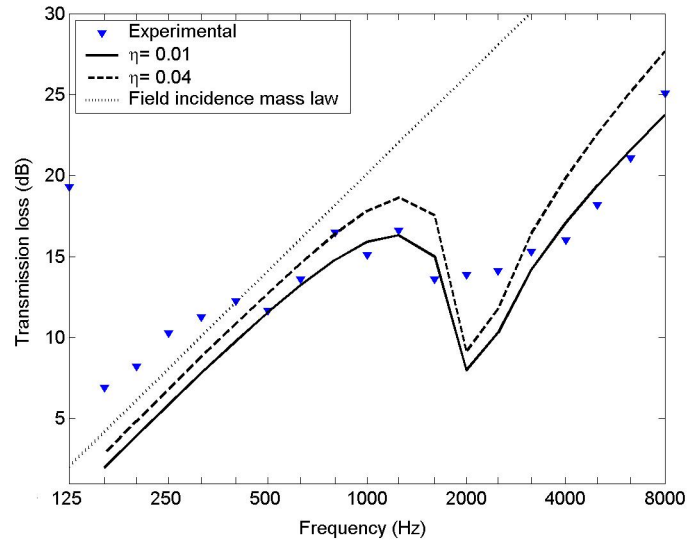


Figure 8.13: Transmission loss estimates for panel *I* from SEA

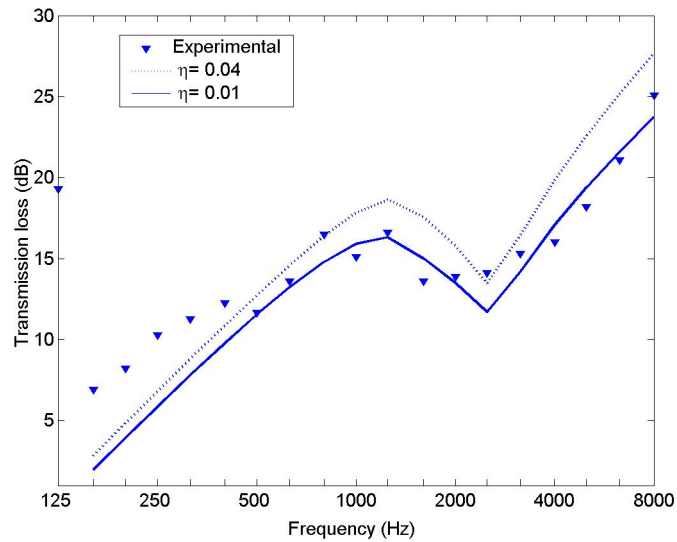


Figure 8.14: Transmission loss estimates for panel *I* using the measured values of η_{rad}

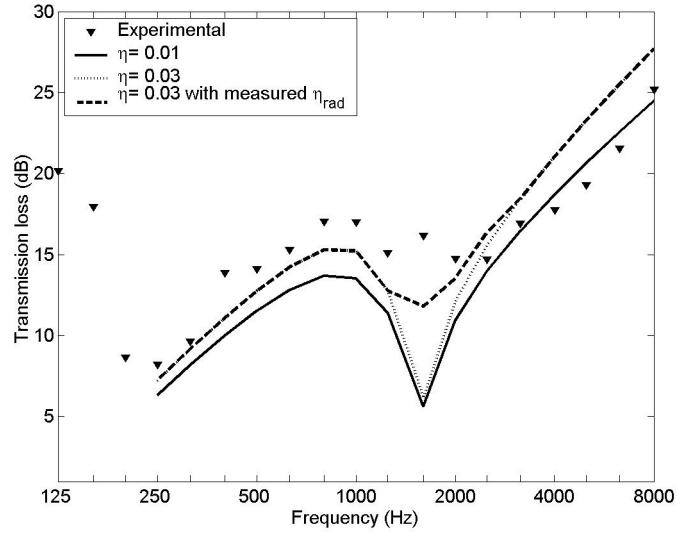


Figure 8.15: Transmission loss estimates for panel J using the measured values of η_{rad}

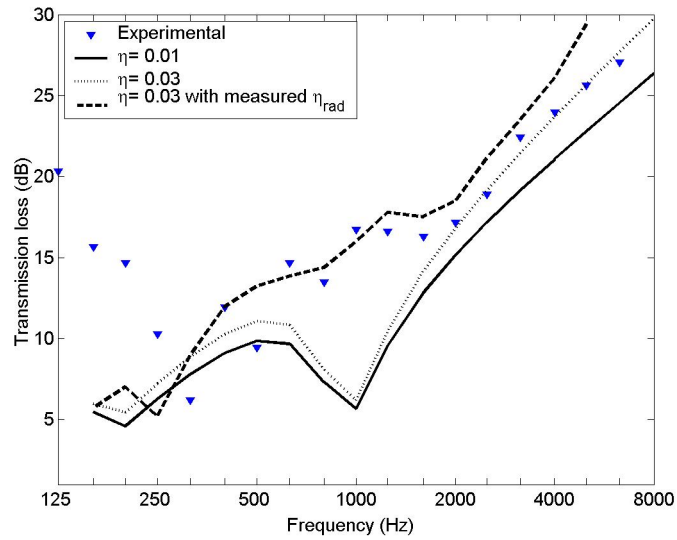


Figure 8.16: Transmission loss estimates for panel K using the measured values of η_{rad}

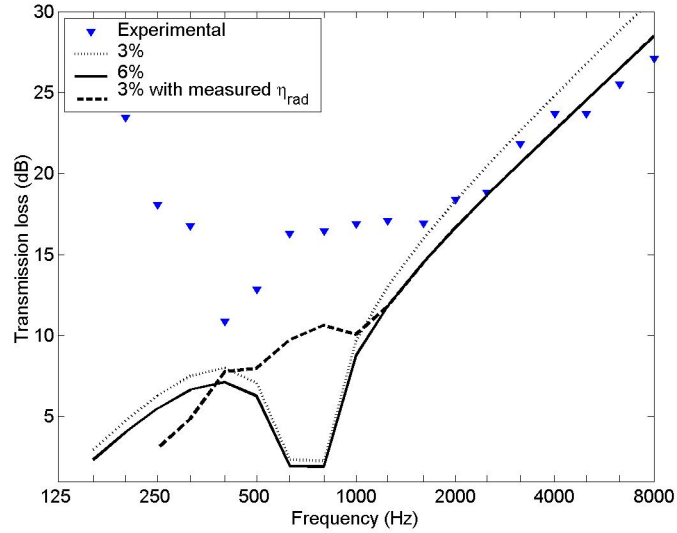


Figure 8.17: Transmission loss estimates for panel L using the measured values of η_{rad}

explain that the measured radiation resistance values of panel L are quite different from those of the other three sandwich panels.

8.5 Sound transmission loss from boundary element analysis

The sound transmission characteristics of the four sandwich panels were also computed by the boundary element analysis model proposed in Sec. 5.5. The finite element mesh of the sandwich panel was generated in MSC Nastran, and consisted of 60×36 CQUAD4 elements for each face sheet, and 60×36 HEXA elements for the core. A finite element model database and a boundary element indirect baffled model database were created in the boundary element analysis software, LMS SYSNOISE. The element mesh of one face sheet was imported to the software as the structural meshes for both databases and to occupy

Table 8.3: Modal frequencies of panel K from Johnson and Kienholz's [48] finite element model

Mode (m, n)	(1,1)	(2,1)	(3,1)	(1,2)	(2,2)	(4,1)	(3,2)
f_{mn} (Hz)	344	442	619	752	824	858	957
Mode (m, n)	(5,1)	(4,2)	(1,3)	(2,3)	(5,2)	(3,3)	(6,1)
f_{mn} (Hz)	1141	1149	1241	1301	1391	1407	1454

on the plane $z = 0$. The computed eigenvectors of the first 30 modes for the face sheet were imported to the software as the structural modes in the finite element model database. A plane wave source was defined in the boundary element model database at 5 m below the center of the panel. The two databases were linked to solve the displacement of the sandwich panel. A 1 m radius hemisphere field point mesh that was assumed to cover the receiver side of the panel was used to obtain the radiated sound power of the panel. The frequency increment used was 4 Hz.

The predicted transmission loss values of composite sandwich panel K for plane sound waves at oblique incidences, $\theta = 12^\circ$, 60° , and $\phi = 45^\circ$, are shown in Fig. 8.18. The calculated modal frequencies obtained from the finite element analysis are given in Table 8.3. It is seen that the contribution of even-even modes can be substantial on the sound transmission loss of composite sandwich panel K for plane sound waves at oblique incidence. The sound transmission loss is less sensitive to the angle of incidence, θ , at low frequencies.

Since the sound transmission loss measurements were conducted in reverberation rooms, for comparison purpose, the sound transmission loss was evaluated by averaging over the angle of incidence θ , and the angle of rotation, ϕ . Figure 8.19 shows a comparison between

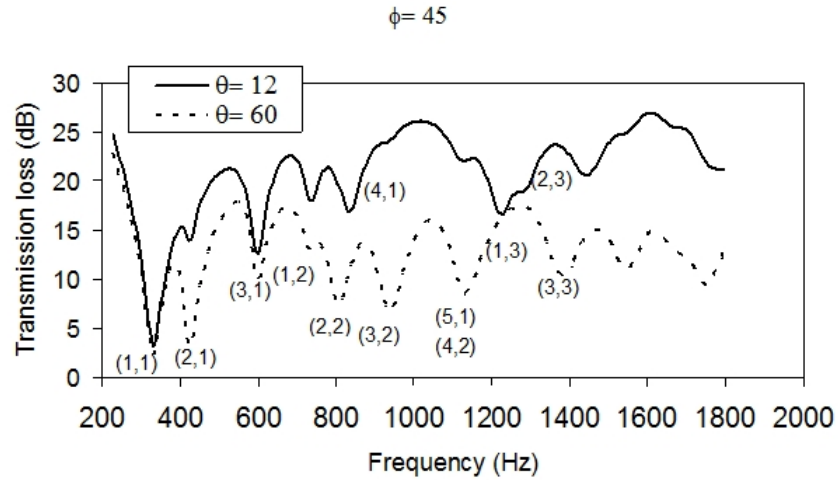


Figure 8.18: Predicted sound transmission loss values of panel K from the boundary element analysis, for sound waves at oblique incidences

the sound transmission loss data for panel K measured experimentally and those calculated from the boundary element analysis model. Predictions were made using two values of the modal loss factor, 0.01 and 0.02.

The predicted sound transmission loss values increase with increasing modal loss factor. The increase varies from band to band and it is dependent on the resonant modes in the one-third octave band under consideration. The disagreement at low frequencies is thought to be caused by the ideal clamped boundary condition assumed in the finite element analysis. While the discrepancy around 500 Hz is much larger than the difference generated by different values of loss factor. The discrepancy may be caused by frequency-dependent

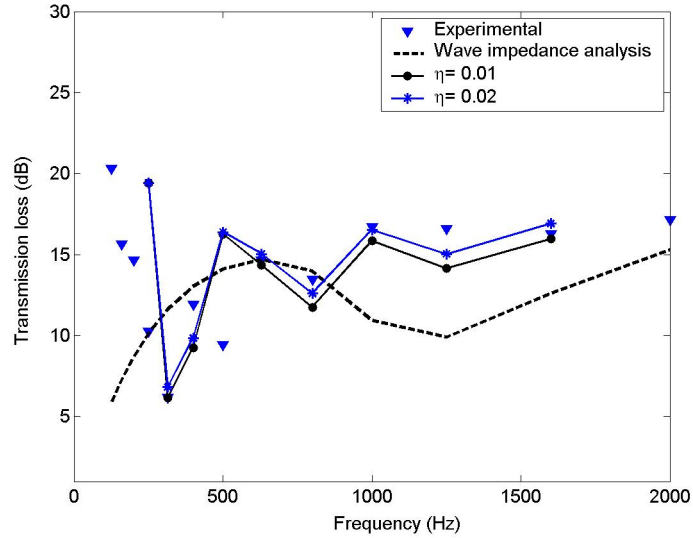


Figure 8.19: Predictions of sound transmission loss for panel K made using the boundary element analysis model

material properties. The predictions for panel K are in better agreement with the experimental values than those made using the other two analyses, wave impedance analysis and SEA.

The predictions of sound transmission loss for panels I , J and L are shown in Figs. 8.20 ~ 8.22. The first 30 modes were included and the frequency step was 4 Hz. Boundary element analysis provides accurate predictions of transmission loss for panel I above 400 Hz. The discrepancy of panel J around 800 Hz was thought to be caused by frequency-dependent material properties. The profiles of the predicted and experimental transmission loss for panel L are very similar. Since the assumed material properties of panel L were obtained experimentally from a small number of measured resonance frequencies of the two beams,

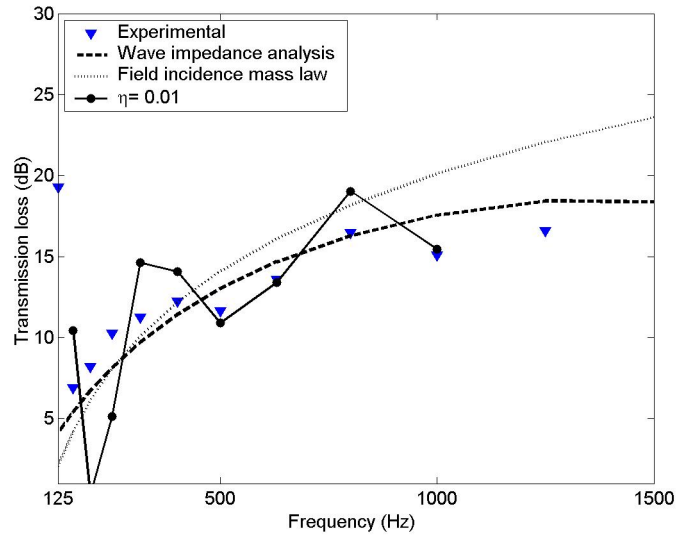


Figure 8.20: The prediction of sound transmission loss for panel *I* made using the boundary element analysis model

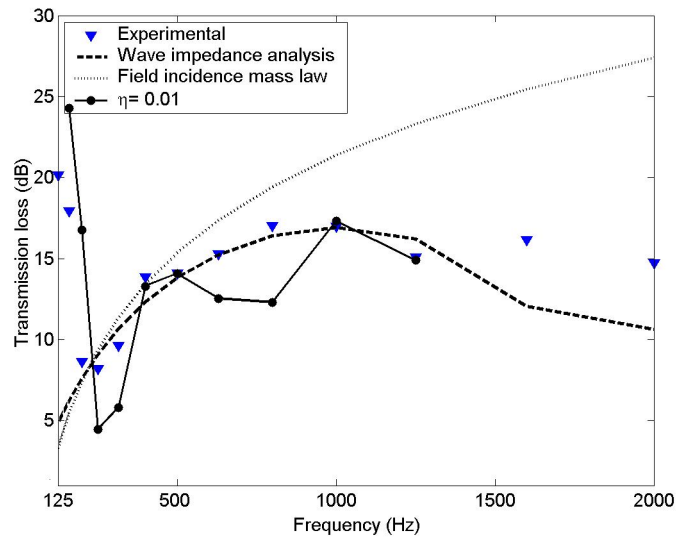


Figure 8.21: The prediction of sound transmission loss for panel *J* made using the boundary element analysis model

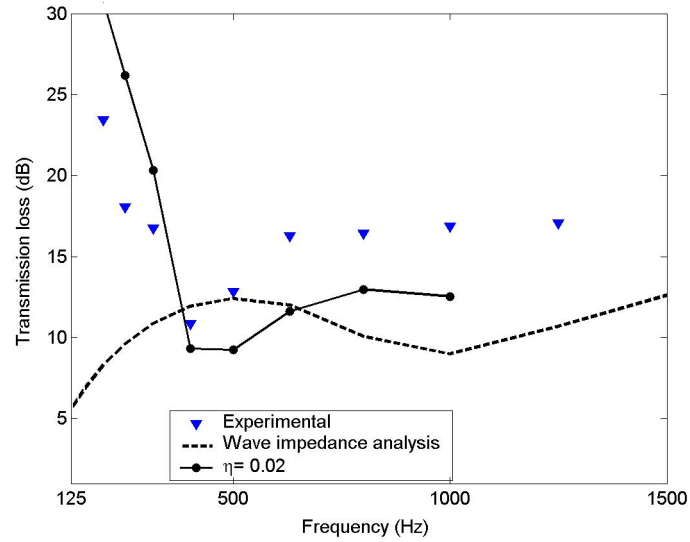


Figure 8.22: The prediction of sound transmission loss for panel L made using the boundary element analysis model

then the amplitude difference between the predicted and experimental sound transmission losses may perhaps be reduced by use of more accurate material properties.

8.6 Conclusions

The experimental sound transmission loss results for thin sandwich panels, I and J , follow the field incidence mass law at frequencies well below their critical frequencies. The transverse motions of the four panels are dominated by the anti-symmetric motion in the frequency range of 125 Hz \sim 8000 Hz. The wave impedance analysis provides a good prediction of sound transmission loss for the four sandwich panels at frequencies above the critical frequency. The statistical energy analysis also provides a good prediction of sound

transmission loss for the four sandwich panels at frequencies above the critical frequency. The predictions of sound transmission loss are very sensitive to the radiation loss factor near coincidence. Both wave impedance analysis and statistical energy analysis provide accurate estimates of sound transmission loss for thin sandwich panels, I and J . The boundary element analysis provides the most accurate predictions of sound transmission loss for thick sandwich panels K and L at low frequencies except near the first resonance frequency.

CHAPTER 9

CONCLUSIONS

The governing equations for the forced vibration of asymmetric sandwich panels were developed from energy relationships and are presented in matrix form. For the type of sandwich panels with graphite fiber face sheets and foam-filled honeycomb cores tested in this study, the anti-symmetric motion was found to be dominant and the effect of rotatory inertia on the transverse displacement of the panels was found to be small in the frequency range of interest.

A closed-form expression for the modal densities of sandwich panels was developed from a typical sixth-order governing equation of motion for sandwich panels with stiff cores. The derived modal density of a traditional honeycomb sandwich panel was found to be one half of the approximate modal density that is obtained from a fourth-order governing equation.

A computer program was developed to compute the sound transmission loss of a baffled simply supported aluminum panel. The presence of the fluid modifies the resonance characteristics of the aluminum panel, slightly shifting modal frequencies to lower frequencies. The radiated sound power of the panel was found to be higher than the virtual sound power flow near the low order resonance frequencies. For finite single-layer isotropic rectangular panels, the sound transmission loss depends not only on the angle of incidence, θ , but on the angle of rotation as well, ϕ . The contribution of other than odd-odd modes on the sound transmission loss of single-layer panels is negligible for plane sound waves at normal

incidence, while those can be substantial for plane sound waves at oblique incidence. The transmission loss values are less sensitive to the damping and the angles of incidence and rotation at low frequencies.

A boundary element analysis model for the sound transmission loss of symmetric sandwich panels is proposed. This model requires a minimum increase in computation effort relative to the effort needed for single-layer panels. It can be implemented with two commercial softwares, LMS SYSNOISE and MSC Nastran.

The material properties for the graphite fiber face sheets and foam-filled honeycomb cores of the sandwich panels investigated in this study were estimated based on the measurements of the resonance frequencies of the beams which were cut from the panels. Because the sandwich panels are light, about $\sim 3 \text{ kg/m}^2$, it was necessary to include the effect of mass loading of the transducer used to measure the panel vibration in order to obtain accurate point mobilities of the panels. The modal densities of the panels were estimated by using a three-channel spectral analysis with a spectral mass correction method, which was used to consider the mass loading of the impedance head. Experimental modal density results for the sandwich panels were found to agree well with the theoretical estimates. Allowance was also made for the effect of mass loading of the accelerometer in the estimations for both total loss factors and radiation loss factors of the panels.

The radiation loss factors of clamped sandwich panels are large near coincidence, especially for thin sandwich panels; while the radiation loss factors of un baffled free-edge

sandwich panels are much smaller than those of baffled clamped sandwich panels. The internal loss factors are dominant in the total loss factor estimates for the unbaffled free-edge sandwich panels studied. The internal loss factors of the sandwich panel were found to be much larger than those of metal panels.

The wave impedance analysis model provides accurate predictions of sound transmission loss for thin composite sandwich panels at frequencies above their first resonance frequencies. The proposed boundary element analysis model provides more accurate predictions of sound transmission loss for thick sandwich panels than either the wave impedance analysis model or the statistical energy analysis model. The predicted and experimental transmission loss values of the sandwich panels are in better agreement when the measured radiation loss factor values near coincidence are used instead of the theoretical values for single-layer panels. The expression for the radiation resistance of sandwich panels is a subject that requires further study.

BIBLIOGRAPHY

- [1] G. Kurtze and B. G. Watters, New wall design for high transmission loss or high damping, *Journal of the Acoustical Society of America* 31 (1959) 739-748.
- [2] R. D. Ford, P. Lord and A. W. Walker, Sound transmission through sandwich constructions, *Journal of Sound and Vibration* 5 (1967) 9-21.
- [3] C. P. Smolenski and E. M. Krokosky, Dilational-mode sound transmission in sandwich panels, *Journal of the Acoustical Society of America* 54 (1973) 1449-1457.
- [4] C. L. Dym and M. A. Lang, Transmission of sound through sandwich panels, *Journal of the Acoustical Society of America* 56 (1974) 1523-1532.
- [5] C. L. Dym, C. S. Ventres and M. A. Lang, Transmission of sound through sandwich panels: a reconsideration, *Journal of the Acoustical Society of America* 59 (1976) 364-367.
- [6] J. A. Moore and R. H. Lyon, Sound transmission loss characteristics of sandwich panel constructions, *Journal of the Acoustical Society of America* 89 (1991) 777-791.
- [7] C. L. Dym and D. C. Lang, Transmission loss of damped asymmetric sandwich panels with orthotropic cores, *Journal of Sound and Vibration* 88 (1983) 299-319.
- [8] A. C. Nilsson, Wave propagation in and sound transmission through sandwich plates, *Journal of Sound and Vibration* 138 (1990) 73-94.
- [9] A. C. Nilsson, Sound transmission through single leaf panels, Report 74-01, Chalmers University of Technology, 1974.
- [10] R. E. Jones, Field sound insulation of load-bearing sandwich panels for housing, *Noise Control Engineering* 16 (1981) 90-105.
- [11] R. H. Lyon and G. Maidanik, Power flow between linearly coupled oscillators, *Journal of the Acoustical Society of America* 34 (1962) 623-639.
- [12] P. W. Smith, Response and radiation of structural modes excited by sound, *Journal of the Acoustical Society of America* 34 (1962) 640-647.
- [13] G. Maidanik, Response of ribbed panels to reverberant acoustic fields, *Journal of the Acoustical Society of America* 34 (1962) 809-826.

- [14] R. H. Lyon, Noise reduction of rectangular enclosures with one flexible wall, *Journal of the Acoustical Society of America* 35 (1963) 1791-1797.
- [15] E. Eichler, Thermal circuit approach to vibration in coupled systems and the noise reduction of a rectangular box, *Journal of the Acoustical Society of America* 37 (1965) 995-1007.
- [16] P. H. White and A. Powell, Transmission of random sound and vibration through a rectangular double wall, *Journal of the Acoustical Society of America* 40 (1966) 821-832.
- [17] A. London, Transmission of reverberant sound through double walls, *Journal of the Acoustical Society of America* 22 (1950) 270-279.
- [18] M. J. Crocker and A. J. Price, Sound transmission using statistical energy analysis, *Journal of Sound and Vibration* 9 (1969) 469-486.
- [19] A. J. Price and M. J. Crocker, Sound transmission through double panels using statistical energy analysis, *Journal of the Acoustical Society of America* 47 (1970) 683-693.
- [20] E. C. Sewell, Transmission of reverberant sound through a single-leaf partition surrounded by an infinite rigid baffle, *Journal of Sound and Vibration* 12 (1970) 21-32.
- [21] B. L. Clarkson and R. J. Pope, Experimental determination of modal densities and loss factors of flat plates and cylinders, *Journal of Sound and Vibration* 77 (1981) 535-549.
- [22] B. L. Clarkson and M. F. Ranky, Modal density of honeycomb plates, *Journal of Sound and Vibration* 91(1983) 103-118.
- [23] D. J. Mead and S. Markus, The force vibration of a three-layer, damped sandwich beam with arbitrary boundary conditions, *Journal of Sound and Vibration* 10 (1969) 163-175.
- [24] A. Berry, J. L. Guyader and J. Nicolas, A general formulation for the sound radiation from rectangular baffled plates with arbitrary boundary conditions, *Journal of the Acoustical Society of America* 88 (1990) 2792-2802.
- [25] C. H. Oppenheimer and S. Dubowsky, A radiation efficiency for unbaffled plates with experimental validation, *Journal of Sound and Vibration* 199 (1997) 473-489.
- [26] K. Renji and P. S. Nair, Modal density of composite honeycomb sandwich panels, *Journal of Sound and Vibration* 195 (1996) 687-699.
- [27] K. Renji, Experimental modal densities honeycomb sandwich panels at high frequencies, *Journal of Sound and Vibration* 237 (2000) 67-79.

- [28] K. Renji and S. S. Narayan, Loss factors of composite honeycomb sandwich panels, *Journal of Sound and Vibration* 250 (2002) 745-761.
- [29] R. M. Jones, *Mechanics of Composite Materials*, Taylor & Francis, Philadelphia, 1999.
- [30] P. R. Keswick and M. P. Norton, A comparison of modal density measurement techniques, *Applied Acoustics* 20 (1987) 137-153.
- [31] K. Renji and P. S. Nair, Response of a plate to diffuse acoustic field using statistical energy analysis, *Journal of Sound and Vibration* 254 (2002) 523-539.
- [32] J. B. Mariem and M. A. Hamdi, A new boundary finite method for fluid-structure interaction problems, *International Journal for Numerical Methods in Engineering*, 24 (1987) 1251-1267.
- [33] L. P. Barisciano, Broadband transmission loss due to reverberant excitation, NASA/CR 1999-209687.
- [34] P. J. T. Filippi, P. O. Mattei and C. Maury, Sound transmission through a thin baffled plate: validation of a light fluid approximation with numerical and experimental results, *Journal of Sound and Vibration* 229 (2000) 1157-1169.
- [35] P. Thamburaj and J. Q. Sun, Effect of material and geometry on the sound and vibration transmission across a sandwich beam, *Journal of Vibration and Acoustics* 123 (2001) 205-212.
- [36] C. I. Papadopoulos, Development of an optimized standard compliant procedure to calculate sound transmission loss: design of transmission rooms, *Applied Acoustics* 63 (2002) 1003-1029.
- [37] E. Nilsson and A. C. Nilsson, Prediction and measurement of some dynamic properties of sandwich structures with honeycomb and foam cores, *Journal of Sound and Vibration* 251 (2002) 409-430.
- [38] I. Ver and C. Holmer, Interaction of sound waves with solid structures, *Noise and vibration control*, McGrawhill, New York, 1971.
- [39] R. H. Lyon and T. D. Scharton, Vibrational-energy transmission in a three-element structure, *Journal of the Acoustical Society of America* 38 (1965) 253-261.
- [40] K. T. Brown and M. P. Norton, Some comments on the experimental determination of modal densities and loss factors for statistical energy analysis application, *Journal of Sound and Vibration* 102 (1985) 588-594.
- [41] N. S. Ferguson and B. L. Clarkson, The modal density of honeycomb shells, *Journal of vibration, Acoustics, Stress, and Reliability in Design* 108 (1986) 399-404.

- [42] L. Cremer, M. Heckl and E. E. Ungar, *Structure-borne sound*, Springer-Verlag, New York, 1973.
- [43] M. P. Norton, *Fundamentals of Noise and Vibration analysis for Engineers*, Cambridge University Press, Cambridge; New York, 1989.
- [44] A. S. Nikiforov, Radiation of sound from a plate of finite dimensions with arbitrary boundary conditions, *Soviet Physics - Acoustics* 10 (1964) 178-182.
- [45] L. A. Roussos, Noise transmission loss of a rectangular plate in an infinite baffle, NASA technical paper, NAS 1.6 2398, 1985
- [46] T. W. Wu and A. Dandapani, A boundary element solution for sound transmission through thin panels, *Journal of Sound and Vibration* 171 (1994) 145-157.
- [47] Y. P. Lu and J. W. Killian, On the vibrational attenuation of damped plate structural systems, David W. Taylor Naval Ship Research and Development Center, Report 78/005, 1978.
- [48] C. D. Johnson and D. A. Kienholz, Finite element prediction of damping in structures with constrained viscoelastic layers, *AIAA Journal* 20 (1982) 1284-1290.
- [49] M. G. Sainsbury and Q. J. Zhang, The galerkin element method applied to the vibration of damped sandwich beams, *Computers and Structures* 71 (1999) 239-256.
- [50] D. K. Rao, Frequency and loss factors of sandwich beams under various boundary conditions, *Journal of Mechanical Engineering Science* 20 (1978) 271-282.
- [51] S. Markus, V. Oravsky and O. Simkova, Damping properties of sandwich beams with local shearing prevention, *Acustica* 31 (1974) 132-138.
- [52] H. G. Allen, *Analysis and Design of Structural Sandwich Panels*, Pergamon Press, Oxford, 1969.
- [53] L. J. Gibson and M. F. Ashby, *Cellular Solids - Structure and Properties*, Pergamon Press, Oxford, 1988.
- [54] Structural Sandwich Composites, MIL-HDBK-23A, Government Printing Office, Washington D.C., 1968.
- [55] K. T. Brown, Measurement of modal density: an improved technique for use on lightly damped structures, *Journal of Sound and Vibration* 96 (1984) 127-132.
- [56] E. A. Starr, Sound and vibration Transducers, *Noise and Vibration Control*, McGraw-Hill, New York, 1971.
- [57] M. F. Ranky and B. L. Clarkson, Frequency average loss factors of plates and shells, *Journal of Sound and Vibration* 89 (1983) 309-323.

- [58] M. C. Gomperts, Radiation from rigid baffled, rectangular plates with general boundary conditions, *Acustica* 30 (1974) 320-327.
- [59] W. Huang and C. Ng, Sound insulation improvement using honeycomb sandwich panels, *Applied Acoustics* 53(1998) 163-177.
- [60] S. Rajaram, T. Wang and S. Nutt, Sound transmission loss of honeycomb sandwich panels, *Noise Control Engineering Journal* 54 (2006) 106-115.
- [61] S. Narayanan and R. L. Shanbhag, Sound transmission through a damped sandwich panel, *Journal of Sound and Vibration* 80 (1982) 315-327.
- [62] D. Zenkert, *The Hand Book of Sandwich Construction*, Chameleon, London, 1997.

APPENDIX A

DERIVATION OF STIFFNESS CONSTANTS OF ROTATED-AXIS

If all three principal axes for the orthotropic material are aligned with the three axes of the coordinate systems, the stiffness matrix of orthotropic material takes the form,

$$\begin{pmatrix} \sigma_x \\ \sigma_y \\ \sigma_z \\ \tau_{yz} \\ \tau_{xz} \\ \tau_{xy} \end{pmatrix} = \begin{bmatrix} C_{11} & C_{12} & C_{13} & 0 & 0 & 0 \\ C_{12} & C_{22} & C_{23} & 0 & 0 & 0 \\ C_{13} & C_{23} & C_{33} & 0 & 0 & 0 \\ 0 & 0 & 0 & C_{44} & 0 & 0 \\ 0 & 0 & 0 & 0 & C_{55} & 0 \\ 0 & 0 & 0 & 0 & 0 & C_{66} \end{bmatrix} \begin{pmatrix} \sigma_x \\ \sigma_y \\ \sigma_z \\ \tau_{yz} \\ \tau_{xz} \\ \tau_{xy} \end{pmatrix}$$

where

$$\begin{aligned} C_{11} &= \frac{1 - \nu_{23}\nu_{32}}{\Delta} E_1, \quad C_{12} = \frac{\nu_{12} + \nu_{13}\nu_{32}}{\Delta} E_2 = \frac{\nu_{21} + \nu_{23}\nu_{31}}{\Delta} E_1, \\ C_{13} &= \frac{\nu_{13} + \nu_{12}\nu_{23}}{\Delta} E_3 = \frac{\nu_{31} + \nu_{21}\nu_{32}}{\Delta} E_1, \quad C_{22} = \frac{1 - \nu_{13}\nu_{31}}{\Delta} E_2, \\ C_{23} &= \frac{\nu_{32} + \nu_{12}\nu_{31}}{\Delta} E_2 = \frac{\nu_{23} + \nu_{21}\nu_{13}}{\Delta} E_3, \quad C_{33} = \frac{1 - \nu_{12}\nu_{21}}{\Delta} E_3, \\ \Delta &= 1 - \nu_{12}\nu_{21} - \nu_{23}\nu_{32} - \nu_{13}\nu_{31} - 2\nu_{12}\nu_{23}\nu_{31}, \\ C_{44} &= G_{23}, \quad C_{55} = G_{13}, \quad C_{66} = G_{12}. \end{aligned}$$

If the Young's modulus in one principal axis of orthotropic material is much stiffer than those in the others, $E_3 \gg E_1, E_2$, $\nu_{31}, \nu_{32} \gg \nu_{13}, \nu_{23}$, the stiffness constants can be approximated,

$$\begin{aligned} C_{11} &= \frac{E_1}{1 - \nu_{12}\nu_{21}}, \quad C_{12} = \frac{\nu_{12}}{1 - \nu_{12}\nu_{21}} E_2 = \frac{\nu_{21}}{1 - \nu_{12}\nu_{21}} E_1, \\ C_{13} &= \frac{\nu_{13}}{1 - \nu_{12}\nu_{21}} E_3 = \frac{\nu_{31}}{1 - \nu_{12}\nu_{21}} E_1, \quad C_{22} = \frac{E_2}{1 - \nu_{12}\nu_{21}}, \\ C_{23} &= \frac{\nu_{32}}{1 - \nu_{12}\nu_{21}} E_2 = \frac{\nu_{23}}{1 - \nu_{12}\nu_{21}} E_3, \quad C_{33} = \frac{E_3}{1 - \nu_{12}\nu_{21}}. \end{aligned}$$

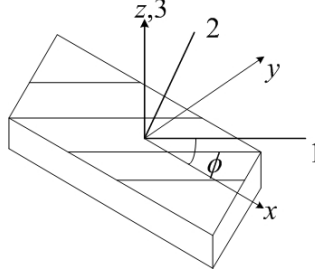


Figure A.1: The rotated-axis coordinate system of the orthotropic material

According to the tensor transformation rule, the stresses and strains along the principal axes can be written with the stresses and strains in x, y, z axes,

$$\begin{bmatrix} \sigma_1 & \tau_{12} & \tau_{13} \\ \tau_{12} & \sigma_2 & \tau_{23} \\ \tau_{13} & \tau_{23} & \sigma_3 \end{bmatrix} = \mathbf{A} \begin{bmatrix} \sigma_x & \tau_{xy} & \tau_{xz} \\ \tau_{xy} & \sigma_y & \tau_{yz} \\ \tau_{xz} & \tau_{yz} & \sigma_z \end{bmatrix} \mathbf{A}^T,$$

$$\begin{bmatrix} \varepsilon_1 & \gamma_{12}/2 & \gamma_{13}/2 \\ \gamma_{12}/2 & \varepsilon_2 & \gamma_{23}/2 \\ \gamma_{13}/2 & \gamma_{23}/2 & \varepsilon_3 \end{bmatrix} = \mathbf{A} \begin{bmatrix} \varepsilon_x & \gamma_{xy}/2 & \gamma_{xz}/2 \\ \gamma_{xy}/2 & \varepsilon_y & \gamma_{yz}/2 \\ \gamma_{xz}/2 & \gamma_{yz}/2 & \varepsilon_z \end{bmatrix} \mathbf{A}^T,$$

where $\mathbf{A} = \begin{bmatrix} \cos \theta & \sin \theta & 0 \\ -\sin \theta & \cos \theta & 0 \\ 0 & 0 & 1 \end{bmatrix} = \begin{bmatrix} l & m & 0 \\ -m & l & 0 \\ 0 & 0 & 1 \end{bmatrix}$.

Expanding the equations above, produces

$$\begin{Bmatrix} \sigma_1 \\ \sigma_2 \\ \sigma_3 \\ \tau_{23} \\ \tau_{13} \\ \tau_{12} \end{Bmatrix} = \mathbf{T} \begin{Bmatrix} \sigma_x \\ \sigma_y \\ \sigma_z \\ \tau_{yz} \\ \tau_{xz} \\ \tau_{xy} \end{Bmatrix} = \begin{bmatrix} l^2 & m^2 & 0 & 0 & 0 & 2lm \\ m^2 & l^2 & 0 & 0 & 0 & -2lm \\ 0 & 0 & 1 & 0 & 0 & 0 \\ 0 & 0 & 0 & l & -m & 0 \\ 0 & 0 & 0 & -m & l & 0 \\ -lm & lm & 0 & 0 & 0 & l^2 - m^2 \end{bmatrix} \begin{Bmatrix} \sigma_x \\ \sigma_y \\ \sigma_z \\ \tau_{yz} \\ \tau_{xz} \\ \tau_{xy} \end{Bmatrix}, \text{ and}$$

$$\begin{Bmatrix} \varepsilon_1 \\ \varepsilon_2 \\ \varepsilon_3 \\ \gamma_{23}/2 \\ \gamma_{13}/2 \\ \gamma_{12}/2 \end{Bmatrix} = \mathbf{T} \begin{Bmatrix} \varepsilon_x \\ \varepsilon_y \\ \varepsilon_z \\ \gamma_{yz}/2 \\ \gamma_{xz}/2 \\ \gamma_{xy}/2 \end{Bmatrix}.$$

The relationships between engineering strains and tensorial strains can be expressed as,

$$\begin{Bmatrix} \varepsilon_x \\ \varepsilon_y \\ \varepsilon_z \\ \gamma_{yz} \\ \gamma_{xz} \\ \gamma_{xy} \end{Bmatrix} = \mathbf{R} \begin{Bmatrix} \varepsilon_x \\ \varepsilon_y \\ \varepsilon_z \\ \gamma_{yz}/2 \\ \gamma_{xz}/2 \\ \gamma_{xy}/2 \end{Bmatrix} = \begin{bmatrix} 1 & & & & & \\ & 1 & & & & \\ & & 1 & & & \\ & & & 2 & & \\ & & & & 2 & \\ & & & & & 2 \end{bmatrix} \begin{Bmatrix} \varepsilon_x \\ \varepsilon_y \\ \varepsilon_z \\ \gamma_{yz}/2 \\ \gamma_{xz}/2 \\ \gamma_{xy}/2 \end{Bmatrix}.$$

Applying the stress-strain relations in the three principal axes and introducing the developed transformations above, we obtain

$$\begin{Bmatrix} \sigma_1 \\ \sigma_2 \\ \sigma_3 \\ \tau_{23} \\ \tau_{13} \\ \tau_{12} \end{Bmatrix} = \mathbf{T} \begin{Bmatrix} \sigma_x \\ \sigma_y \\ \sigma_z \\ \tau_{yz} \\ \tau_{xz} \\ \tau_{xy} \end{Bmatrix} = \mathbf{C} \begin{Bmatrix} \varepsilon_1 \\ \varepsilon_2 \\ \varepsilon_3 \\ \gamma_{23} \\ \gamma_{13} \\ \gamma_{12} \end{Bmatrix} = \mathbf{CR} \begin{Bmatrix} \varepsilon_1 \\ \varepsilon_2 \\ \varepsilon_3 \\ \gamma_{23}/2 \\ \gamma_{13}/2 \\ \gamma_{12}/2 \end{Bmatrix} = \mathbf{CRT} \begin{Bmatrix} \varepsilon_x \\ \varepsilon_y \\ \varepsilon_z \\ \gamma_{yz}/2 \\ \gamma_{xz}/2 \\ \gamma_{xy}/2 \end{Bmatrix},$$

$$\text{then, } \begin{Bmatrix} \sigma_x \\ \sigma_y \\ \sigma_z \\ \tau_{yz} \\ \tau_{xz} \\ \tau_{xy} \end{Bmatrix} = \overline{\mathbf{C}} \begin{Bmatrix} \varepsilon_x \\ \varepsilon_y \\ \varepsilon_z \\ \gamma_{yz} \\ \gamma_{xz} \\ \gamma_{xy} \end{Bmatrix}, \text{ where } \overline{\mathbf{C}} = \mathbf{T}^{-1}\mathbf{CRTR}^{-1},$$

$$\begin{aligned} \overline{C}_{11} &= l^4 C_{11} + 2l^2 m^2 (C_{12} + 2C_{66}) + m^4 C_{22}, \\ \overline{C}_{12} &= l^2 m^2 C_{11} + (l^4 + m^4) C_{12} + l^2 m^2 C_{22} - 4l^2 m^2 C_{66}, \\ \overline{C}_{13} &= l^2 C_{13} + m^2 C_{23}, \\ \overline{C}_{16} &= l^3 m C_{11} + (lm^3 - l^3 m) C_{12} - lm^3 C_{22} + 2(lm^3 - l^3 m) C_{66}, \\ \overline{C}_{22} &= m^4 C_{11} + 2l^2 m^2 (C_{12} + 2C_{66}) + l^4 C_{22}, \\ \overline{C}_{26} &= lm^3 C_{11} + (l^3 m - lm^3) C_{12} - l^3 m C_{22} + 2(l^3 m - lm^3) C_{66}, \\ \overline{C}_{33} &= C_{33}, \overline{C}_{44} = m^2 C_{55} + l^2 C_{44}, \overline{C}_{55} = m^2 C_{44} + l^2 C_{55}, \\ \overline{C}_{66} &= l^2 m^2 C_{11} - 2l^2 m^2 C_{12} + l^2 m^2 C_{22} + (l^2 - m^2) C_{66}, \\ \overline{C}_{34} &= \overline{C}_{35} = \overline{C}_{36} = \overline{C}_{14} = \overline{C}_{15} = \overline{C}_{24} = \overline{C}_{25} = 0. \end{aligned}$$

APPENDIX B
PARTIAL DIFFERENTIAL OPERATORS

The elements of the matrix \mathbf{B} of Eq. (3.59) are differential operators which are listed below:

$$\begin{aligned}
B_{11} &= -\frac{mh^2}{4} \frac{\partial^4}{\partial x^2 \partial t^2} + m^* \frac{\partial^2}{\partial t^2} + \bar{D} \frac{\partial^4}{\partial x^4} - h \left(2C_{13} + \frac{C_{55}}{3} \right) + \frac{4C_{13}}{h}, \\
B_{12} &= \frac{mh}{2} \frac{\partial^3}{\partial x \partial t^2} - \bar{F} \frac{\partial^3}{\partial x^3} + 2C_{13} \frac{\partial}{\partial x}, \quad B_{13} = \frac{\rho h^2}{\pi} \frac{\partial^3}{\partial x \partial t^2} - \frac{C_{11} h^2}{\pi} \frac{\partial^3}{\partial x^3} + \frac{4}{\pi} (C_{13} + C_{55}) \frac{\partial}{\partial x}, \\
B_{22} &= -m \frac{\partial^2}{\partial t^2} + \bar{C} \frac{\partial^2}{\partial x^2}, \quad B_{23} = \frac{2C_{11} h}{\pi} \frac{\partial^2}{\partial x^2} - \frac{2\rho h}{\pi} \frac{\partial^2}{\partial t^2}, \\
B_{33} &= -\frac{\rho h}{2} \frac{\partial^2}{\partial t^2} + \frac{C_{11} h}{2} \frac{\partial^2}{\partial x^2} + \frac{\pi^2 C_{55}}{2h}, \quad B_{34} = B_{35} = 0, \\
B_{14} &= \frac{h^2 (\rho_1 t_1 - \rho_2 t_2)}{4} \frac{\partial^4}{\partial x^2 \partial t^2} - (\rho_1 t_1 - \rho_2 t_2) \frac{\partial^2}{\partial t^2} - (D_1 - D_2) \frac{\partial^4}{\partial x^4}, \\
B_{24} &= B_{15} = -\frac{h(\rho_1 t_1 - \rho_2 t_2)}{2} \frac{\partial^3}{\partial x \partial t^2} + (F_1 - F_2) \frac{\partial^3}{\partial x^3}, \\
B_{25} &= (\rho_1 t_1 - \rho_2 t_2) \frac{\partial^2}{\partial t^2} - (C_1 - C_2) \frac{\partial^2}{\partial x^2}, \\
B_{44} &= -\frac{m^* h^2}{4} \frac{\partial^4}{\partial x^2 \partial t^2} + m \frac{\partial^2}{\partial t^2} + \tilde{D} \frac{\partial^4}{\partial x^4}, \\
B_{45} &= \frac{m^* h}{2} \frac{\partial^3}{\partial x \partial t^2} - \tilde{F} \frac{\partial^3}{\partial x^3}, \quad B_{55} = -m^* \frac{\partial^2}{\partial t^2} + \tilde{C} \frac{\partial^2}{\partial x^2} - \frac{4C_{55}}{h},
\end{aligned}$$

with,

$$\begin{aligned}
m &= \rho_1 t_1 + \rho_2 t_2 + \rho h, \quad m^* = \rho_1 t_1 + \rho_2 t_2 + \frac{\rho h}{3}, \\
\bar{C} &= C_1 + C_2 + C_{11} h, \quad \bar{F} = F_1 + F_2 + \frac{C_{11} h^2}{2}, \\
\tilde{C} &= C_1 + C_2 + \frac{C_{11} h}{3}, \quad \tilde{F} = F_1 + F_2 + \frac{C_{11} h^2}{6}, \\
\bar{D} &= D_1 + D_2 + \frac{C_{11} h^3}{4}, \quad D_i = \frac{E_i}{3(1 - v_i^2)} \left[\left(\frac{h}{2} + t_i \right)^3 + \left(\frac{h}{2} \right)^3 \right], \\
C_i &= \frac{E_i t_i}{(1 - v_i^2)}, \quad F_i = \frac{E_i}{2(1 - v_i^2)} \left[\left(\frac{h}{2} + t_i \right)^2 + \left(\frac{h}{2} \right)^2 \right],
\end{aligned}$$

where ρ_j and ρ denote mass densities of the face sheet j and the core; t_j and h stand for thicknesses of the face sheet j and the core, respectively. E_j is the Young's modulus of the

face sheet j . C_{ij} is the stiffness constants of the core, and the directions denote as follows,

$$\begin{Bmatrix} \sigma_x \\ \sigma_y \\ \sigma_z \\ \tau_{yz} \\ \tau_{xz} \\ \tau_{xy} \end{Bmatrix} = \begin{bmatrix} C_{11} & C_{12} & C_{13} & 0 & 0 & 0 \\ C_{12} & C_{22} & C_{23} & 0 & 0 & 0 \\ C_{13} & C_{23} & C_{33} & 0 & 0 & 0 \\ 0 & 0 & 0 & C_{44} & 0 & 0 \\ 0 & 0 & 0 & 0 & C_{55} & 0 \\ 0 & 0 & 0 & 0 & 0 & C_{66} \end{bmatrix} \begin{Bmatrix} \sigma_x \\ \sigma_y \\ \sigma_z \\ \tau_{yz} \\ \tau_{xz} \\ \tau_{xy} \end{Bmatrix}.$$